

PHASE RESOLVED SPECTRAL ANALYSIS OF SELECTED INTERMEDIATE  
POLARS AND THE EFFECT OF WARM ABSORBERS IN CATAclySMIC  
VARIABLES

A THESIS SUBMITTED TO  
THE GRADUATE SCHOOL OF NATURAL AND APPLIED SCIENCES  
OF  
MIDDLE EAST TECHNICAL UNIVERSITY

BY

YAKUP PEKÖN

IN PARTIAL FULFILLMENT OF THE REQUIREMENTS  
FOR  
THE DEGREE OF DOCTOR OF PHILOSOPHY  
IN  
PHYSICS

AUGUST 2014



Approval of the thesis:

**PHASE RESOLVED SPECTRAL ANALYSIS OF SELECTED INTERMEDIATE  
POLARS AND THE EFFECT OF WARM ABSORBERS IN CATAclysmic  
VARIABLES**

submitted by **YAKUP PEKÖN** in partial fulfillment of the requirements for the degree  
of **Doctor of Philosophy in Physics Department, Middle East Technical University** by,

Prof. Dr. Canan Özgen  
Dean, Graduate School of **Natural and Applied Sciences**

\_\_\_\_\_

Prof. Dr. Mehmet T. Zeyrek  
Head of Department, **Physics**

\_\_\_\_\_

Prof. Dr. Şölen Balman  
Supervisor, **Physics Department, METU**

\_\_\_\_\_

**Examining Committee Members:**

Prof. Dr. Ümit Kızılođlu  
Physics Department, METU

\_\_\_\_\_

Prof. Dr. Şölen Balman  
Physics Department, METU

\_\_\_\_\_

Prof. Dr. Altan Baykal  
Physics Department, METU

\_\_\_\_\_

Assoc. Prof. Dr. S. Çağaş İnam  
Electrical Engineering Department, Başkent University

\_\_\_\_\_

Assoc. Prof. Dr. Ünal Ertan  
Physics Department, Sabancı University

\_\_\_\_\_

**Date:**

\_\_\_\_\_

**I hereby declare that all information in this document has been obtained and presented in accordance with academic rules and ethical conduct. I also declare that, as required by these rules and conduct, I have fully cited and referenced all material and results that are not original to this work.**

Name, Last Name: YAKUP PEKÖN

Signature :

# ABSTRACT

## PHASE RESOLVED SPECTRAL ANALYSIS OF SELECTED INTERMEDIATE POLARS AND THE EFFECT OF WARM ABSORBERS IN CATAclySMIC VARIABLES

Pekön, Yakup

Ph.D., Department of Physics

Supervisor : Prof. Dr. Şölen Balman

August 2014, 110 pages

In this study, XMM-Newton data of selected cataclysmic variables are examined. One of the sources is an Intermediate Polar (IP) EX Hya where the orbital and spin phase resolved spectra are analyzed in depth. A composite model is successfully fit to the spectra in order to explain the X-ray emission from the source. Changes in the emission, absorption and accretion behaviour of the system over the orbital and spin period of the system, as well as the changes in the system over two different epoch are determined for the first time with detailed phase resolution.

The second source is another IP, FO Aqr. The behaviour of the spin pulse of the White Dwarf in the system was examined against the orbital modulation. Different absorption components in the system are able to be distinguished from each other. And most importantly, the presence of a warm absorber in the system was detected similar to that of LMXBs for the first time.

We also study the orbital behaviour of X-rays for PQ Gem and V2069 Cyg which are IPs with soft emission components. Both systems show modulation in X-rays over the orbital period most possibly due to absorption from bulge on the disc. In PQ Gem, the absorption component from the disc is clearly separated with phase resolved spectral analysis.

Lastly the classical novae V2491 Cyg and V4743 Sgr outburst data are investigated. As opposed to hot white dwarf stellar atmosphere models (expanding or stationary) previously suggested for modelling the X-ray outburst data, an ionizing emission continuum in tandem with collisionally ionized and photoionized absorber is utilized. The fits yield promising results explaining the temperatures of the underlying WD surface and absorption lines resulting from elements in the ejecta.

Keywords: Cataclysmic Variables, Novae, FO Aqr, EX Hya, PQ Gem, V2069 Cyg, V2491 Cyg, V4743 Sgr, X-rays

## ÖZ

### SEÇİLMİŞ ORTA KUTUPSAL SİSTEMLERİN FAZ ÇÖZÜNÜRLÜKLÜ ANALİZLERİ VE ILIK SOĞURGANLARIN KATAKLİSMİK DEĞİŞKENLERDEKİ ETKİLERİ

Pekön, Yakup

Doktora, Fizik Bölümü

Tez Yöneticisi : Prof. Dr. Şölen Balman

Ağustos 2014 , 110 sayfa

Bu çalışmada bir takım seçilmiş kataklizmik değişkenlerin (CV) XMM-Newton uydusu ile alınmış verileri incelenmiştir. Kaynaklardan ilki bir Orta Kutuplu (IP) olan EX Hya olup bu kaynağın yörünge ve dönme çözünürlüklü tayf analizleri detaylı olarak incelenmiştir. Kaynaktan gelen X-ışınlarının açıklanabilmesi adına bileşke bir model tayf üzerinde uydurulmuştur. Kaynağın soğurma, salma ve madde aktarımı davranışının yörünge ve dönme periyodu üzerindeki değişiminin yanında farklı yıllardaki değişimi de ortaya konulmuştur.

İkinci kaynak, yine bir IP olan FO Aqr'dir. Burada yörünge hareketi üzerinden sistemin dönme atım profilinin değişimi incelenmiştir. Sistemdeki farklı soğurma kaynakları birbirinden ayrıştırılabilmektedir. Ve en önemli bulgu olarak da sistemde LMXBlerdeki gibi bir ılık soğurganın varlığı bir ilk olarak tespit edilmiştir.

Bunların dışında yumuşak X-ışın bileşenlerine sahip iki orta kutupsal sistem olan PQ Gem ve V2069 Cyg de yörünge üzerinden incelenmiştir. Her iki sistemde de X-ışınları yörünge periyotunda disk üzerindeki kitlenin soğurmasından kaynaklanan değişimler gözlenmiştir. PQ Gem sisteminde diskten kaynaklanan bu soğurma etkisi faz çözünürlüklü tayf analizi neticesinde açık olarak tespit edilebilmiştir.

Son olarak iki klasik nova olan V2491 Cyg ve V4743 Sgr novalarının patlama verileri incelenmiştir. Novalarda daha önceden izlenilen yol olan atmosfer modelleri yerine X-ışın tayfını açıklayabilmek adına iyonize eden bir sürem modeli ile birlikte çarpışmalı iyonize ve fotoiyonize olmuş soğurmanlar kullanılmıştır. Verilere uydurulan modeller, novalardaki beyaz cüce sıcaklıkları ve atılan maddedeki elementlerden gelen soğurma çizgilerinin belirlenmesi yolunda umut vaadeden sonuçlar ortaya koymuştur.

Anahtar Kelimeler: Katakliizmik Değişkenler, Novalar, FO Aqr, EX Hya, PQ Gem, V2069 Cyg, V2491 Cyg, V4743 Sgr, X-ışınları



This one is for me

## ACKNOWLEDGMENTS

Firstly I would like to express my sincere gratitude to my supervisor Şölen Balman. She has been my mentor and guide for more than a decade now, and her guidance, encouragement and patience has kept me going all these years.

I would like to thank my friend and office mate Mehtap Özbey Arabacı for her support and company, without her I wouldn't have come this far.

I thank my family, friends, colleagues, professors and band mates for making my world more tolerable; and my special thanks go to Mustafa İşlek and Ceren Sibel Sayın who were by my side during hard times.

Lastly I thank Tuğba Adalı for everything. It has been a rough journey for me, and I am grateful that we shared the ride most of the way. This work here is hers as well.

I acknowledge support from TÜBİTAK, The Scientific and Technological Research Council of Turkey, through project 108T735.

# TABLE OF CONTENTS

ABSTRACT . . . . .	v
ÖZ . . . . .	vii
ACKNOWLEDGMENTS . . . . .	x
TABLE OF CONTENTS . . . . .	xi
LIST OF TABLES . . . . .	xiv
LIST OF FIGURES . . . . .	xvi
CHAPTERS	
1 INTRODUCTION . . . . .	1
1.1 Definition and Classification . . . . .	1
1.2 Orbital Periods and Mass Accretion . . . . .	3
1.2.1 Accretion in non-magnetic systems . . . . .	6
1.2.2 Accretion in magnetic systems . . . . .	8
1.3 Eruptive Behavior . . . . .	9
1.3.1 Classical Nova Outbursts . . . . .	9
1.3.2 Dwarf Nova Outbursts . . . . .	12
1.3.3 Superoutbursts . . . . .	13

1.4	X-rays From Cataclysmic Variables . . . . .	13
1.4.1	Non magnetic Systems . . . . .	16
1.4.2	Polars . . . . .	19
1.4.3	Intermediate Polars . . . . .	22
2	EX HYA . . . . .	25
2.1	Observation and Data . . . . .	26
2.2	Average Spectrum . . . . .	27
2.3	Orbital Phase-Resolved Spectroscopy . . . . .	31
2.4	Spin Phase-Resolved Spectroscopy . . . . .	40
2.5	Discussion . . . . .	46
3	FO AQR . . . . .	55
3.1	Observation and Data . . . . .	56
3.2	Spin Modulation Variations over the Orbit . . . . .	57
3.3	Spectral Variations over the Orbital Phase . . . . .	60
3.4	Discussion . . . . .	62
4	PQ GEM AND V2069 CYG . . . . .	67
4.1	The Data and Observations . . . . .	68
4.2	Analysis and Results . . . . .	69
4.2.1	PQ Gem . . . . .	69
4.2.2	V2069 Cyg . . . . .	71
4.3	Discussion . . . . .	76

5	V2491 CYG AND V4743 SGR . . . . .	83
5.1	The Data and Observations . . . . .	84
5.2	Analysis and Results . . . . .	84
5.2.1	Warm and Hot Absorber Models . . . . .	84
5.2.2	<i>XMM-Newton</i> RGS Spectrum of V2491 Cyg and V4743 Sgr . . . . .	85
5.3	Discussion . . . . .	87
6	SUMMARY AND CONCLUSION . . . . .	97
	REFERENCES . . . . .	101
	CURRICULUM VITAE . . . . .	109

## LIST OF TABLES

### TABLES

Table 2.1	Spectral parameters of EX Hya from year 2000 and 2003 . . . . .	30
Table 2.2	Best fit parameters for the common Gaussian emission lines in the EX Hya spectra in 2000 and 2003. . . . .	31
Table 2.3	Spectral parameters of EX Hya derived for the year 2000 observation at each orbital phase . . . . .	36
Table 2.4	Spectral parameters of EX Hya derived for the year 2003 observation at each orbital phase . . . . .	39
Table 2.5	Spectral parameters of EX Hya derived for the year 2003 observation at each spin phase . . . . .	45
Table 2.6	Spectral parameters of EX Hya derived for the year 2000 observation at each spin phase . . . . .	49
Table 3.1	Spectral parameters derived from the fits to the orbital maxima and minima of FO Aqr . . . . .	62
Table 4.1	Spectral parameters derived from the fits to the orbital maxima and minima for PQ Gem . . . . .	74
Table 4.2	Spectral parameters derived from the fits to the orbital maxima and minima for V2069 Cyg . . . . .	76
Table 5.1	The spectral parameters from the fit with the RGS spectrum of V2491 Cyg using the XABS model in SPEX. . . . .	87
Table 5.2	The spectral parameters from the fit with the RGS spectrum of V2491 Cyg using the HOT model in SPEX. . . . .	88
Table 5.3	The spectral parameters from the fit with the RGS spectrum of V4743 Sgr using the XABS model in SPEX. . . . .	89

Table 5.4 The spectral parameters from the fit with the RGS spectrum of V4743 Sgr using the HOT model in SPEX. . . . .	90
Table 5.5 The spectral parameters from the fit with the RGS spectrum of V2491 Cyg using 3 HOT models . . . . .	91

## LIST OF FIGURES

### FIGURES

Figure 1.1	The Roche equipotentials and Lagrange points . . . . .	5
Figure 1.2	Formation of the Accretion Disc . . . . .	7
Figure 1.3	Geometry of a non-magnetic CV . . . . .	8
Figure 1.4	Geometry of an Intermediate Polar with an accretion disc . . . . .	10
Figure 1.5	Geometry of a Polar . . . . .	11
Figure 1.6	Graphic representation of the boundary layer in non-magnetic CVs	14
Figure 1.7	Graphic representation of the accretion column in magnetic CVs . .	15
Figure 1.8	ROSAT X-ray Light Curve of the Polar HU Aqr . . . . .	21
Figure 2.1	Average X-ray Spectra of EX Hya from 2000 and 2003 Data . . . .	29
Figure 2.2	Ratio of count rates of orbital maximum to orbital minimum of EX Hya . . . . .	32
Figure 2.3	The folded lightcurve and spectral parameters plotted against the orbital phase of EX Hya from 2000 data . . . . .	34
Figure 2.4	Model fit to the orbital maximum and minimum of EX Hya from 2000 data . . . . .	35
Figure 2.5	The folded lightcurve and spectral parameters plotted against the orbital phase of EX Hya from 2003 data . . . . .	37
Figure 2.6	Model fit to the orbital maximum and minimum of EX Hya from 2003 data . . . . .	38
Figure 2.7	Orbital phase resolved spectra of EX Hya from 2003 data focusing on the Fe emission lines . . . . .	41
Figure 2.8	Ratio of count rates of orbital maximum to orbital minimum of EX Hya . . . . .	42



Figure 2.9 Model fit to the spin maximum and minimum of EX Hya from 2003 data . . . . .	43
Figure 2.10 The folded lightcurve and spectral parameters plotted against the spin phase of EX Hya from 2003 data . . . . .	44
Figure 2.11 Model fit to the spin maximum and minimum of EX Hya from 2000 data . . . . .	47
Figure 2.12 The folded lightcurve and spectral parameters plotted against the spin phase of EX Hya from 2000 data . . . . .	48
Figure 2.13 The power spectrum of EX Hya from the 2000 data . . . . .	54
Figure 3.1 Lightcurve of FO Aqr folded over the orbital and spin periods . . . . .	58
Figure 3.2 The spin pulse profile of FO Aqr for each 0.1 orbital phase interval . . . . .	59
Figure 3.3 The amplitude variation of the spin pulses of FO Aqr . . . . .	60
Figure 3.4 The orbital-phase resolved spectra of FO Aqr for each 0.1 phase bin interval . . . . .	60
Figure 3.5 Warm absorber fit to the orbital minima of FO Aqr . . . . .	63
Figure 3.6 The schematic diagram of FO Aqr . . . . .	64
Figure 4.1 The light curve of PQ Gem folded over the orbital period . . . . .	69
Figure 4.2 The lightcurves of PQ Gem extracted from three different energy ranges and folded over the orbital period . . . . .	70
Figure 4.3 Hardness ratios over the orbital phase of PQ Gem . . . . .	72
Figure 4.4 The minimum and maximum spectra of PQ Gem fit with the composite model . . . . .	73
Figure 4.5 The light curve of V2069 Cyg folded over the orbital period . . . . .	75
Figure 4.6 The lightcurves of V2069 Cyg extracted from three different energy ranges and folded over the orbital period . . . . .	75
Figure 4.7 The hardness ratios over the orbital phase of V2069 Cyg . . . . .	77
Figure 4.8 The minimum and maximum spectra of V2069 Cyg fit with the composite model . . . . .	78

Figure 5.1 The RGS count rate spectrum of V2491 Cyg fitted with the XABS model . . . . .	88
Figure 5.2 The RGS count rate spectrum of V2491 Cyg fitted with the HOT model . . . . .	89
Figure 5.3 The RGS count rate spectrum of V4743 Sgr fitted with the XABS model . . . . .	90
Figure 5.4 The RGS count rate spectrum of V4743 Sgr fitted with the HOT model . . . . .	91
Figure 5.5 Plots of the best fit models for V2491 Cyg and V4743 Sgr . . . . .	92
Figure 5.6 The lightcurve of V2069 Cyg and the selected regions for spectrum extraction. . . . .	93
Figure 5.7 The composite model fit to the time filtered V2491 Cyg spectra . .	94

# CHAPTER 1

## INTRODUCTION

The sources in this study are binary systems classified as Cataclysmic Variables (CVs). This chapter will provide a background information such as classification, physical properties, accretion process and outburst mechanisms on CVs in general. X-rays in CVs are particularly important, providing information about the accretion process.

### 1.1 Definition and Classification

CVs are compact binary systems consisting of a degenerate white dwarf and a low mass main sequence star. The white dwarf, which is the primary, accretes material from the main sequence star which is the donor or secondary (Warner, 2003).

The classification of CVs are based on their eruptive behavior and the strength of magnetic fields. Thus there is an orthogonal classification of CVs, dividing them into subgroups as Classical Novae, Dwarf Novae, Recurrent Novae and Nova-like Variables depending on their eruptive behavior which are *Non-Magnetic CVs*. *Magnetic CVs* are also divided into *Polars* and *Intermediate Polars* based on the magnetic field strength of the white dwarf. There is also overlap between subclasses such as some classical novae are also intermediate polars.

*Classical Novae (CN)*, are CVs which show only one observed outburst. During the outburst their brightness can increase by up to 20 magnitudes. The amplitude of the outbursts are inversely correlated to the rate of fading after the outburst. The cause of

these outbursts is the thermonuclear runaway of the Hydrogen-rich material accreted by the white dwarf.

*Dwarf Novae (DN)* show outbursts of 2-5 magnitude. These outbursts repeat themselves in a range of 10 days to tens of years. The outbursts are caused by the release of gravitational energy due to large rate of mass transfer increase on the disc. DN have three distinct subtypes based on the outburst structures:

*Z Cam* stars show prolonging standstills after the outbursts, for about 10 days to tens of years

*SU UMa* stars show additional superoutbursts lasting longer than normal outburst.

*U Gem* stars show sudden outbursts after the quiescent phase with 2-6 magnitude in around 3-500 days

*Recurrent Novae (RN)* are like CN but show multiple outbursts.

*Nova-like Variables (NL)* are the CVs that have no outbursts. Since this is a contradicting definition, it is believed that NL consist of pro-novae, post-novae or possible *Z Cam* stars in standstill in which it may not be possible to observe the cataclysms due to our observational baseline which is about 100 years. (Warner 2003)

*Non-Magnetic CVs* include all the CVs in which the magnetic field of the white dwarf  $B \leq 10^4$  Gauss. The mass transfer to the white dwarf is achieved through an accretion stream and accretion disc.

*Polars (AM Her stars)* have white dwarfs with magnetic field strength  $B > 10^7$  Gauss. Because of the extremely strong magnetic field, accretion disc can not form in these systems. The matter flowing from the companion travels through an accretion stream and following the magnetic field lines, and falls on to the magnetic poles of the white dwarf.

*Intermediate Polars (DQ Her stars)* have magnetic fields in the  $10^6$ - $10^7$  Gauss range. The accretion discs may form and they are disrupted by the dipole magnetic field and the stream of material channeled by the field lines accretes onto the white dwarf (Hellier, 2001).

CVs play important part in astrophysics for understanding the accretion process. CVs provide us with the opportunity to observe mass transfer in long time scales since they exhibit long lived stable mass accretion. They possess similar characteristics to other compact binaries with neutron stars and black holes in terms of variability and accretion disc. Hence their number and smaller orbital periods are most useful in studying compact binaries in general. (Knigge 2011). Unlike other X-ray binaries, the discs of CVs are too cool to emit radiation in the X-ray range because of the relative shallowness of the potential well of the white dwarf. X-rays are generated from the region where accretion takes place on the white dwarf. Accretion disc and accretion process can be independently studied in different wavelengths. Because of high number of CVs in our galaxy and their closeness to Earth, it is possible to study these systems in a wide wavelength range in detail (Mukai, 2003).

## 1.2 Orbital Periods and Mass Accretion

Orbital period,  $P_{orb}$ , is the most and usually the only precisely known property of a CV.  $P_{orb}$  can provide information about the scale of the binary, allows categorizations between CV types and give an estimate about the evolution of the donor star.

Since CVs consist of two bodies bound by gravity orbiting roughly in a circular orbit around each other, they obey Kepler's law. For a given orbital separation  $a$ , mass of the primary  $M_1$ , and mass of the secondary  $M_2$ , orbital period of the system  $P_{orb}$  can be found with the following relation.

$$P_{orb}^2 = \frac{4\pi^2 a^3}{G(M_1 + M_2)} \quad (1.1)$$

Rearranging the terms in Equation 1.1 one can get the orbital separation as

$$a = 3.53 \times 10^{10} P_{orb}^{2/3} M^{1/3} (1 + q)^{1/3} \text{ cm} \quad (1.2)$$

where  $q$  is the mass ratio  $M_2/M_1$ ,  $M$  is  $M_1/M_\odot$  and  $P_{orb}$  is given in hours. Taking values  $M_1=M_2=M_\odot$  and  $P_{orb}=1-10$ , we get binary separations around  $0.5-3 R_\odot$  which

implies CVs are close binaries (Warner, 2003).

Majority of the CVs have orbital periods  $P_{orb}$  between 75 minutes and 8 hours. These systems consist of a Roche Lobe-filling main sequence star and a white dwarf. However the number is scarce in the 2-3 hr. period range which is called the *period gap*. The period gap is associated with switching from magnetic braking to gravitational radiation as the system evolves to lower  $P_{orb}$ . There are systems with  $P_{orb}$  in the 8h-3d range with evolved subgiants as donors. Some CVs have  $P_{orb} \sim 200d$  which require their donors to be giants. There exist systems with  $P_{orb}$  beyond 200 d, called symbiotic binaries, but these generally do not have Roche Lobe-filling secondaries, instead they consist of a white dwarf orbiting in the wind of a supergiant. In the region below 75 minutes there exist a class called AM CVn stars with Helium rich degenerate donors (Hellier 2001, Kuulkers et al. 2006, Nelemans 2005).

Since CVs are close binaries, their interaction is more complex than that of two point masses. Tidal interactions combining with gravitational and centrifugal effects take place, distorting the secondary star and causing it to rotate synchronously with the orbital motion. Tidal effects enable us to simplify the systems to have circular orbits and apply the Kepler's law (Equation 1.1).

During the evolutionary sequence, the secondary star expands until material can no longer be bounded by the secondary and at some point accretes to the white dwarf. The process is called Roche lobe overflow. For a free particle moving in a rotating reference system, it is the analysis of a restricted three body problem. The Roche lobe potential,

$$\Phi(\vec{R}) = -\frac{GM_1}{|\vec{R} - \vec{R}_1|} - \frac{GM_2}{|\vec{R} - \vec{R}_2|} - \frac{1}{2}(\vec{\Omega} \times \vec{R})^2 \quad (1.3)$$

where  $\Omega$  is the angular frequency of the orbit, signifies the gravitational effect of the two stars on a third object (Warner 2003). Using Roche potentials one can plot the equipotential surfaces and equilibrium points (Lagrange points) in the system as in Figure 1.1.

The innermost surface is the Roche Lobe and the point adjoining the two Roche lobes

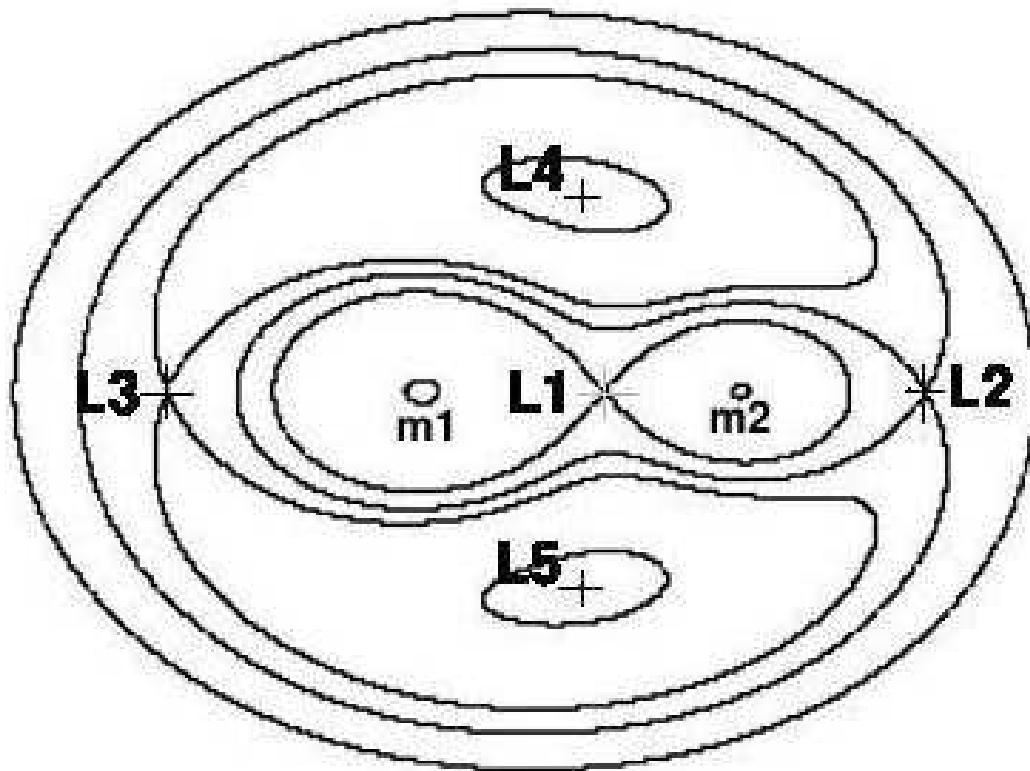


Figure 1.1: The Roche equipotentials and Lagrange points

(The lines represent the equipotentials, points  $L_1$  to  $L_5$  are the equilibrium points (Lagrangian points),  $m_1$  and  $m_2$  are the white dwarf and the secondary respectively. Adapted from Hellier (2001))

of the stars is called the *inner lagrangian point* or  $L_1$ . When the secondary star expands, it fills its Roche lobe and cannot expand any longer. The material flows out of  $L_1$  into the Roche lobe of the white dwarf. Since the white dwarf does not fill its Roche lobe the material will flow into the Roche lobe of the white dwarf.

For steady mass accretion, the binary system loses its angular momentum reducing the size of the Roche lobe so that the secondary does not have to expand to a greater extent. There are two mechanisms to allow the loss of angular momentum from the system: gravitational radiation and magnetic braking. *Gravitational radiation* occurs in close orbiting CVs releasing the gravitational energy and reducing the orbit size. *Magnetic braking* occurs when stellar wind (ionized particles) from the secondary rotates and accelerates along with its magnetic field lines and escapes the system carrying the angular momentum out. The loss of angular momentum brakes the rotation

of the secondary. However tidal forces ensure the secondary to corotate with the orbital motion, which leads to the angular momentum loss of the system and shrinking the orbit.

The accretion process and geometry of CVs are determined by the magnetic field strength of the white dwarf. So, we examine the accretion as *accretion in non-magnetic systems* and *accretion in magnetic systems*.

### 1.2.1 Accretion in non-magnetic systems

The accreted material shoots out of  $L_1$  at supersonic speeds more than 100 km/s. Because of the rotation of the Roche lobe, the velocity has a lateral component, therefore the matter does not directly fall on to the white dwarf. The stream of material moves in a path close to white dwarf and whirls around and settles into a circular orbit (on *circulization radius*) with the same angular momentum it has on  $L_1$  forming a ring. The inner parts of the ring move faster obeying the Kepler's law thus causing friction with the outer parts of the ring radiating the gravitational energy away. Having lost some angular momentum, material in the inner part of the disc moves in smaller orbits. Material in the outer ring gains angular momentum and moves to larger radii, and thus the ring spreads out to become a thin disc which is called the *accretion disc* (See Figure 1.2) (Verbunt 1982, Hellier 2001). Standard accretion disc theory attributes the angular momentum transfer to the viscosity of the disc, such that disc is composed of annuli exchanging blobs of material due to viscosity. Kinematic viscosity, governing the flow of material through the disc could be parametrised as

$$\nu = \alpha c_s H \quad (1.4)$$

where  $\nu$  is the viscosity,  $\alpha$  is a constant less than 1,  $c_s$  is the speed of sound and  $H$  is the thickness of the disc (Shakura & Sunyaev 1973).

The outer rim of the disc is bound by the tidal interactions with the secondary. The location where the material stream from the secondary intersects the accretion disc is called the *bright spot*. The innermost region of the disc where the kinetic energy of the incoming material dissipates as it settles on the WD from Keplerian velocities is called the *boundary layer*. The accretion disc lies on the orbital plane. Accretion



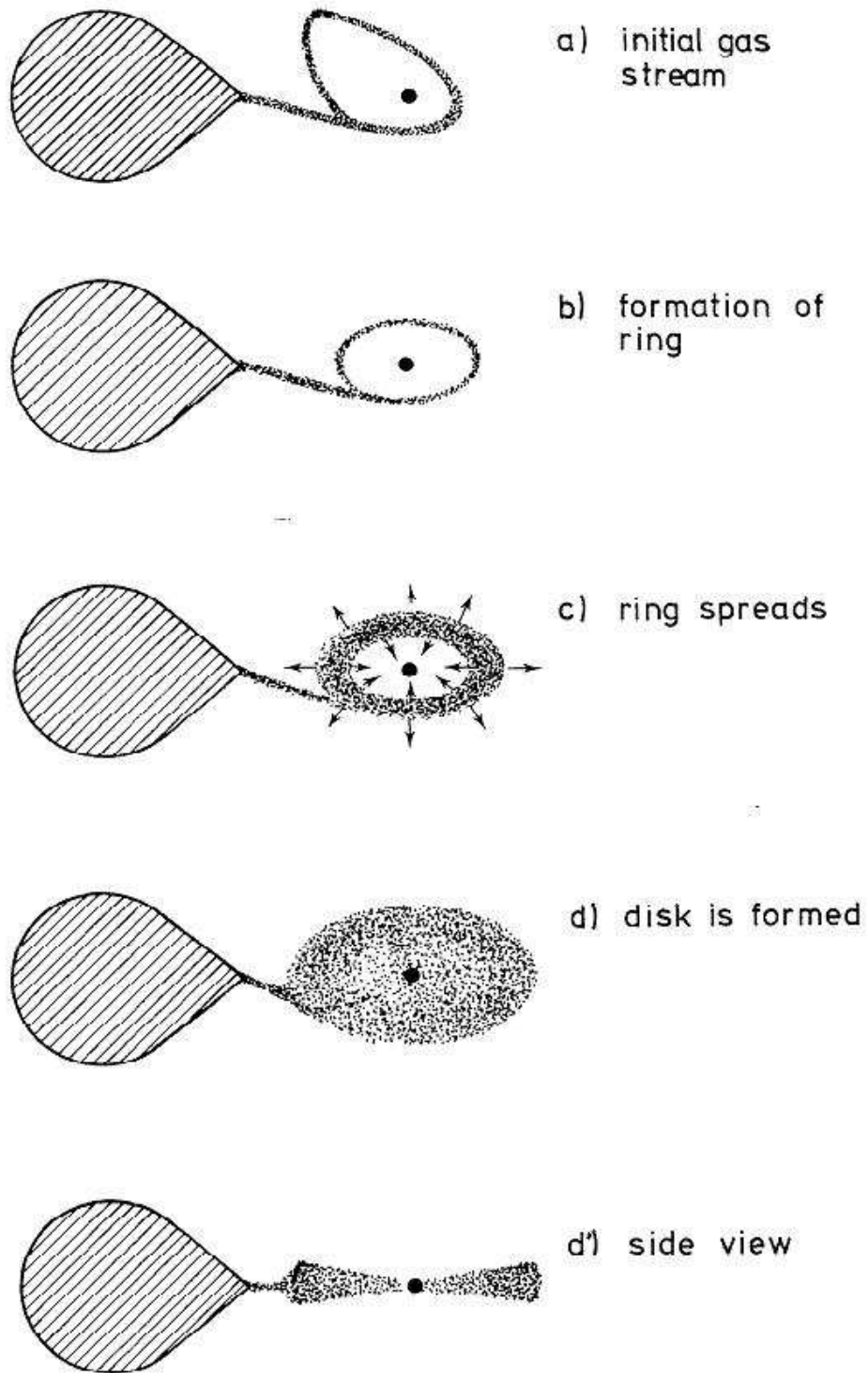


Figure 1.2: Formation of the Accretion Disc

(Figure adapted from Warner (2003))

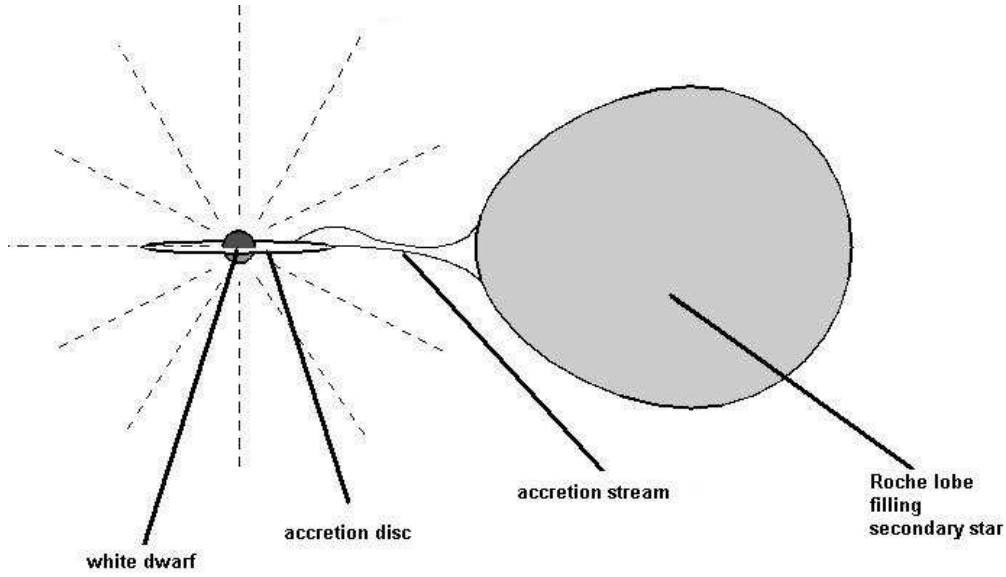


Figure 1.3: Geometry of a non-magnetic CV

(Figure taken from <http://www.physics.usyd.edu.au/rcfta/anrep93/node22.html>)

discs have a temperature of about 5000 K close to the outer radius and gets hotter toward the inner disc up to 100000 K. The disc emits in a wavelength range from IR to X-rays due to loss of gravitational energy of the particles (Hellier 2001, Hamilton et al. 2007, Balman 2014).

### 1.2.2 Accretion in magnetic systems

In the case of strong magnetic field of the white dwarf, the accretion process differs. The material moving out of the Roche lobe of the secondary follows a projectile motion as in non-magnetic case but this time magnetic field deters the motion. The effect of the magnetic field depends on the Alfvén radius where the kinetic energy density of the material is roughly equal to the magnetic energy density and given as

$$R_A = 3.7 \times 10^9 \dot{M}_{17}^{-2/7} M_{\odot}^{-1/7} \mu_{32}^{4/7} \text{ cm} \quad (1.5)$$

where  $\dot{M}_{17}$  is the accretion rate in units of  $10^{17}$  g/s,  $M_{\odot}$  is the mass of the white dwarf in terms of solar mass and  $\mu_{32}$  is magnetic moment of the white dwarf in  $10^{32}$

$G \text{ cm}^3$  (Patterson 1994). Accreted material lying within Alfvén radius is affected by the magnetic fields more than ram pressure. Here, the particles follow the magnetic field lines and accrete on to the white dwarf.

If the magnetic field strength ( $B$ ) is greater than about  $10^7$  G (as in polars) then Alfvén radius extends outside the *circulisation radius* (in extremely strong magnetic fields, it may exceed  $L_1$ ) and hence the accretion disc can not form. The transferred material locks to the field lines and co-rotate with the white dwarf and the white dwarf's spin period synchronizes with the orbital period. The material then falls on to one or two magnetic poles of the white dwarf. It forms *accretion columns* rather than the boundary layer. If the magnetic field  $B$  is in the range  $10^6$ - $10^7$  G (as in intermediate polars) the accretion disc may form, inner parts of the disc is disrupted by the magnetic field and material accretes on to the magnetic poles as in the highly magnetic case. The synchronization of white dwarf's orbital and spin periods does not occur due to weak magnetic field.

The magnetic axis do not align with the rotation axis in most cases. The system acts as an oblique rotator. The accretion column will encounter a stand off shock near the white dwarf surface and the shocked material will cool down as it reaches the white dwarf. Figure 1.3 and Figure 1.4 show magnetic accretion with and without the accretion discs respectively.

### **1.3 Eruptive Behavior**

The most distinctive and important phenomena displayed by cataclysmic variables are the outbursts. During the outburst, the brightness of the system increases dramatically and then decays. In this section, the mechanisms responsible for the outbursts will be introduced.

#### **1.3.1 Classical Nova Outbursts**

Classical nova outbursts are explosions occurring on the surface of white dwarfs in cataclysmic variables due to a *thermonuclear runaway*.

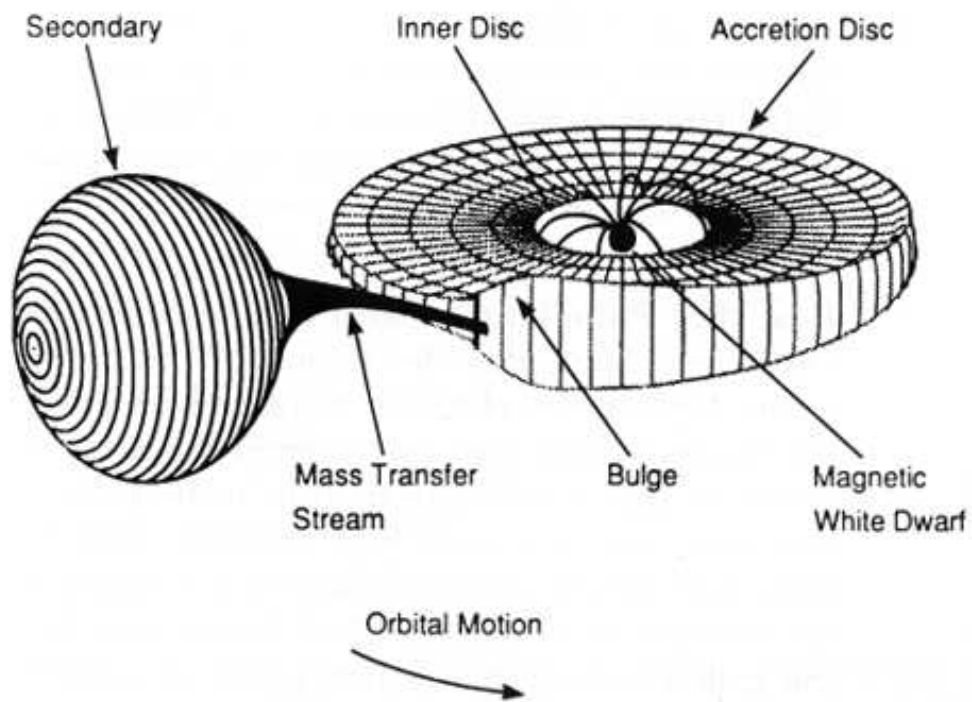


Figure 1.4: Geometry of an Intermediate Polar with an accretion disc

(Figure taken from <http://heasarc.gsfc.nasa.gov/docs/objects/cvs/cvstext.html#intermediate>)

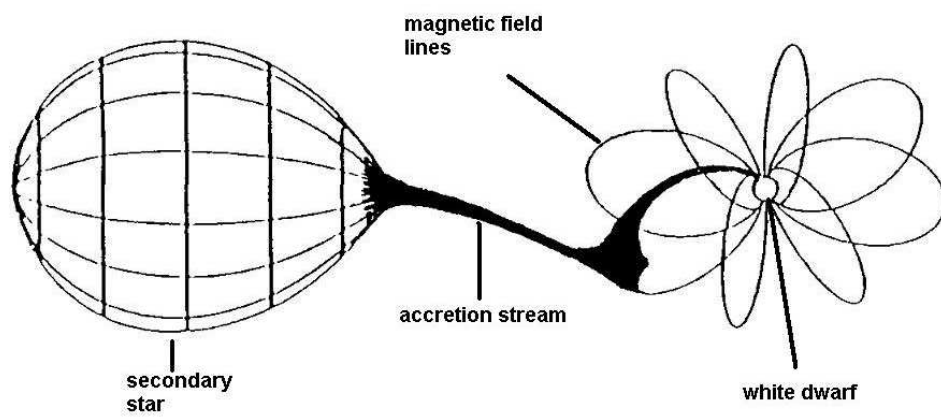


Figure 1.5: Geometry of a Polar  
(Figure is taken from Cropper (1990))

White dwarfs are burnt out cores of stars that consumed most of its Hydrogen into Helium and other heavier elements. However, the accreted material from the secondary is mostly Hydrogen and fresh Hydrogen builds up on the surface as a layer. The density of the layer increases and the electrons become degenerate and degeneracy pressure becomes dominant in the layer. As the layer thickens, temperature and density at the bottom of the layer increases to critical levels required for Hydrogen fusion. As the temperature rises above  $2 \times 10^7$  K, Thermonuclear Runaway (TNR) occurs where explosive Hydrogen burning synthesizes unstable radioactive heavy elements which are convected to the surface. At some point the temperature is exceedingly high and the material deposited at the outer shell expands out with speeds  $\sim 3000$  km/s as the energy is released (Hellier 2001, Bode & Evans 2008).

For classical novae, the accretion rates should be low enough ( $\dot{M} \sim 10^{-9}$ - $10^{-10} M_{\odot} \text{ yr}^{-1}$ ) so that the degeneracy condition is supplied. After the outburst, the white dwarf will be Hydrogen deficient again and the whole process will repeat itself within  $10^4$  -  $10^5$  years. The outburst will result in more than 3-4 orders of magnitude increase in the luminosity of the system in a few days, with a pre-maximum halt,  $\sim 2$  magnitudes before the maximum, in some cases. Nova light curves are classified according to their decay rates from maximum brightness, defined by either  $t_2$  or  $t_3$ , which are the time intervals needed to decay by 2 or 3 visual magnitudes after maximum respectively. The maximum brightness and decay times are inversely related (Hernanz 2005).

### 1.3.2 Dwarf Nova Outbursts

Dwarf nova outbursts are different than the nova outbursts by mechanism and nature of the outbursts. The energy source is simply the gravitational field of the white dwarf unlike thermonuclear runaway on the surface of the white dwarf. Basically due to instabilities in the accretion disc, mass accumulates on the disc and when the critical density is reached, accumulated mass moves rapidly on to the white dwarf releasing significant amount of energy causing the outbursts.

The outbursts show much variety in shape, magnitude and duration even within the same source. The magnitude change is around 2-5 and recurrence times are in a wide

range of a few days to tens of years. The outburst profile differ as well. The rise to maximum can be rapid or slow depending on the outburst happening from outside-in or inside-out. The peak can show a plateau-like structure when the entire disc is in outburst. The declines all show similar gradual decays. (Hellier 2001, Warner 2003)

### 1.3.3 Superoutbursts

SU UMa stars show superoutbursts additional to outbursts other dwarf novae exhibit. The normal outburst mechanism is the same but in SU Uma stars the mass lost to white dwarf is much less causing the disc to grow in size in every outburst cycle. When the disc radius reaches the *resonant radius* where particles have orbital frequency  $\Omega = 3\Omega_{orb}$ , the tidal forces are dominant on the disc so that the disc precesses. The eccentric disc can then loose enough angular momentum through spreading out the excess mass and shrink back to small symmetric disc. Thus the superoutbursts occur. The disc grows again due to normal outbursts and superoutbursts repeat themselves in a *supercycle*.

Superoutbursts occur less frequently than normal outbursts. The recurrence time varies from several hundred to several thousand days. The superoutburst last about two weeks where normal outburst last about a few days and also have higher amplitudes. During the superoutbursts, the orbital light curve shows *superhumps* ; periodic photometric light humps with amplitudes about 0.2-0.3 mag. The superhumps are seen due to the asymmetry of the disc. (Osaki 1996)

## 1.4 X-rays From Cataclysmic Variables

As stated previously, CVs emit X-rays due to accretion process, and studying X-ray properties helps us understand the accretion process and use the information in analogy with other accreting systems.

CVs emit radiation in a range of IR to X-rays and the accretion powered total luminosity is given by

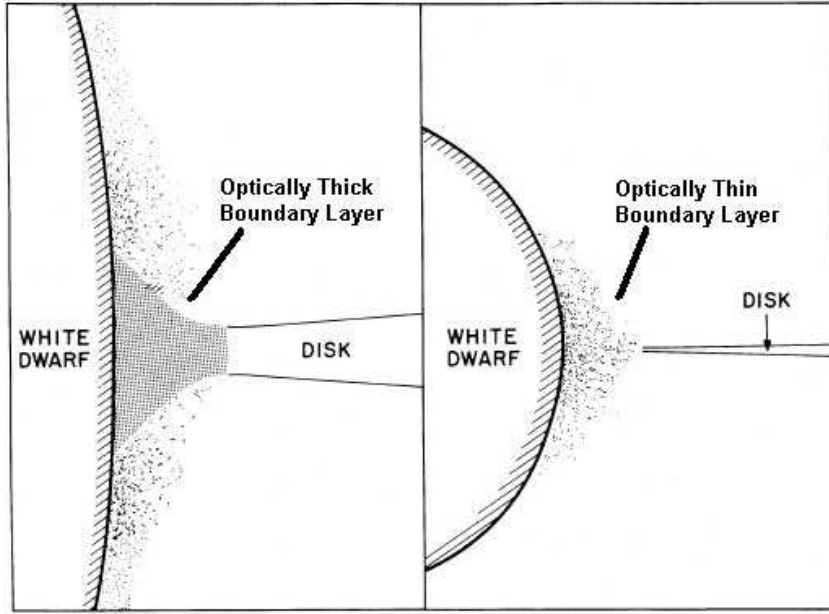


Figure 1.6: Graphic representation of the boundary layer in non-magnetic CVs

(The box on the left shows the optically thick boundary layer when the system's  $\dot{M}$  is high ( $>10^{16}$  gr/s) and on the box on the right shows the optically thin boundary layer where  $\dot{M}$  is low ( $<10^{16}$  gr/s. Adapted from Patterson & Raymond (1985).)

$$L \approx \frac{GM\dot{M}}{R} \approx 2.2 \frac{\dot{M}}{10^{-9}M_{\odot}\text{yr}^{-1}} \frac{M}{M_{\odot}} \frac{10^4\text{km}}{R_{\odot}} L_{\odot} \quad (1.6)$$

where  $M$  and  $R$  are mass and radius of the white dwarf respectively (Lynden-Bell & Pringle, 1974). The corresponding accretion rates are in the order of  $10^{-12}M_{\odot}\text{yr}^{-1}$ - $10^{-8}M_{\odot}\text{yr}^{-1}$  for typical values of mass and radius of the white dwarf.

X-rays originate mainly in the region where the accreted material settles on the surface of the white dwarf for non-magnetic systems, the boundary layer, for magnetic systems the accretion column; hence accretion geometry affects the origin and properties of emitted X-rays.



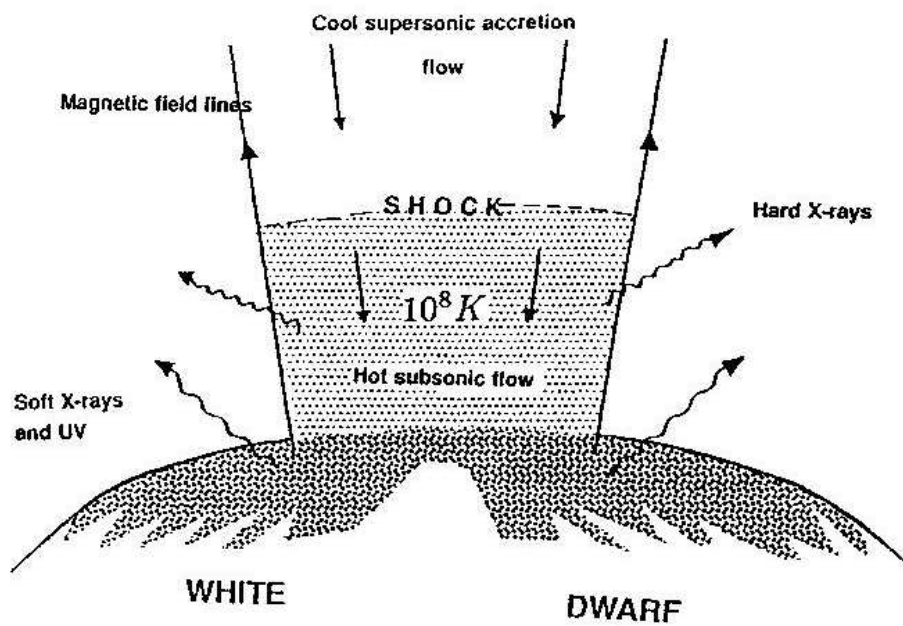


Figure 1.7: Graphic representation of the accretion column in magnetic CVs

(The figure also shows how soft and hard X-rays emerge from the accretion column.

Adapted from Patterson (1994).)

### 1.4.1 Non magnetic Systems

In Non-magnetic CVs, where  $B$  is less than about  $10^4$  Gauss, the accreted material from the donor forms an accretion disc. The material on the disc then falls on to the white dwarf via the boundary layer. Generally, half of the total luminosity is due to loss of gravitational energy on the disc while the other half is due to the loss in the boundary layer (Pringle 1981). The particles on the boundary layer moves with Keplerian velocities which is much higher than the rotation velocity of the white dwarf. The material in the disc is slowed down in order to accrete on to the white dwarf and produces X-rays in the boundary layer. The X-ray luminosities are usually  $10^{29} - 10^{32}$  erg/s (Balman 2014). These luminosities are small enough not to disturb the appearance of the disc. Since the disc has  $kT < 1$  eV it does not emit X-rays. It mainly radiates in optical and UV range. The boundary layer emits mostly in extreme UV and X-rays, so the main X-ray source of the CVs are the boundary layers (Kuulkers et al. 2006).

The nature of the X-rays from the boundary layer depends on the accretion rate ( $\dot{M}$ ) of the system. If  $\dot{M}$  is smaller than the critical accretion rate,  $\dot{M}_{critical}$  ( $10^{16}$  gr/s), then the accretion rate is low and the boundary layer will be optically thin and through release of the gravitational energy heated up to temperatures around  $10^8$  K. These systems such as Dwarf Novae in quiescent state emit mostly hard X-rays that can be represented by a multi-temperature cooling flow type plasma with maximum temperatures in the 9-55 keV range. If the system is in outburst state where  $\dot{M}$  exceeds the  $\dot{M}_{critical}$ , then the boundary layer becomes optically thick due to accumulation of more particles. The boundary layer in this situation may heat up to  $10^5$  K temperatures. The reason that it is colder than the low  $\dot{M}$  boundary layer is that cooling is more efficient since it is optically thick. In this case, the boundary layer mostly radiates in extreme UV or soft X-rays with temperatures around 5-30 eV. (Patterson & Raymond 1985, Balman 2012). During the DN outbursts, hard X-rays can also be observed, although with lower fluxes than the quiescent. The origin of this hard component during outbursts can be explained with the coronal emission above the disc (Ishida 2010).

In novae, there is a soft X-ray component which is blackbody-like stellar continuum

emission from the underlying WD after the outburst. This happens after the constant bolometric phase where the photospheric radius decreases, in turn increasing the effective photospheric temperatures peaking up to 0.1-1 keV range. There is also a hard component above 0.5 keV arising during the outburst phase. The mechanisms responsible for the hard component are circumstellar interaction, wind-wind interaction, stellar wind instabilities and mass accretion (Balman 2012 and the references therein).

The X-ray spectrum of non-magnetic systems can be explained with multi-temperature thermal plasma models. Additionally, some can be modeled with thermal plasma emission with a flat emission distribution indicating that the radiation is produced by cooling flow of the gas. A continuous thermal distribution and emission lines from various elements indicate the isobaric cooling flow plasma settling on the white dwarf. The maximum cooling flow temperatures  $T_{max}$  are in a wide range of 8-80 keV mostly for dwarf novae (Mukai et al. 2003, Rana et al. 2006, Pandel et al 2005)).

Another characteristic of the non-magnetic CVs is that the most show line emission of Fe  $K_{\alpha}$  near 6.7 keV. This emission consists of 6.4 keV fluorescent line, He-like Fe XXV line near 6.7 keV and H-like Fe XXVI line near 6.9 keV. The Fe XXV and Fe XXVI lines originate from the hot plasma with temperatures of  $10^{8-9}$  K in the accretion disc in the shocked zones. They play important role in the diagnostics of these regions. The intensity ratio of Fe XXV and XXVI lines provides information on the ionization temperature of the plasma. Fe XXV further can be used to get information about the ionization state, temperature and density of the emitting plasma in collisional ionization equilibrium. The fluorescent line of Fe originates from the lower transitions of Iron and from relatively colder plasma (less than  $10^6$  K). Their origin is mainly attributed to the reflection of hard rays from the surface of the white dwarf and/or inner accretion disc. In quiescent states, the main reflector is the white dwarf surface since the inner disc will be too thin. Although the line is from the reflection, the relation with the line strength and the inclination of the system is not clear yet (Rana & Singh et al. 2006).

Other than the Fe  $K_{\alpha}$  complex near the 6.7 keV, other emission lines are occasionally seen in X-ray spectra, especially in data where there is enough energy resolution.

Most common ones are the Fe L complex around 1 keV, and transitions of other elements such as N, O, Ne, Mg, Si and S. These emission lines provides us with better understanding of the abundance ratios, temperature distributions, electron temperatures, electron density and ionisation states of the X-ray emitting plasma. Studying the velocity broadening in the lines and looking at the velocities, one can determine the location of the X-ray emitting region whether near the fast rotating boundary layer or near the slow rotating white dwarf. (Szkody et al. 2002, Mauche & Raymond 2000, Raymond & Brickhouse 1996)

One property of X-ray light curves of the non-magnetic CVs is that in some systems orbital eclipses are detected as the X-ray emitting region is obscured. However, whether we see eclipses depends on the inclination of the system. Therefore only in systems with enough inclination angle the eclipse can be observed. Eclipses yield good diagnostics to determine the location and size of the X-ray emitting region using orbital phase and duration of ingress and egress. For dwarf novae in quiescence, X-ray eclipses are observed at the time of the optical eclipse seen. Some sources show shorter X-ray eclipse times than that of the optical one. This implies that the X-ray emitting region is smaller than the white dwarf and close to the photosphere of the white dwarf. In some systems, the eclipses are not observed during the outburst phases. This could be explained by obscuration of boundary layer at all orbital phases. There is a case for UX UMa in outburst where the eclipse is seen only in the harder X-ray region. This indicates that the source for soft and hard X-rays have different origins. (Mukai et al. 1997, van Teeseling 1997, Ramsay et al. 2001, Wheatley & West 2003, Pratt et al. 2004)

In some observations, non-magnetic CVs also show dips in their X-ray light curves in quiescent and outburst stages. The dips are shallower in quiescent state than the outburst stage due to size of X-ray emitting region in quiescence is larger than that of the outburst while the absorbing material holds the same position. During the dips the boundary layer is obscured and hence the residual X-rays possibly come from the accretion disc corona or disc wind. The dips are attributed to interaction of the accretion stream and the disc creating cool clouds of gas obscuring the X-rays. (Frank et al 1984, Naylor & la Dous 1997, Mason et al. 1997, Kuulkers et al. 2006))

X-ray light curves studies also show outbursts in non-magnetic CVs mostly in dwarf novae and nova-like variables. The X-ray outbursts lag the optical outbursts by about 12-36 hours. In the beginning of the outburst, the spectrum softens rapidly. The soft X-ray flux peaks and gradually decreases slower than the increase rate. The soft X-rays decrease and disappear before the optical outburst, hence increase and decrease times are smaller than the optical outbursts. During the increase of the soft X-rays, harder X-rays tend to be suppressed and later increases back to the quiescent levels indicating that there are two different X-ray emitting regions responsible for hard and soft X-rays. (van der Woerd et al. 1986, Wheatley et al. 2003, Mauche & Robinson 2001)

### 1.4.2 Polars

In polars, due to high magnetic field strength of the white dwarf, accreting material couples on to the magnetic field lines and flows to the magnetic poles of the white dwarf. They show intensive X-ray emission, mostly soft X-rays ( $L_X \sim 10^{32}$  ergs/s), some hard X-rays depending on the accretion rate. They also show cyclotron emission at longer wavelengths from IR to UV. (Mukai 2003, Kuulkers et. al. 2006)

According to the standard model accreting material falling on to the white dwarf forms a strong stand-off shock close almost vertically to the surface due to high speed of the accretion material. Most of the radiation at all wavelengths including hard X-rays originate in this shock region when the material is heated up to 10-40 keV energies due to the shock and cooled as material settles on the white dwarf. The soft X-rays with temperatures of ( $10^5$  K) arise from the absorbed and re-radiated emission from the footprints of the accretion column surrounding the area of hard X-ray emitting region (Wu 2000, King & Lasota 1979, Lamb & Masters 1979).

Early X-ray observations with ROSAT showed that the soft X-ray emission is much higher than the expected from the standard model. This was explained by assuming that the accretion is in forms of blobs due to the strong magnetic field, rather than uniform streams penetrate into the photosphere. The shock region is then buried and hard X-rays are thermalised releasing soft X-rays. Late observations with XMM-Newton shows that the excess is not as much as the ROSAT data presents. Moreover,

XMM-Newton data established that low accretion systems ( $\dot{M} < 10^{-11} M_{\odot} \text{ yr}^{-1}$ ) show very little soft components than the high accretion systems. (Ramsay et al. 1994, Ramsay & Cropper 2004, Ramsay et al. 2004, Singh 2013)

As in the case of non-magnetic systems, early low signal-to-noise, low resolution spectral data of polars were fit with simple bremsstrahlung model with temperatures about 15 keV with a simpler absorber and a reflection coefficient to account for the reflected emission from the surface of the white dwarf. Later, with better spectral data, the main approach was using bremsstrahlung component for the hard X-rays and blackbody component for the soft X-rays (Ramsay et al. 1994, Beuermann & Burwitz 1995, Mukai 2003). The soft component of the spectrum should be more complicated however mostly blackbody is used for simplicity. For the hard X-ray emission, since the accreted matter cools from high temperature in the shock front to lower temperatures at the bottom of the shock region, multi-temperature shock models were established (Cropper et. al 2000). Multi-temperature plasma models such as MEKAL with various temperatures or plasma emission with continuous emission measure (CEVMEKL) were also used to fit the hard X-ray spectra from polars. (Singh et al. 2004, Schwarz et al 2005)

Line emission is also observed in polars, since recent X-ray missions can resolve them. The most common one is (although not many polars show strong intensities) the Fe  $K_{\alpha}$  complex near the 6.7 keV as with non-magnetic CVs. The  $K_{\alpha}$  complex is comprised of He-like, H-like and fluorescent Fe emission lines produced in the post-shock region where the multi-temperature plasma is present. The line complex is a good tool for determination of white dwarf mass and for density diagnostics. They show low doppler shifts meaning the emission is from the lower and denser base of the accretion column. Spin modulation of the width of the lines were also reported. (Hellier & Mukai 2004, Terada et al. 2004, McNamara et al. 2008)

Despite simple accretion geometry, polars display a rich phenomenology of X-ray light curves. X-ray light curve modulation has many aspects such as the locations of the accretion spots, stellar eclipses, changes in the accretion and absorption within the system. In long terms, the light curves are affected by the shifts of locations of the accretion region, changes of from one-pole to -two pole accretion and large variations

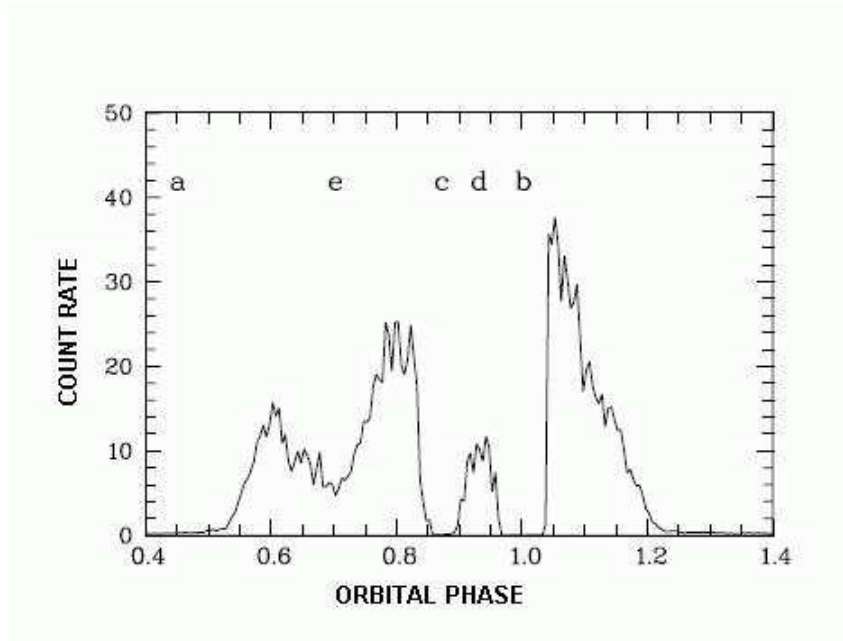


Figure 1.8: ROSAT X-ray Light Curve of the Polar HU Aqr

(Region a corresponds to the occultation of the X-ray source by the white dwarf, region b corresponds to eclipse by the secondary, region c is the narrow dip, region d correspond to absorption by the accretion column and region e correspond to the broad dip. Adapted from Schwope et al. (2001))

in  $\dot{M}$  (Kuulkers et al 2006).

The X-ray light curve of one pole accreting polar has five distinct characteristics which is demonstrated in Figure 1.8. Firstly, there is a clear on-off pattern caused by the occultation of the accretion spot by the white dwarf which does not totally obliterate the X-rays, however reduces the count rate by a great deal (In Figure 1.8 region a). Second, total eclipse of the secondary star which happens at a different phase than the eclipse of the white dwarf (In Figure 1.8 region b). Then there is a narrow dip caused by obscuration by the accretion stream (In Figure 1.8 region c). There is also an absorption from the accretion curtain that reduces the X-ray count rate (In Figure 1.8 region d). Lastly there is a broad dip caused by the absorption or scattering of photons in the accretion column just above the accretion spot (In Figure 1.8 region e). (Schwope et al. 2001, Ramsay et al. 2004)

### 1.4.3 Intermediate Polars

In intermediate polars (IPs) the matter from the donor accretes on the white dwarf on the magnetic poles as in polars. However, due to their low magnetic field strengths a truncated accretion disc may exist in intermediate polars, also their accretion region is more extended than polars. They are the most luminous hard X-ray (up to 90 keV) emitters among CVs with luminosities  $L_X \sim 10^{32} - 10^{33}$  erg/s and show weak or no cyclotron emissions (Mukai 2003, de Martino et al. 2008). In recent years, an increasing number of IPs have been observed by hard X-ray telescopes such as INTEGRAL/IBIS (Barlow et al. 2006; Landi et al. 2009, Scaringi et al. 2010), Swift (Brunschweiler et al. 2009) and SUZAKU (Terada et al. 2008, Yuasa et al. 2010). Although the number of known Polars are twice that of IPs, IPs constitute 90% of the magnetic CVs found in the hard X-ray regime. This is expected since IPs are more luminous in X-rays than Polars due to higher accretion rates (Singh 2013).

Although intermediate polars have smaller magnetic fields and have different accretion geometries than polars, their X-ray production processes are mostly similar. The magnetically channeled accretion material reaches very high speeds up to 3000-10000 km/s forming a shock region near the surface of the white dwarf where the material has temperatures higher than  $10^8$  K. The accreting material then settles on to the white dwarf emitting hard X-rays. (Patterson 1994)

Early work suggested that intermediate polars lack soft X-ray emissions in contrast to polars. The reason was thought to be higher absorption due to larger accretion area, higher accretion rate or lower white dwarf mass than the polars (King & Lasota 1990). However later observations proved some IPs to have soft X-ray components due to reprocessing of hard X-rays by the surface of the white dwarf (not because of the blobby accretion as suggested for some polars) , and reason for the lack of soft X-rays from some IPs would be due to geometrical properties: obscuration by the accretion curtain (Evans & Hellier 2007)

As in the general case for CVs, early low signal-to-noise data are fitted with single temperature (however with higher temperatures in orders of 10 keV) bremsstrahlung along with a partial absorber varying with phase (Norton & Watson 1989). The ap-



proach was further advanced with multi-temperature emission models including reflection effects and partially ionized absorbers which enabled the determination of the white dwarf mass. (Cropper et al. 1998)

Recently, observed soft X-ray component of the spectra, probably resulting from the irradiation of the white dwarf around the accretion curtain, can be fit with blackbody emission with temperatures around several 10s of eVs. Commonly used recent fitting models combines multi-temperature optically thin plasma along with a soft blackbody component and partially covering absorber which takes into account the multi-temperature nature of the hard X-ray emission from the post-shock region, soft X-ray emission and absorption due to the accretion region (Evans et al. 2006, de Martino et al. 2006). A different approach requires photoionized plasma model which has a hard power law-like continuum and line emissions from medium elements for spectral fitting (Mukai et al. 2003).

Line emissions from various elements contribute highly to the spectrum of IPs. Properties of various emission lines from O, Ne, Mg, Si, S, and Fe detected in IPs could be taken as an evidence for the presence of multi-temperature plasma in the shock region. The line ratios provide a basis for constraining the temperature at the shock region and white dwarf mass as well as elemental abundances (Fujimoto & Ishida 1997, Mukai et al. 2001, Mukai et al. 2003). Fe  $K_{\alpha}$  complex also plays an important part in the spectra. Apart from the Iron abundance, Fe  $K_{\alpha}$  line ratios is a tool for the diagnostics for the ionization temperatures in the post-shock plasma. Doppler shifts in these lines give account for the X-ray emitting region. Fe fluorescent line at 6.4 keV could be related to the irradiation of the surface of the white dwarf and hence provides information on the accretion column (Hellier & Mukai 2004, Ezuka & Ishida 1999).

The main characteristic of intermediate polars distinguishing them from the polars is that due to less magnetic field strength, the white dwarf spin is not synchronized with the orbital period. In fact the spin period is much less than the orbital period in these systems. Thus two different periodicities are detected in power spectra of the IPs which is an essential criterion for the classification of a system as an IP. The  $P_{spin}/P_{orb}$  of known IPs peak around 0.1. The systems below this ratio are found to

be harder X-ray emitters with low magnetic fields (Norton et al. 2004, Scaringi et al. 2010).

Basically X-ray light curves folded on the spin period of the white dwarf shows sinusoidal behavior in phase with the optical. The X-ray modulation of the spin period was attributed to the absorption by the accretion column (Hellier et al. 1991). However, later observations indicated that in some IPs the pulse profile show more complex properties such as double peak pulses, saw tooth shape pulses, changing profiles with energy and changes in profiles during outbursts. One is the double peak behavior attributed to short  $P_{spin}$  systems where the magnetic field is weak. Due to weak magnetic field the accretion curtain footprints are wide and the optical depths to X-ray emission within the accretion curtains are therefore lowest in the direction along the magnetic field lines and highest in the direction parallel to the white dwarf surface, such that the emission from the two poles conspires to produce double-peaked X-ray pulse profile. The sawtooth profile is explained by the offset of the magnetic axis from the white dwarf center. The energy dependent spin period modulation is explained by a partially covered absorber system, with a small change in the covering fraction being sufficient to explain the in-phase soft X-ray modulation without affecting the harder X-rays. The change of profiles during outbursts is explained by the disc being pushed inward during the outburst blocking the view to the lower accretion pole and causing larger pulsation during the outburst (Norton et al. 1999, Hellier et al. 1997, Rana et al. 2004, Evans & Hellier 2004,).

Other features seen in X-ray light curves are the eclipses resembling dips in LMXBs over the orbital period related to the photoelectric absorption, X-ray flickering related to the magnetic accretion, and various sideband modulations as an indication of stream fed or stream overflow accretion. (Hellier et al. 1993, Buckley et al. 1997, Hellier & Beardmore 2002, Anzolin et al 2010).

## CHAPTER 2

### EX HYA

Discovered by Kraft (1962), EX Hya has a 98 minute orbital period. The source was classified as an Intermediate Polar when the 67 minutes rotation period of the white dwarf was later identified (Vogt et al. 1980). Estimations from optical (Beuerman et al. 2003; Hellier et. al 1987) and X-ray (Fujimoto & Ishida 1997) observations revealed that the WD has a mass in the  $0.5-0.8 M_{\odot}$  range. Apart from the sub-solar Iron abundance ( $0.6 \pm 0.2$ ), all other elements are compatible with solar abundances (Fujimoto & Ishida 1997). Beuermann et al. (2003) found that the system is at a distance of  $64.5 \pm 1.2$  pc, has an inclination of  $76.0^{\circ} - 77.6^{\circ}$ , has a quiescent accretion luminosity of  $(2.6 \pm 0.6) \times 10^{32}$  erg s<sup>-1</sup>, and a quiescent accretion rate of  $(6.2 \pm 1.5) \times 10^{-11} M_{\odot}$  yr<sup>-1</sup>.

From the lightcurves, EX Hya is observed to have a partial eclipse over the orbital period. Two scenarios were propose the partial eclipse depending on the accretion mode: For two pole accretion, it is the occultation of one of the poles; and for one pole accretion, it is the partial occultation of the accretion column by the secondary star (Rosen, Mason & Cordova, 1988). Belle et al. (2005) suggested that the source has an extended bulge on the outer accretion disc and extended/overflowing material that originates from the hot spot. There are observations of the source is from both outburst and quiescence states. The Doppler tomograms and radial velocities show that the source shows dips and disc overflow during outburst in the optical light curve (Mhlahlo et al. 2007). In line with this scenario, there is disc overflow in the quiescent state (Mhlahlo et al. 2007). X-ray observations also reveal evidence for a a bulge on the accretion disc. There is an extended absorption feature observed from X-ray light

curves in the 1-20 Å range associated with the disc, this broad feature increases at lower wavelengths (Hoogerwerf, Brickhouse & Mauche 2005).

Previously, EX Hya X-ray spectrum has been modeled with various multi-temperature plasma emission models. In one case, four optically thin plasma emission models with different temperatures were utilized (Allan, Hellier & Beardmore, 1998). In a different approach, a cooling-flow model (MKCFLOW) which accounts for a cooling gas from a steady-state condition. It assumes a multi-temperature thermal plasma emission that has a relatively flat emission measure distribution (Mukai et al. 2003).

The X-ray light curve of the source also shows spin modulation which can be explained either by change of absorbing column due to the accretion curtain over the spin phase, or occultation by the white dwarf. Since the accretion column in the system is tall ( $\sim 1 R_{\text{WD}}$ ), occultation scenario is found to be more likely (Allan, Hellier & Beardmore, 1998). There are also variability in the source spectrum over the orbital phase (Cropper et. al 2002), but up until this work, the modulations and spectral variations have not been investigated thoroughly.

## 2.1 Observation and Data

Two sets of XMM-Newton archival data are used in this work. One of the observations was performed on 01 July 2000 (OBS ID: 00111020101) with 30 ksec exposure time, and the other observation which has 57 ksec exposure time was on 11 January 2003 (OBS ID:0057740301). The XMM-Newton Observatory (Jansen et al. 2001) is an X-ray mission that has a pn (Strüder et al., 2001) and two MOS CCD detectors at the focus of three European Photon Imaging Cameras (EPIC), operating in the 0.2-15 keV energy range. XMM-Newton also has Reflecting Grating Spectrometers (RGS), which is a high resolution spectrometer (den Herder et al. 2001) and 30 cm optical monitor instrument (OM) with an optical/UV telescope (Mason et al. 2001).

The first task was checking the pile up in the data with EPATPLOT<sup>1</sup> tool in SAS. Only EPIC pn data was utilized throughout the analysis due to pile up in the EPIC MOS

---

<sup>1</sup> See <http://xmm.esac.esa.int/sas/current/documentation/threads/epatplot.shtml>

data. The 2000 data was obtained in the small window mode, and in the 0.2-10 keV energy range it has a count rate of  $40.1 \pm 0.04$  count  $s^{-1}$ . The 2003 observation is obtained in the full frame mode, and the source has an offset of 14 arc-minutes from the center. The net count rate of source in the 0.2-10 keV energy interval for this observation is  $9.7 \pm 0.01$  count  $s^{-1}$ . The difference in count rates in both observation is attributed to the offset in the object position in the observation.

In order to perform the spectral and temporal analysis, standard pipeline processing was carried out for both observations, using the XMM-Newton Science Analysis Software (SAS) version 8.0.0. By utilizing the SAS tool XMMSELECT, light curves and spectra were extracted from the source. For 2000 data, a circular region with 38.8 arc-seconds was used in order to extract photons from both the source and the background. For the 2003 observation, due to the offset, an elliptical region was chosen with 60 arc-second semi-major axis and 23.3 arc-second semi-minor axis, tilted at 320 degrees for source and background event extraction. Single and double pixel event data was used. Spin and orbital phase columns were created using PHASECALC tool in SAS. For the purpose of phase resolved spectroscopy, spectra were extracted for each 0.1 phase interval from the event files using ESPECGET tool in SAS. For further spectral analysis, XSPEC 12.2.1 (Arnaud 1996) was utilized.

## 2.2 Average Spectrum

Average spectra from 0.2-10.0 keV range for both 2000 and 2003 observations were extracted according to the procedure explained in the previous section. Spectrum from the 2000 data was grouped so that there is a minimum of 300 count for each energy bin. For the 2003 data, the minimum count for each energy bin is 200. The fits to the spectra were carried out in XSPEC, in the 0.2-10.0 keV energy band.

For the initial fit to the average spectra, a composite model proposed by Allan et al. (1998) was put into use. The model consisted of multiple plasma emissions in collisional equilibrium (MEKAL model in XSPEC) with different temperatures. However, including even up to 4 different MEKAL components did not yield fits with reduced  $\chi^2$  less than 2. In the next step, as suggested by Mukai et al. (2003), a cooling flow

model with variable abundances was used in the fits (VMCFLOW model in XSPEC) which in turn also did improve the fits. Finally, the two approaches were combined, by including two MEKAL models at 0.64 keV and 1.6 keV together with the cooling flow model VMCFLOW. A simple absorber and a partial covering absorber (TBABS and PCFABS) were also included to account for the absorption from the interstellar medium and the system itself.

This composite model yielded varying residuals around strong lines in the spectrum, Fe complex around 6.7 in particular which we attribute to CTI effects. Therefore, in order to account for the  $\text{Fe}\alpha$  line complex, we modeled them separately. The Fe abundance in VMCFLOW model was reduced to 0.2 times the solar, and Gaussian emission lines at 6.7 keV and 6.9 keV were added to the model. This way, each line could be modeled individually. Reducing Fe abundance had no effect on the rest of the spectral fit, since VMCFLOW component affects only the harder part of the spectrum. In order to reduce the high sigma fluctuations in the residuals at certain energies, additional Gaussian emission lines were added to the model. These lines have centroids at 7.8 keV, 0.58 keV and 0.78 keV for the 2000 spectrum and 7.8 keV, 6.4 keV and 0.58 keV for the 2003 spectrum. According to CHIANTI atomic database, the lines at 0.58 keV, 0.78 keV and 7.8 keV correspond to O VII, O VIII and Fe XXV  $K\beta$  transitions respectively. Independent Gaussian profiles were used for these lines since they could not be modeled by increasing the abundance parameters in the composite model. The spectra and corresponding fits are displayed in Figure 2.1 and the best fit parameters are presented in Table 2.1.

The flux calculated from the fits are  $1.43 \times 10^{-10}$  for 2000 and  $1.24 \times 10^{-10}$  erg  $\text{cm}^{-2} \text{s}^{-1}$  for 2003 observations. Taking the distance as 64.5 pc, the luminosities can be calculated as  $6.7 \times 10^{31}$  erg  $\text{s}^{-1}$  and  $5.8 \times 10^{31}$  erg  $\text{s}^{-1}$  for 2000 and 2003 respectively. We also calculated the accretion rate of the system, using  $L = \dot{M} R / 2$  relation. Taking  $0.5 M_{\odot}$  as the white dwarf mass and  $0.95 R_{\odot}$  as white dwarf radius (Beuermann et al. 2003), the accretion rate yields values of  $5.75 \times 10^{-11} M_{\odot} \text{yr}^{-1}$  for 2000 and  $5.0 \times 10^{-11} M_{\odot} \text{yr}^{-1}$  2003 data. These values are underestimations, however, since inner radius of the disc does not extend all the way down to the surface the of white dwarf.

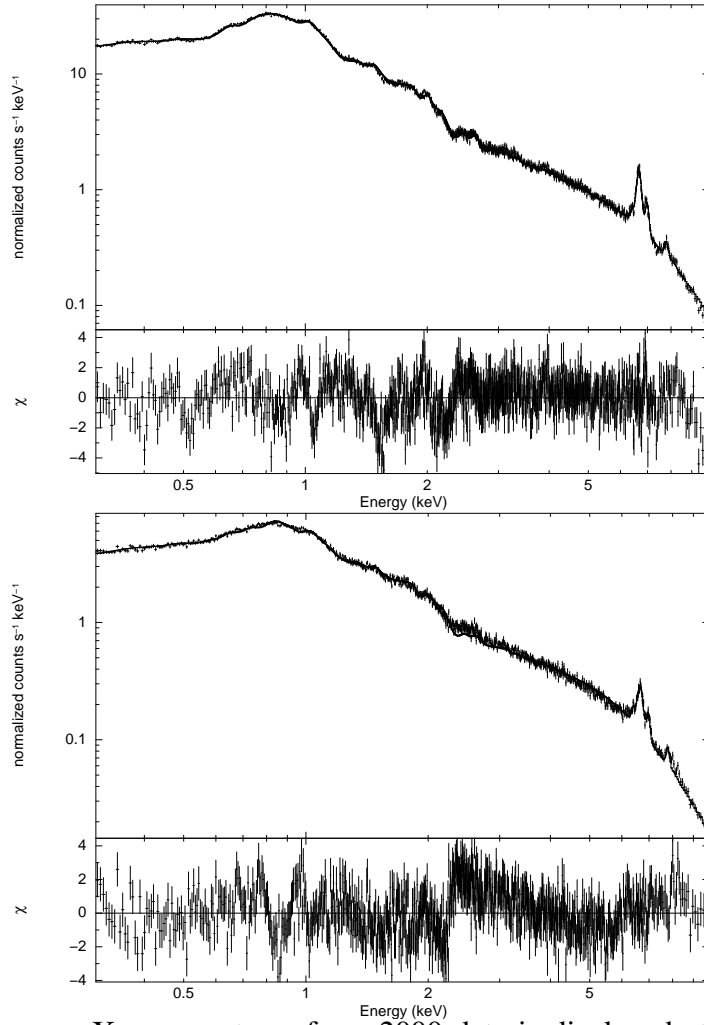


Figure 2.1: Average X-ray spectrum from 2000 data is displayed at the top panel, and average X-ray spectrum from 2003 data is displayed at the bottom panel (see Table 2.1 for details).

Table 2.1: Best fit parameters to the average spectra from year 2000 and 2003 in the 0.3-10 keV energy range. The fitted composite model consists of two plasma emission models at collisional equilibrium and with different temperatures (MEKAL), two Gaussians emission lines with centroids at 6.7 keV, and 6.9 keV, a cooling-flow plasma emission model with variable abundances (VMCFLOW), a partial covering absorber (PCFABS) and a simple absorber (TBABS). Additional Gaussian profiles were used for both spectra where needed.  $N_{\text{H}}$  is the absorbing neutral Hydrogen column density, CoverFrac stands for the covering fraction of the partially covering absorber. Parameter errors displayed correspond to  $2\sigma$  confidence level for a single parameter.

Model	Component	2000 Total Spectrum	2003 Total Spectrum
tbabs	$N_{\text{H}} (\times 10^{22} \text{ atoms/cm}^2)$	$0.0097^{+0.0007}_{-0.0007}$	$0.0092^{+0.0025}_{-0.0035}$
pcfabs	$N_{\text{H}} (\times 10^{22} \text{ atoms/cm}^2)$	$0.86^{+0.17}_{-0.16}$	$0.17^{+0.06}_{-0.04}$
	CoverFrac	$0.22^{+0.01}_{-0.01}$	$0.35^{+0.7}_{-0.5}$
MEKAL1	kT (keV)	$0.66^{+0.01}_{-0.01}$	$0.63^{+0.01}_{-0.01}$
	norm ( $\times 10^{-3}$ )	$4.8^{+0.2}_{-0.2}$	$2.9^{+0.2}_{-0.1}$
MEKAL2	kT (keV)	$1.58^{+0.05}_{-0.05}$	$1.65^{+0.07}_{-0.08}$
	norm ( $\times 10^{-3}$ )	$7.8^{+0.7}_{-0.7}$	$4.3^{+0.5}_{-0.5}$
Gaussian1 (6.7 keV)	sigma (keV)	$0.070^{+0.006}_{-0.005}$	$0.076^{+0.009}_{-0.010}$
	norm ( $\times 10^{-4}$ )	$2.8^{+0.1}_{-0.1}$	$2.6^{+0.2}_{-0.2}$
Gaussian2 (6.9 keV)	sigma (keV)	$0.042^{+0.016}_{-0.020}$	$0.064^{+0.035}_{-0.040}$
	norm ( $\times 10^{-5}$ )	$6.3^{+0.6}_{-0.6}$	$5.8^{+1.1}_{-1.1}$
Gaussian3 (6.4 keV)	sigma (keV)	N/A	$0.11^{+0.04}_{-0.04}$
	norm ( $\times 10^{-5}$ )	N/A	$4.5^{+1.1}_{-1.0}$
Gaussian4 (7.8 keV)	sigma (keV)	$0.06^{+0.06}_{-0.06}$	$0.51^{+0.29}_{-0.14}$
	norm ( $\times 10^{-5}$ )	$2.7^{+1.0}_{-0.7}$	$18.2^{+7.6}_{-4.6}$
Gaussian5 (0.58 keV)	sigma (keV)	0 (frozen)	0 (frozen)
	norm ( $\times 10^{-4}$ )	$3.9^{+0.6}_{-0.6}$	$5.2^{+0.8}_{-0.8}$
Gaussian6 (0.78 keV)	sigma (keV)	0 (frozen)	N/A
	norm ( $\times 10^{-4}$ )	$5.0^{+0.6}_{-0.6}$	N/A
VMCFLOW	LowT	$3.4^{+0.6}_{-0.6}$	$9.0^{+1.2}_{-1.0}$
	HighT	$29.1^{+3.6}_{-3.4}$	$59.2^{+2.4}_{-2.1}$
	$\chi^2_{\nu}$	1.70 (956 d.o.f.)	1.66 (903 d.o.f.)



Table 2.2: Best fit parameters for the common Gaussian emission lines in the EX Hya spectra in 2000 and 2003.

Emission Line	Component	2000 Spectrum	2003 Spectrum
Gaussian1 (6.7 keV)	line center (keV)	6.7 (fixed)	6.7 (fixed)
	sigma (keV)	$0.070^{+0.006}_{-0.005}$	$0.076^{+0.009}_{-0.010}$
	norm ( $\times 10^{-4}$ )	$2.8^{+0.1}_{-0.1}$	$2.6^{+0.2}_{-0.2}$
Gaussian2 (6.9 keV)	line center (keV)	6.9 (fixed)	6.9 (fixed)
	sigma (keV)	$0.042^{+0.016}_{-0.020}$	$0.064^{+0.035}_{-0.040}$
	norm ( $\times 10^{-5}$ )	$6.3^{+0.6}_{-0.6}$	$5.8^{+1.1}_{-1.1}$
Gaussian3 (7.8 keV)	line center (keV)	$7.8^{+0.3}_{-0.3}$	$7.9^{+0.8}_{-0.8}$
	sigma (keV)	$0.059^{+0.063}_{-0.059}$	$0.51^{+0.29}_{-0.14}$
	norm ( $\times 10^{-5}$ )	$2.6^{+1.0}_{-0.7}$	$18.2^{+7.7}_{-4.6}$

The emission line centered around 7.8 keV is an unusual feature, observed in both spectra. We focused on the 5-10 keV region in order to investigate this feature in detail. We fitted a power law continuum and Gaussian emission profiles at around 6.7 keV, 6.9 keV and 7.8 keV in both spectra. Table 2.2 shows the best fit parameters and corresponding errors. We find an emission line centered around  $7.8^{+0.3}_{-0.3}$  keV with a line width  $\sigma = 0.06^{+0.06}_{-0.06}$  keV for 2000, and centered around  $7.9^{+0.8}_{-0.8}$  with a line width  $\sigma = 0.5^{+0.3}_{-0.1}$  for 2003 observations. We interpret this line as the Fe XXV  $K\beta$  emission line. In the line widths for 6.9 keV and 7.8 keV are significantly higher in 2003 observation, but 6.7 keV line width has similar value both in 2000 and 2003.

### 2.3 Orbital Phase-Resolved Spectroscopy

In this chapter, we perform for the first time, a detailed orbital phase-resolved X-ray spectroscopy of EX Hya. The ephemeris  $T_0 = 2437699.94179+0.068233846(4)E$  (Hellier & Sproats, 1992) was used in both observations while creating phase columns in the data. In the next step, 10 spectra were extracted for each observations, with 0.1 phase interval, spanning from phase 0 to phase 1. In order to improve the statistics of the data, the extracted spectra were grouped with minimum 100 counts in each energy bin, and only the energy channels between 0.3 keV and 10.0 keV were used.

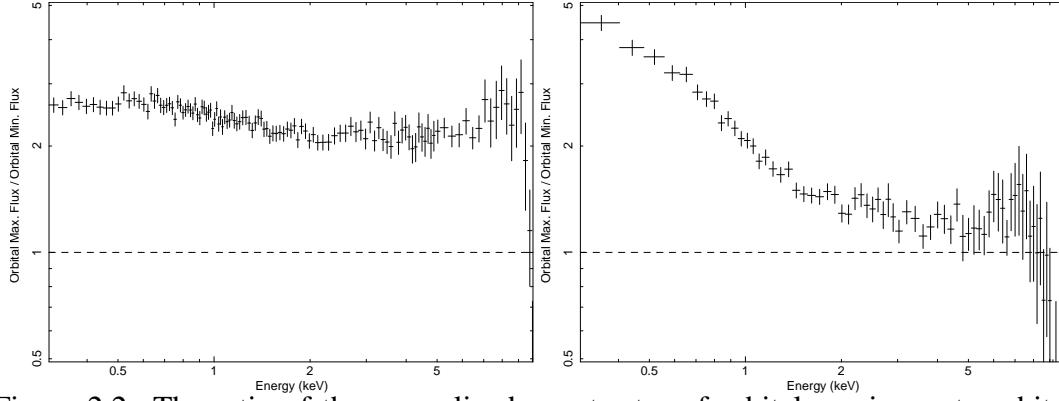


Figure 2.2: The ratio of the normalized count rates of orbital maximum to orbital minimum against energy. The left hand panel shows the 2000 data and the right hand panel shows the 2003 data .

Firstly, we extracted spectra from the orbital minimum (phases between 0.9-1.1) and orbital maximum (phases between 0.6-0.8) for each observation. Then, in order to investigate the absorption and occultation effects, we plotted the ratio of orbital maximum spectrum to the orbital minimum spectrum against energy. As shown in Figure 2.2, while the spectral ratio values are always above 1, they display a power-law decline towards higher energies, indicating spectral variation. The decline in 2003 data is more prominent than 2000, indicating a substantial change in the absorption structure in the system from orbital minimum to maximum.

Similar to the phase average spectra, fitting the spectra by using multiple MEKAL models or single VMCFLOW model resulted in large reduced  $\chi^2$  values. Hence a combination of VMCFLOW model with MEKAL model was used, in tandem with a simple photoelectric absorber model (WABS) and the abundances were kept at solar values. This method, however still resulted in fits with high reduced  $\chi^2$  due to fluctuating residuals around 6.7 keV Fe emission line complex. Hence, we reduced the Fe abundance in the continuum models and modeled the Fe emission lines separately, by adding Gaussian profiles at 6.7 keV and 6.9 keV where necessary.

The composite model used for the analysis of 2000 data includes two MEKAL components at different temperatures, a VMCFLOW model, a simple photoelectric absorber (WABS) and 3 Gaussian emission profiles for Fe lines. The best fit parameters and corresponding errors are displayed in Table 2.3 and in Figure 2.3, a selection of spectral parameters are plotted against the orbital phase. Figure 2.4 shows the spec-

tra and the corresponding fitting model for orbital minima (phase 0.9) and maxima (phase 0.3). Since a simple absorber was sufficient to fit the spectrum, partial covering absorber was not necessary. Neutral Hydrogen column density ( $N_{\text{H}}$ ) displays significant variation over the orbital phase. It reaches to the maximum value on the orbital minimum, indicating absorber effects are responsible for the spectral variations over the orbit. In addition, low temperature of the cooling flow ( $LowT$  parameter of VMCFLOW) shows a similar behaviour, reaching maximum at orbital phases where the flux is minimum. On the other hand, high temperature parameter of the cooling flow ( $HighT$ ) shows a behaviour in direct correlation with the flux over the orbital phase, implying the effect of scattering. The temperature parameters of MEKAL components are almost constant over the orbital period, with normalizations varying slightly with the in line with the orbital phase. The Gaussian emission line centered at 6.7 keV only shows a slight drop around phases 0.6-0.7. This indicates that over the orbital motion, the region where this line is produced is in the line of sight at all times.

The same composite model was used for the orbital phase resolved spectral analysis of the 2003 data. It was comprised of two MEKAL models at different temperatures, a VMCFLOW model, a simple cold absorber model (WABS) and three different Gaussians profiles Fe lines at 6.4 keV, 6.7 keV and 6.9 keV. Parameters and corresponding errors from the best fits are presented in Table 2.4 and plot of selected parameters against the orbital phase are displayed in Figure 2.5. Figure 2.6 shows the spectra and the best fit models at the orbital maximum (phase 0.4) and orbital minimum (phase 0). The fits yielded reduced  $\chi^2$  values below 2 at all phases. Some of the parameters distinctly vary over the orbital phase. The absorbing column parameter  $N_{\text{H}}$  and the  $LowT$  parameter of the VMCFLOW model vary inversely with the X-ray flux over the orbital phase. At the orbital maxima (phases 0.4-0.8) they have lower values, and their values peak at the orbital minima (phases 0.9-1.3). This feature is an indication of absorption of the X-rays from the source during the orbital minima. Also, since the absorption effects the softer X-rays more, hardening in the spectra is observed. This absorption component has a less prominent impact in hard X-rays, and hence we observe no distinct variation in the  $HighT$  parameter of VMCFLOW model.

Temperature and normalization parameters of the MEKAL component of the com-

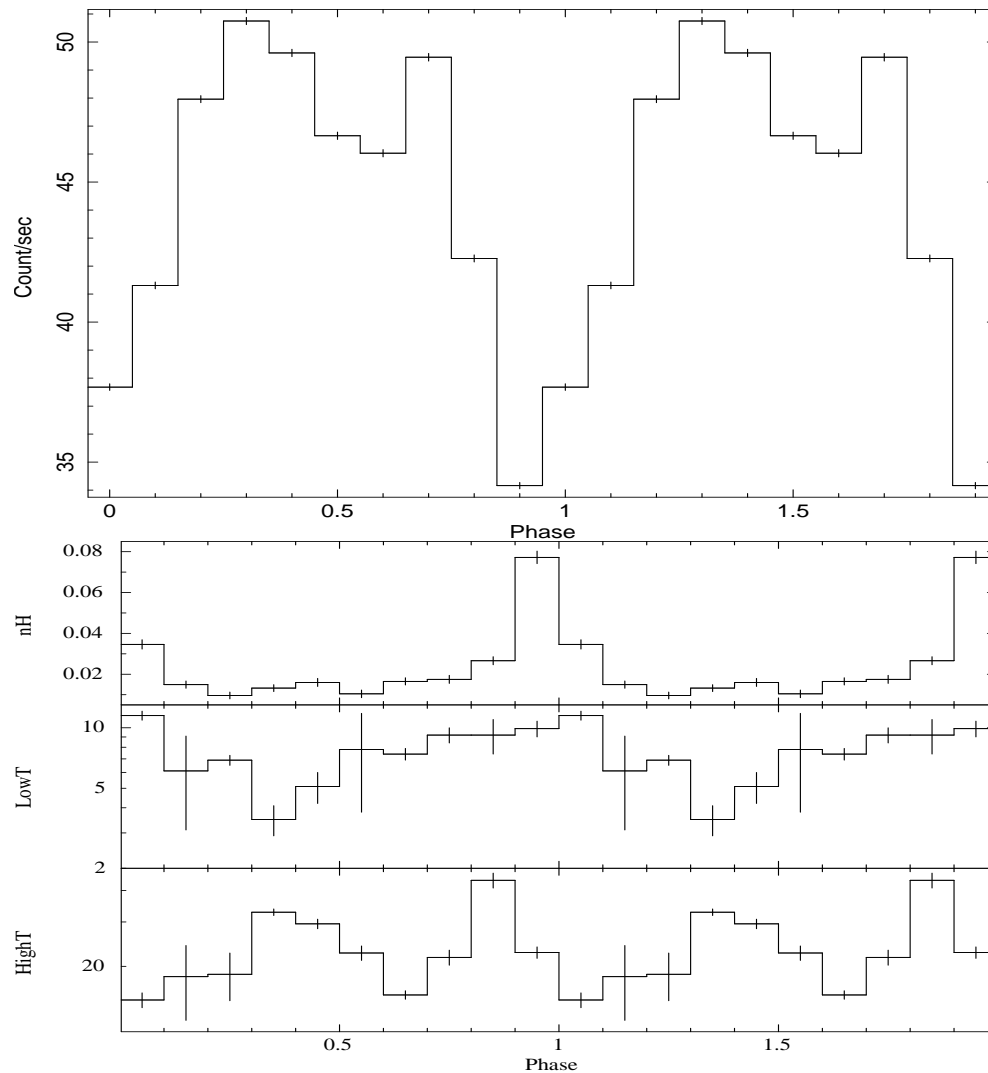


Figure 2.3: The X-ray light curve (2000 observation) folded over the orbital period using the ephemeris  $T = 2437699.94179 + 0.068233846(4)E$  at the top, and spectral parameters derived from the best fits to the orbital phase-resolved spectra plotted over the orbital phase. The temperatures are given in keV.

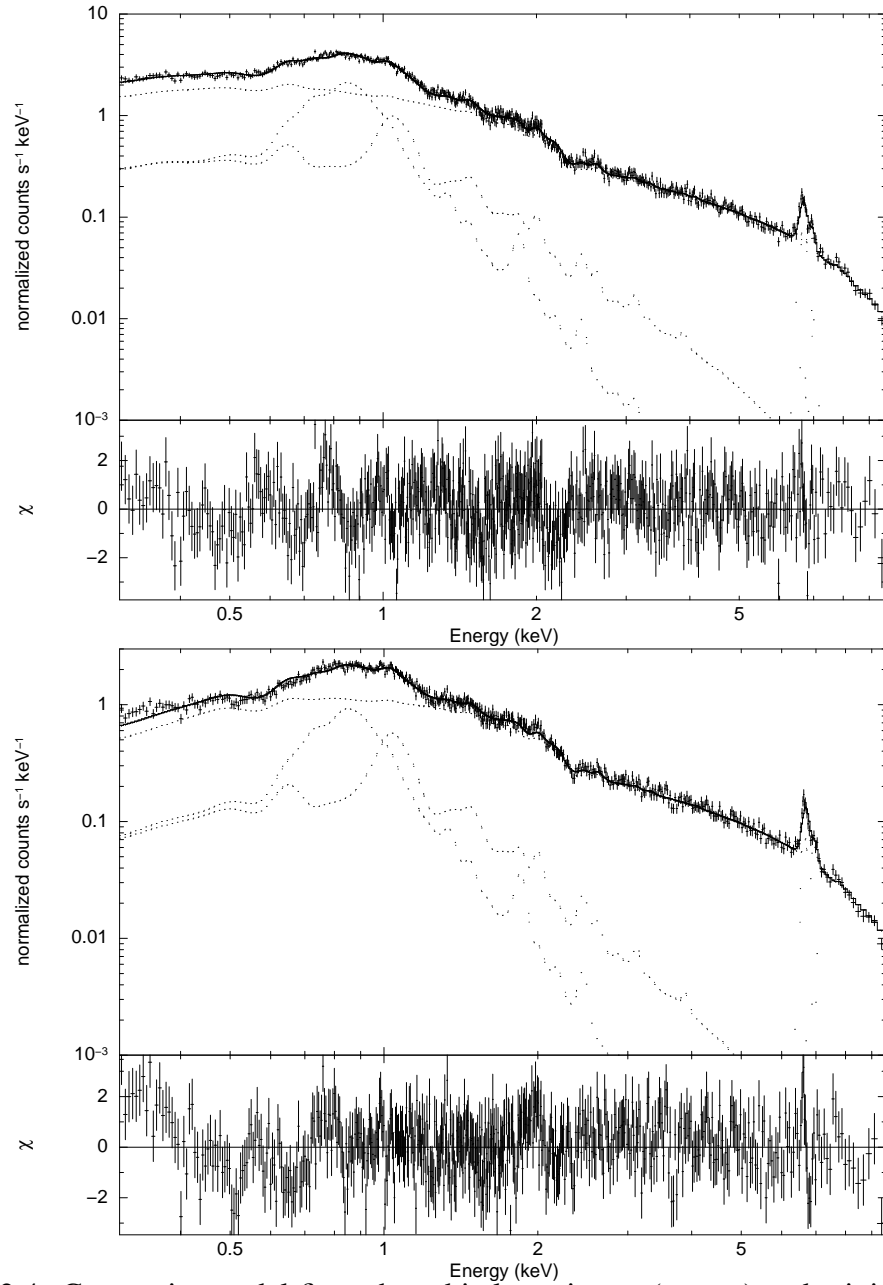


Figure 2.4: Composite model fit to the orbital maximum (on top) and minimum (at the bottom) of EX Hya from 2000 data.

Table 2.3: Spectral parameters derived from the best fits to each spectra extracted from each 0.1 orbital phase interval for the year 2000 observation. The corresponding parameter errors are at  $2\sigma$  confidence level.

Model	Component	0.1	0.2	0.3	0.4	0.5
wabs	$N_{\text{H}} (\times 10^{-22})$	$0.035^{+0.002}_{-0.002}$	$0.015^{+0.002}_{-0.002}$	$0.010^{+0.002}_{-0.002}$	$0.013^{+0.002}_{-0.002}$	$0.016^{+0.002}_{-0.003}$
MEKAL1	kT (keV)	$0.64^{+0.01}_{-0.01}$	$0.62^{+0.02}_{-0.02}$	$0.63^{+0.01}_{-0.01}$	$0.64^{+0.01}_{-0.01}$	$0.63^{+0.01}_{-0.01}$
	Norm ( $\times 10^{-4}$ )	$3.5^{+0.1}_{-0.1}$	$4.3^{+0.2}_{-0.2}$	$4.7^{+0.2}_{-0.2}$	$4.8^{+0.2}_{-0.2}$	$4.3^{+0.2}_{-0.2}$
MEKAL2	kT (keV)	$1.57^{+0.12}_{-0.14}$	$1.37^{+0.06}_{-0.07}$	$1.56^{+0.11}_{-0.13}$	$1.59^{+0.12}_{-0.17}$	$1.60^{+0.13}_{-0.17}$
	Norm ( $\times 10^{-4}$ )	$5.9^{+0.9}_{-0.9}$	$5.6^{+0.2}_{-0.2}$	$7.9^{+1.0}_{-1.1}$	$7.5^{+1.2}_{-1.3}$	$6.4^{+1.2}_{-1.2}$
VMCFLOW	LowT (keV)	$11.5^{+0.7}_{-0.5}$	$6.1^{+3.0}_{-2.8}$	$6.9^{+0.4}_{-0.4}$	$3.5^{+0.6}_{-0.5}$	$5.1^{+0.9}_{-0.9}$
	HighT (keV)	$14.7^{+0.8}_{-1.2}$	$18.2^{+9.5}_{-3.1}$	$18.6^{+5.7}_{-3.4}$	$32.8^{+1.0}_{-0.9}$	$29.5^{+1.4}_{-1.2}$
Gaussian1 (6.7 keV)	$\sigma$ (keV)	$0.11^{+0.02}_{-0.02}$	$0.11^{+0.03}_{-0.2}$	$0.11^{+0.04}_{-0.01}$	$0.11^{+0.03}_{-0.02}$	$0.14^{+0.03}_{-0.03}$
	Norm ( $\times 10^{-5}$ )	$2.7^{+0.5}_{-0.3}$	$5.7^{+0.4}_{-0.2}$	$3.2^{+0.5}_{-0.4}$	$3.1^{+0.4}_{-0.4}$	$3.4^{+0.6}_{-0.5}$
Gaussian2 (6.9 keV)	$\sigma$ (keV)	0	0	0	0	0
	Norm ( $\times 10^{-6}$ )	$3.5^{+1.9}_{-2.5}$	$3.6^{+2.0}_{-2.5}$	$3.8^{+2.0}_{-2.5}$	$2.8^{+2.0}_{-2.5}$	$2.6^{+3.0}_{-1.8}$
	$\chi^2_{\nu}$ (d.o.f)	1.35 (510)	1.31 (557)	1.29 (574)	1.29 (585)	1.20 (548)
Model	Component	0.6	0.7	0.8	0.9	1.0
wabs	$N_{\text{H}} (\times 10^{-22})$	$0.010^{+0.002}_{-0.002}$	$0.016^{+0.002}_{-0.002}$	$0.018^{+0.002}_{-0.002}$	$0.027^{+0.002}_{-0.002}$	$0.077^{+0.003}_{-0.003}$
MEKAL1	kT (keV)	$0.63^{+0.02}_{-0.02}$	$0.65^{+0.01}_{-0.01}$	$0.62^{+0.02}_{-0.02}$	$0.63^{+0.01}_{-0.02}$	$0.64^{+0.02}_{-0.03}$
	Norm ( $\times 10^{-4}$ )	$3.8^{+0.1}_{-0.1}$	$4.1^{+0.2}_{-0.2}$	$3.7^{+0.2}_{-0.2}$	$2.8^{+0.1}_{-0.2}$	$2.6^{+0.2}_{-0.2}$
MEKAL2	kT (keV)	$1.59^{+0.13}_{-0.15}$	$1.61^{+0.12}_{-0.19}$	$1.42^{+0.16}_{-0.03}$	$1.42^{+0.09}_{-0.11}$	$1.43^{+0.14}_{-0.09}$
	Norm ( $\times 10^{-4}$ )	$5.5^{+1.0}_{-0.9}$	$6.2^{+1.3}_{-1.6}$	$5.7^{+1.0}_{-0.4}$	$3.8^{+0.8}_{-0.5}$	$4.1^{+0.9}_{-0.4}$
VMCFLOW	LowT (keV)	$7.8^{+5.6}_{-2.5}$	$7.4^{+0.5}_{-0.5}$	$9.2^{+1.1}_{-0.7}$	$9.2^{+2.2}_{-1.4}$	$9.9^{+0.8}_{-0.9}$
	HighT (keV)	$22.6^{+1.6}_{-1.0}$	$15.4^{+0.6}_{-0.7}$	$21.7^{+2.0}_{-1.0}$	$43.9^{+3.9}_{-2.6}$	$22.7^{+1.3}_{-1.2}$
Gaussian1 (6.7 keV)	$\sigma$ (keV)	$0.09^{+0.02}_{-0.02}$	$0.06^{+0.03}_{-0.04}$	$0.10^{+0.07}_{-0.02}$	$0.12^{+0.03}_{-0.02}$	$0.09^{+0.02}_{-0.02}$
	Norm ( $\times 10^{-5}$ )	$2.9^{+0.4}_{-0.3}$	$2.2^{+0.4}_{-0.4}$	$2.9^{+0.2}_{-0.3}$	$3.6^{+0.4}_{-0.4}$	$3.1^{+0.4}_{-0.3}$
Gaussian2 (6.7 keV)	$\sigma$ (keV)	0	0	0	0	0
	Norm ( $\times 10^{-6}$ )	$5.5^{+2.1}_{-2.2}$	$5.1^{+1.2}_{-2.1}$	$2.2^{+1.9}_{-2.2}$	$4.2^{+2.1}_{-1.2}$	$3.1^{+2.3}_{-1.8}$
	$\chi^2_{\nu}$ (d.o.f)	1.23 (522)	1.23 (538)	1.33 (531)	1.40 (501)	1.30 (531)

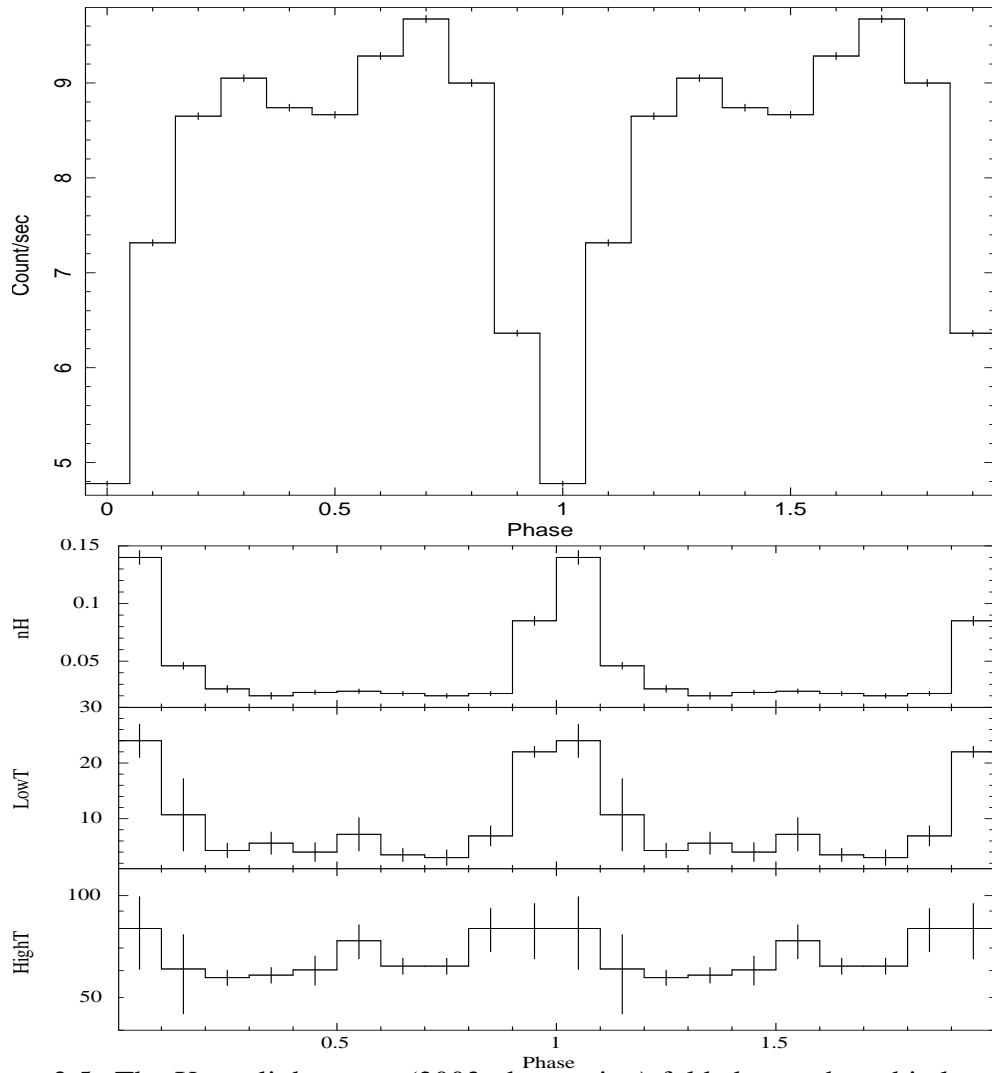


Figure 2.5: The X-ray light curve (2003 observation) folded over the orbital period using the ephemeris  $T = 2437699.94179 + 0.068233846(4)E$  at the top, and spectral parameters derived from the best fits to the orbital phase-resolved spectra plotted over the orbital phase. The temperatures are given in keV.

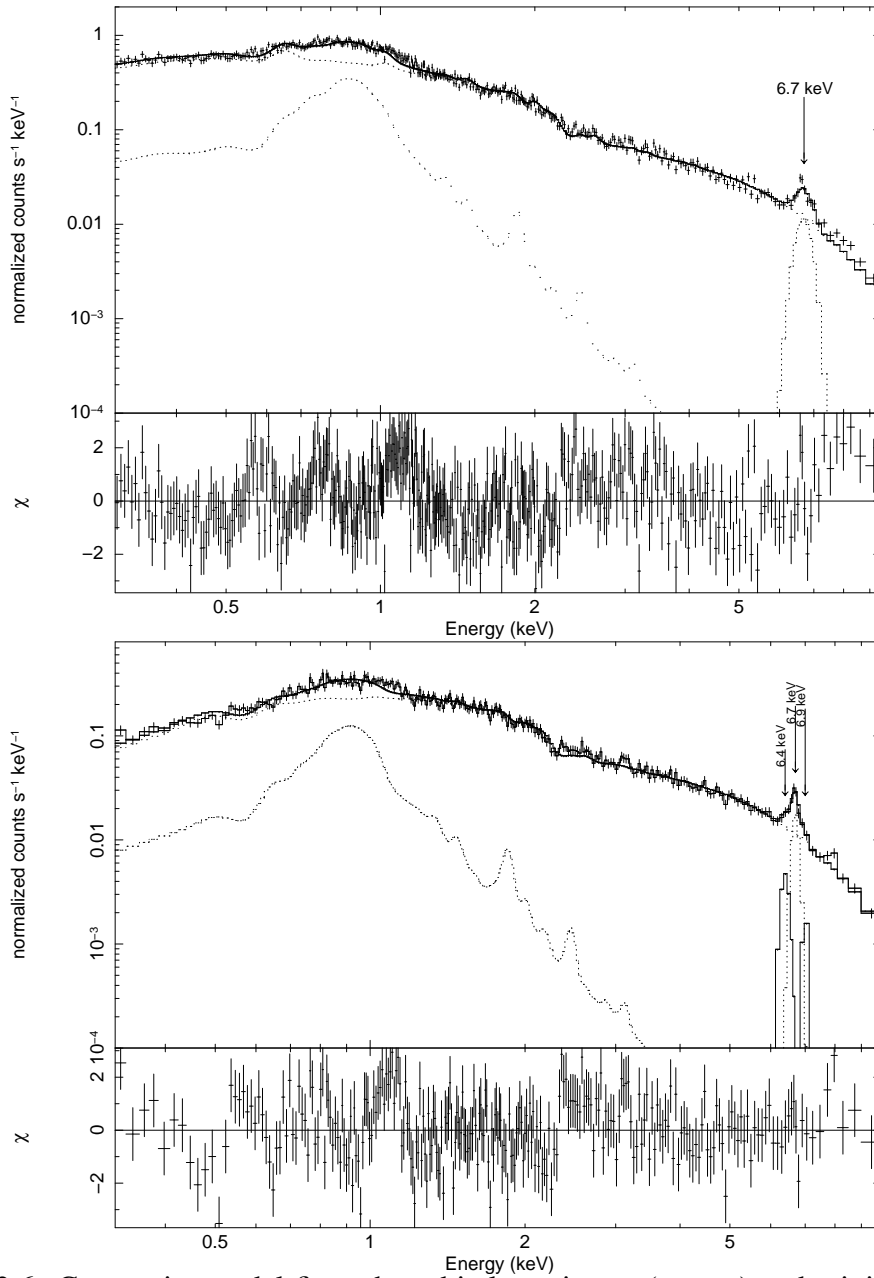


Figure 2.6: Composite model fit to the orbital maximum (on top) and minimum (at the bottom) of EX Hya from 2000 data. Note that 6.4 keV and 6.9 keV emission lines are absent in the orbital maximum spectral fit.



Table 2.4: Spectral parameters derived from the best fits to each spectra extracted from each 0.1 orbital phase interval for the year 2003 observation. The corresponding parameter errors are at  $2\sigma$  confidence level.

Model	Component	0.1	0.2	0.3	0.4	0.5
wabs	$N_{\text{H}} (\times 10^{-22})$	$0.142^{+0.006}_{-0.006}$	$0.046^{+0.003}_{-0.003}$	$0.026^{+0.003}_{-0.003}$	$0.020^{+0.002}_{-0.002}$	$0.024^{+0.002}_{-0.002}$
MEKAL1	kT (keV)	$0.63^{+0.04}_{-0.06}$	$0.65^{+0.02}_{-0.02}$	$0.61^{+0.03}_{-0.03}$	$0.65^{+0.02}_{-0.02}$	$0.64^{+0.02}_{-0.02}$
	Norm ( $\times 10^{-4}$ )	$1.2^{+0.1}_{-0.2}$	$2.6^{+0.2}_{-0.2}$	$2.6^{+0.3}_{-0.2}$	$3.3^{+0.2}_{-0.2}$	$2.7^{+0.2}_{-0.1}$
MEKAL2	kT (keV)	$1.53^{+0.18}_{-0.19}$	$1.80^{+0.26}_{-0.13}$	$1.48^{+0.12}_{-0.08}$	$1.72^{+0.09}_{-0.09}$	$1.65^{+0.14}_{-0.12}$
	Norm ( $\times 10^{-4}$ )	$2.3^{+0.6}_{-0.6}$	$4.3^{+1.3}_{-0.8}$	$3.9^{+0.9}_{-0.8}$	$5.2^{+0.9}_{-0.8}$	$3.6^{+0.8}_{-0.8}$
VMCFLOW	LowT (keV)	$25.7^{+1.0}_{-5.0}$	$10.8^{+19.5}_{-6.6}$	$4.3^{+1.7}_{-0.9}$	$5.7^{+3.4}_{-1.6}$	$4.1^{+1.4}_{-1.9}$
	HighT (keV)	$79.9^{<}_{-19.4}$	$60.8^{+12.3}_{-20.2}$	$57.2^{+4.4}_{-2.9}$	$58.2^{+3.2}_{-3.1}$	$60.4^{+3.8}_{-8.5}$
Gaussian1 (6.7 keV)	$\sigma$ (keV)	$0.07^{+0.03}_{-0.03}$	$0.10^{+0.06}_{-0.04}$	$0.10^{+0.09}_{-0.04}$	$0.25^{+0.08}_{-0.05}$	$0.19^{+0.06}_{-0.05}$
	Norm ( $\times 10^{-5}$ )	$3.1^{+0.6}_{-0.5}$	$2.3^{+1.2}_{-0.5}$	$1.4^{+0.9}_{-0.6}$	$3.8^{+0.9}_{-0.8}$	$3.2^{+0.7}_{-0.7}$
Gaussian2 (6.9 keV)	$\sigma$ (keV)	0	0	0	0	0
	Norm ( $\times 10^{-6}$ )	$2.1^{+3.5}_{-2.1}$	$5.1^{+3.7}_{-5.1}$	$1.5^{+0.5}_{-0.3}$	$< 0.000037$	$< 0.000021$
Gaussian3 (6.4 keV)	$\sigma$ (keV)	$0.08^{+0.11}_{-0.08}$	$0.09^{+0.44}_{-0.09}$	$0.16^{+0.08}_{-0.06}$	0	0
	Norm ( $\times 10^{-6}$ )	$8.7^{+4.5}_{-5.2}$	$6.3^{+4.7}_{-3.2}$	$14.9^{+4.8}_{-7.3}$	$< 0.0018$	$< 0.000021$
	$\chi^2_{\nu}$ (d.o.f.)	1.27 (254)	1.22 (363)	1.40 (380)	1.26 (386)	1.43 (374)
Model	Component	0.6	0.7	0.8	0.9	1.0
wabs	$N_{\text{H}} (\times 10^{-22})$	$0.025^{+0.003}_{-0.002}$	$0.022^{+0.002}_{-0.002}$	$0.020^{+0.002}_{-0.002}$	$0.022^{+0.002}_{-0.002}$	$0.085^{+0.004}_{-0.004}$
MEKAL1	kT (keV)	$0.65^{+0.2}_{-0.2}$	$0.63^{+0.02}_{-0.03}$	$0.63^{+0.02}_{-0.02}$	$0.62^{+0.03}_{-0.03}$	$0.67^{+0.07}_{-0.08}$
	Norm ( $\times 10^{-4}$ )	$2.7^{+0.2}_{-0.2}$	$3.0^{+0.2}_{-0.2}$	$3.1^{+0.2}_{-0.2}$	$2.5^{+0.2}_{-0.3}$	$1.0^{+0.2}_{-0.2}$
MEKAL2	kT (keV)	$1.64^{+0.11}_{-0.13}$	$1.36^{+0.07}_{-0.07}$	$1.66^{+0.12}_{-0.14}$	$1.35^{+0.08}_{-0.07}$	$1.27^{+0.16}_{-0.14}$
	Norm ( $\times 10^{-4}$ )	$3.9^{+0.8}_{-0.8}$	$2.9^{+0.6}_{-0.4}$	$4.3^{+0.9}_{-0.9}$	$2.4^{+0.7}_{-0.5}$	$1.2^{+0.3}_{-0.4}$
VMCFLOW	LowT (keV)	$7.3^{+3.4}_{-2.6}$	$3.5^{+1.3}_{-1.0}$	$3.1^{+1.3}_{-1.4}$	$6.9^{+0.8}_{-2.0}$	$24.0^{+0.8}_{-1.0}$
	HighT (keV)	$73.5^{+4.5}_{-12.5}$	$62.0^{+3.6}_{-3.3}$	$62.0^{+3.7}_{-3.1}$	$79.9^{<}_{-11.8}$	$79.9^{<}_{-14.9}$
Gaussian1 (6.7 keV)	$\sigma$ (keV)	$0.15^{+0.06}_{-0.03}$	$0.20^{+0.05}_{-0.04}$	$0.22^{+0.05}_{-0.04}$	$0.06^{+0.04}_{-0.03}$	$0.08^{+0.04}_{-0.04}$
	Norm ( $\times 10^{-5}$ )	$3.1^{+0.5}_{-0.8}$	$4.4^{+0.8}_{-0.7}$	$4.1^{+0.4}_{-0.7}$	$2.4^{+0.5}_{-0.8}$	$2.2^{+0.6}_{-0.5}$
Gaussian2 (6.9 keV)	$\sigma$ (keV)	0	0	0	0	0
	Norm ( $\times 10^{-6}$ )	$< 0.00016$	$< 2.3$	$< 1.3$	$8.3^{+3.8}_{-3.8}$	$7.9^{+3.7}_{-4.1}$
Gaussian3 (6.4 keV)	$\sigma$ (keV)	0	0	0	$0.0^{+0.3}_{>}$	$0.10^{+0.06}_{-0.05}$
	Norm ( $\times 10^{-6}$ )	$< 0.84$	$< 0.0022$	$< 0.0013$	$5.2^{+8.8}_{-3.0}$	$12.1^{+4.9}_{-5.0}$
	$\chi^2_{\nu}$ (d.o.f.)	1.17 (385)	1.41 (392)	1.34 (393)	1.44 (376)	1.65 (273)

posite fit are almost constant at all phases with a slight variation in normalizations in line with the orbital motion. The occultation caused by the X-ray eclipse may cause these variations in these components. The emission line at 6.7 keV shows variations matching the behaviour of the flux over the orbit, with higher  $\sigma$  and normalisation values at orbital maximum and lower values at orbital minimum. The emission line at 6.7 keV which corresponds to Fe XXV transition is present in the model throughout the orbital motion. However, as seen in Figure 2.6, at the orbital minimum (phases 0.9 to 1.3) we also needed to include two additional emission lines at 6.9 keV (Fe XXVI transition) and 6.4 keV (fluorescent Fe line) in order successfully fit the models. The justification for including these additional lines are presented in Figure 2.7 where we fitted the continuum of the spectra of the phases around orbital minima with 4 MEKAL components. We used the 6.0-8.0 keV energy range in order to focus on the region where the lines are present. As seen from the figure, there is a clear excess around 6.4 keV. For phases from 0.4 to 0.8 which correspond to orbital maximum, 6.4 keV and 6.9 keV lines could not be freely fit. For these fits, by fixing all the other model parameters normalization upper limits were obtained.

In the 2000 data the width of the emission line at 6.7 keV has values around 0.1 keV with no prominent variations over the orbital phase. However, the same line shows variations in line with the changing flux over the orbital motion in the 2003 data. During the orbital minimum, the line widths have similar values that of the 2000 data, but the line broadens, with widths reaching up to 0.3 keV during the phases corresponding to orbital maximum. The line width of the emission from 6.4 keV changes from 0 keV to 0.16 keV.

## 2.4 Spin Phase-Resolved Spectroscopy

In addition to orbital phase resolved spectroscopy, spin phase-resolved spectroscopy was also performed for 2000 and 2003 observations. Using the method presented in Section 2.2, spin phase resolved spectra were created using the ephemeris  $T_0 = 2437699.8914(5) + 0.046546504(9)E$  given by Hellier & Sproats (1992). The analysis and fitting was carried out by using XSPEC. As in the case of orbital phase resolved spectroscopy, in order to improve the statistics of the data, the extracted spectra were

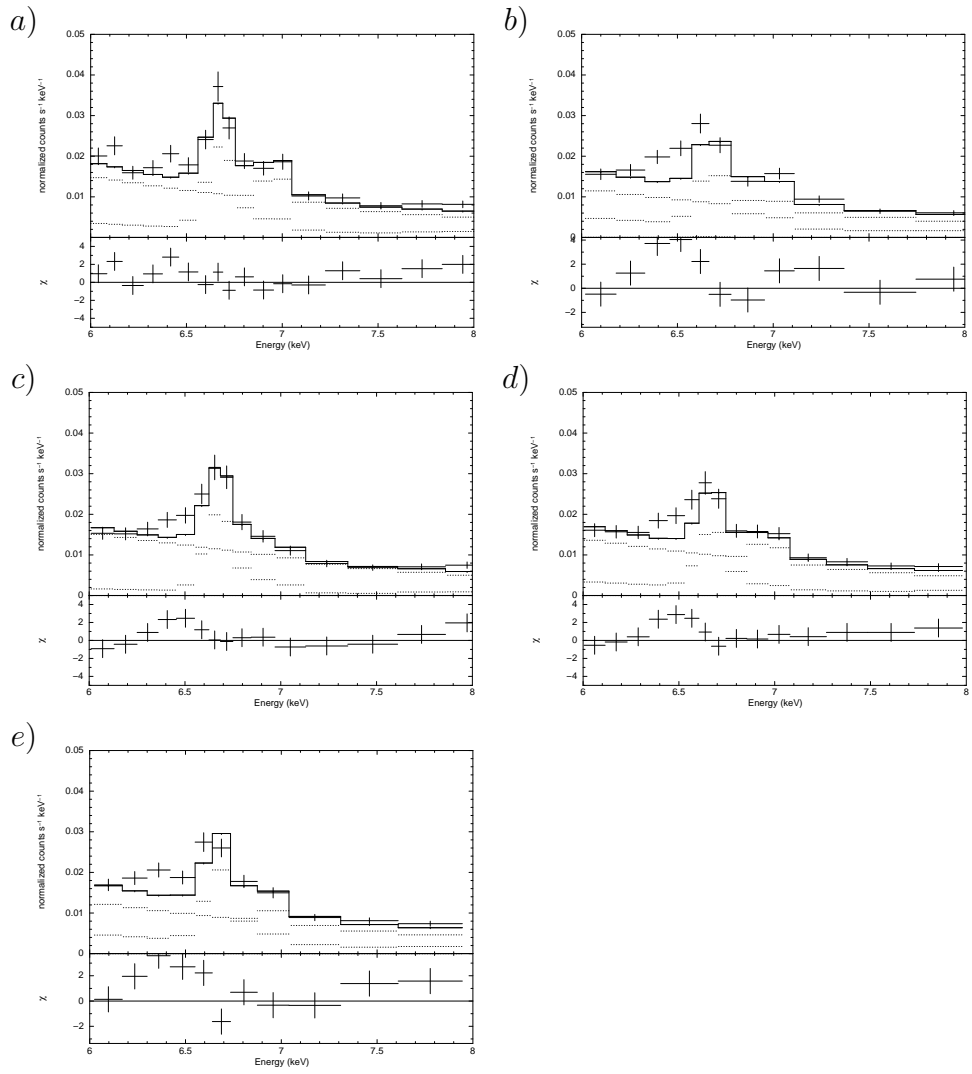


Figure 2.7: The orbital phase-resolved spectra of 2003 data between phases 0.9 to 1.3 from a) to e) respectively. The energy range is between 6 and 8 keV to focus on the emission lines.

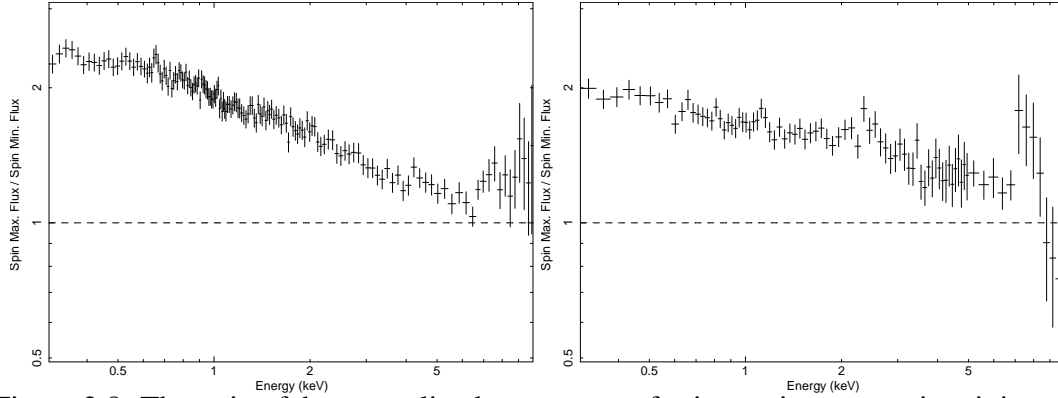


Figure 2.8: The ratio of the normalized count rates of spin maximum to spin minimum against energy. The left hand panel shows the 2000 data and the right hand panel shows the 2003 data.

grouped with minimum 100 counts in each energy bin, and only the energy channels between 0.3 keV and 10.0 keV were used.

We also plotted the ratio of spin maximum (phases between 0.75 and 0.95) spectrum to the spin minimum (phases between 0.25 and 0.45) spectrum against energy in order to study the absorption effects. As seen in Figure 2.8, the spectral ratios for both observations display a similar behavior. The ratio values start with around 2 at the low energies, and gradually drops to 1 as the energy increases.

The same composite model with small modifications were used in fitting the spin phase resolved spectra. The model consists of 2 MEKAL components at different temperatures, a VMCFLOW model, a partial covering absorber (PCFABS) and Gaussian emission line at 6.7 keV and 6.9 keV where necessary. The partial covering absorber instead of a simple absorber used in order to achieve better fits at lower energies, and inclusion of other emission lines were not necessary.

In Figure 2.9 the spectra and the corresponding fitting model for spin minima (phase 0.3) and maxima (phase 0.9) are displayed for the 2003 data. The best fit parameters and corresponding errors from the spin phase resolved spectroscopy are displayed in Table 2.5 and in Figure 2.10, a selection of spectral parameters are plotted against the spin phase. As seen from the fits, *LowT* and *HighT* parameters of the VMCFLOW model vary inversely with the spin folded light curve. Contrary to expectations, absorbing column and covering fraction of the partial covering absorber do not vary inversely with the flux. The emission line centered at 6.7 keV does not also show

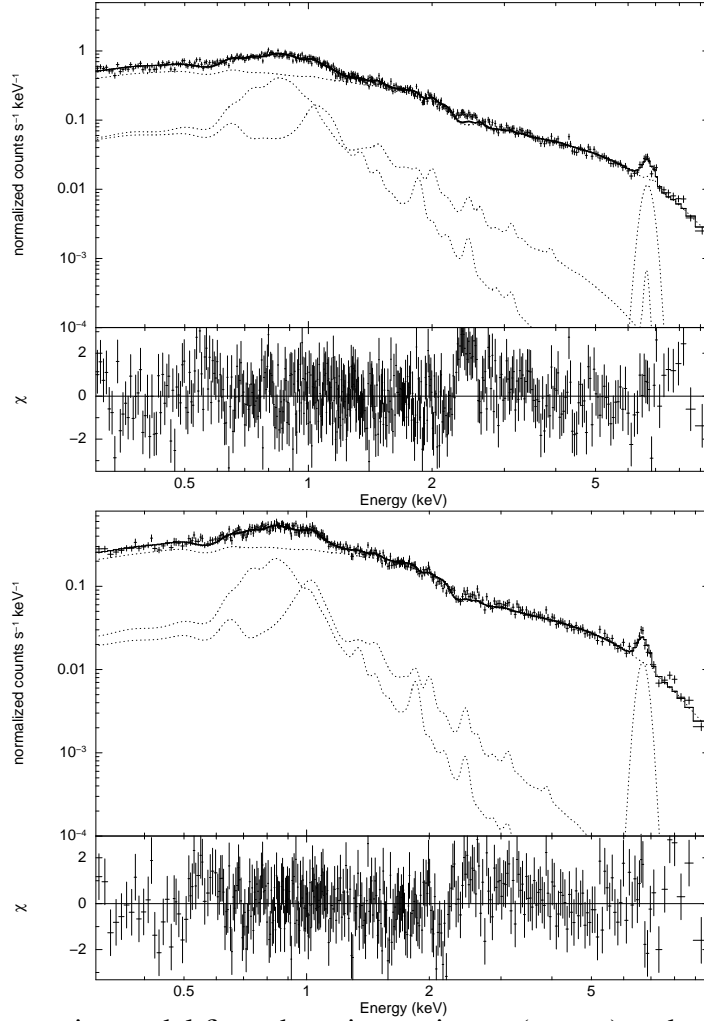


Figure 2.9: Composite model fit to the spin maximum (on top) and minimum (at the bottom) of EX Hya from 2003 data.

significant variation over the spin phase in 2003. Similar to the orbital phase resolved spectroscopy, we also checked whether additional 6.4 keV emission lines are needed in spin phase resolved spectra, however, we see no such excess and necessity to include additional emission lines.

The same model is used for fitting the spin phase resolved spectra of 2000. Figure 2.11 displays the spectra and the corresponding best fit at the spin phase maximum (phase 0.9) and minimum (phase 0.5). Table 2.6 shows the best fitting spectral parameters and Figure 2.12 shows the plot of selected spectral parameters against the spin phase. According to the fits performed on the spin phase resolved spectra of 2000 observation, the emission lines at 6.7 keV and 6.9 keV are present at all phases. As seen in Figure 2.12,  $N_{\text{H}}$ , covering fraction,  $LowT$  and  $HighT$  parameters values

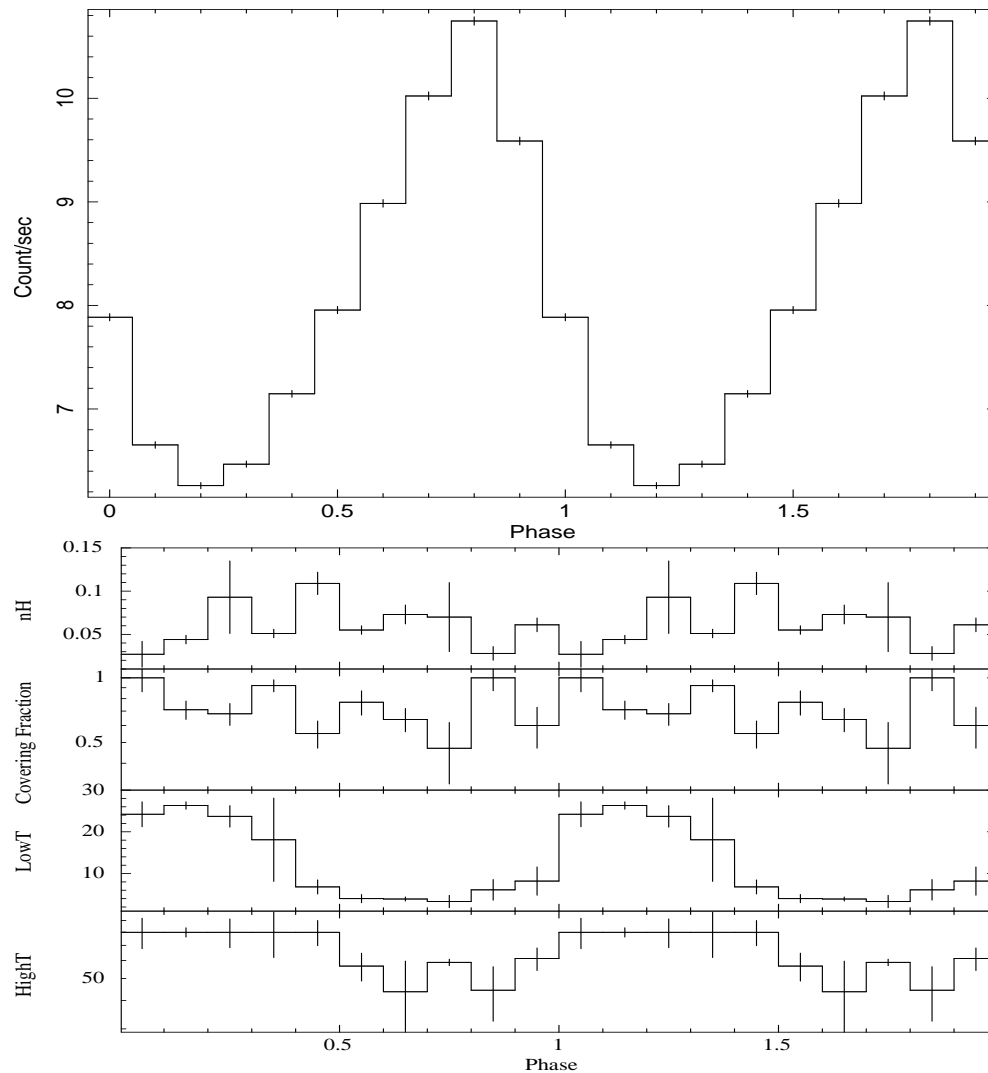


Figure 2.10: The X-ray light curve (2003 observation) folded over the spin period using the ephemeris  $T = 2437699.8914(5) + 0.046546504(9)E$  at the top, and spectral parameters derived from the best fits to the orbital phase-resolved spectra plotted over the spin phase. The temperatures are given in keV.

Table 2.5: Spectral parameters derived from the best fits to each spectra extracted from each 0.1 spin phase interval for the year 2003 observation. The corresponding parameter errors are at  $2\sigma$  confidence level.

Model	Component	0.1	0.2	0.3	0.4	0.5
pcfabs	$N_{\text{H}} (\times 10^{-22})$	$0.027^{+0.003}_{-0.029}$	$0.044^{+0.005}_{-0.006}$	$0.093^{+0.044}_{-0.039}$	$0.051^{+0.004}_{-0.006}$	$0.109^{+0.013}_{-0.014}$
	CoverFrac	$1.00^{<}_{-0.16}$	$0.71^{+0.08}_{-0.07}$	$0.68^{+0.08}_{-0.08}$	$0.92^{+0.06}_{-0.06}$	$0.55^{+0.09}_{-0.07}$
MEKAL1	kT (keV)	$0.52^{+0.1}_{-0.05}$	$0.63^{+0.02}_{-0.03}$	$0.60^{+0.03}_{-0.04}$	$0.62^{+0.03}_{-0.04}$	$0.62^{+0.02}_{-0.04}$
	Norm ( $\times 10^{-4}$ )	$1.8^{+0.5}_{-0.2}$	$2.2^{+0.2}_{-0.2}$	$1.8^{+0.2}_{-0.2}$	$1.9^{+0.2}_{-0.1}$	$3.2^{+0.8}_{-0.5}$
MEKAL2	kT (keV)	$1.10^{+0.28}_{-0.18}$	$1.4^{+0.2}_{-0.1}$	$1.29^{+0.10}_{-0.09}$	$1.58^{+0.08}_{-0.23}$	$1.46^{+0.18}_{-0.10}$
	Norm ( $\times 10^{-4}$ )	$1.9^{+0.2}_{-0.5}$	$1.7^{+0.7}_{-0.4}$	$2.2^{+0.4}_{-0.4}$	$3.3^{+0.7}_{-0.8}$	$2.8^{+0.8}_{-0.6}$
VMCFLOW	LowT (keV)	$24.1^{+0.4}_{-3.7}$	$26.4^{+0.9}_{-0.9}$	$22.7^{+0.4}_{-2.7}$	$18.1^{+13.1}_{-4.2}$	$6.9^{+2.1}_{-1.4}$
	HighT (keV)	$79.9^{<}_{-12.3}$	$79.9^{<}_{-3.8}$	$79.9^{<}_{-11.7}$	$79.9^{<}_{-18.1}$	$79.9^{<}_{-10.3}$
Gaussian1 (6.7 keV)	$\sigma$ (keV)	$0.18^{+0.7}_{-0.5}$	$0.19^{+0.06}_{-0.04}$	$0.18^{+0.04}_{-0.03}$	$0.20^{+0.04}_{-0.04}$	$0.14^{+0.07}_{-0.04}$
	Norm ( $\times 10^{-5}$ )	$3.6^{+0.8}_{-0.6}$	$3.8^{+0.8}_{-0.6}$	$4.2^{+0.7}_{-0.6}$	$4.0^{+0.6}_{-0.7}$	$2.4^{+0.3}_{-0.4}$
	$\chi^2_{\nu}$ (d.o.f.)	1.27 (333)	1.21 (312)	1.17 (329)	1.24 (338)	1.35 (360)
Model	Component	0.6	0.7	0.8	0.9	1.0
pcfabs	$N_{\text{H}} (\times 10^{-22})$	$0.055^{+0.004}_{-0.005}$	$0.073^{+0.007}_{-0.017}$	$0.069^{+0.043}_{-0.034}$	$0.028^{+0.014}_{-0.002}$	$0.061^{+0.006}_{-0.010}$
	CoverFrac	$0.77^{+0.08}_{-0.13}$	$0.64^{+0.07}_{-0.10}$	$0.48^{+0.29}_{-0.12}$	$1.0^{<}_{-0.14}$	$0.60^{+0.13}_{-0.13}$
MEKAL1	kT (keV)	$0.64^{+0.02}_{-0.02}$	$0.64^{+0.02}_{-0.02}$	$0.63^{+0.01}_{-0.01}$	$0.64^{+0.02}_{-0.02}$	$0.64^{+0.02}_{-0.03}$
	Norm ( $\times 10^{-4}$ )	$2.6^{+0.2}_{-0.2}$	$3.4^{+0.3}_{-0.2}$	$3.6^{+0.2}_{-0.2}$	$3.1^{+0.2}_{-0.2}$	$2.6^{+0.2}_{-0.1}$
MEKAL2	kT (keV)	$1.67^{+0.12}_{-0.10}$	$1.72^{+0.10}_{-0.13}$	$1.92^{+0.18}_{-0.15}$	$1.66^{+0.18}_{-0.22}$	$1.63^{+0.15}_{-0.16}$
	Norm ( $\times 10^{-4}$ )	$3.8^{+0.9}_{-0.8}$	$4.7^{+1.3}_{-1.0}$	$7.4^{+0.8}_{-0.7}$	$4.8^{+1.2}_{-1.0}$	$3.1^{+0.9}_{-0.8}$
VMCFLOW	LowT (keV)	$4.1^{+1.0}_{-1.0}$	$3.9^{+0.6}_{-0.5}$	$3.4^{+1.6}_{-1.0}$	$6.2^{+3.0}_{-1.9}$	$8.2^{+3.3}_{-3.7}$
	HighT (keV)	$56.7^{+9.0}_{-8.0}$	$43.7^{+18.5}_{-15.7}$	$59.0^{+1.8}_{-2.9}$	$46.4^{+12.7}_{-11.2}$	$61.3^{+3.2}_{-10.3}$
Gaussian1 (6.7 keV)	$\sigma$ (keV)	$0.17^{+0.07}_{-0.04}$	$0.31^{+0.08}_{-0.06}$	$0.15^{+0.09}_{-0.04}$	$0.19^{+0.04}_{-0.04}$	$0.17^{+0.05}_{-0.04}$
	Norm ( $\times 10^{-5}$ )	$3.6^{+0.08}_{-0.06}$	$3.9^{+0.8}_{-0.7}$	$3.5^{+1.0}_{-0.6}$	$4.1^{+0.7}_{-0.7}$	$3.8^{+0.7}_{-0.6}$
	$\chi^2_{\nu}$ (d.o.f.)	1.27 (374)	1.46 (396)	1.39 (416)	1.39 (416)	1.55 (382)

all peak during the orbital minima (phases 0.1-0.4) and have lower values at the remaining spin phases. This is an expected result when the spectral variations arise due to absorption. While 6.7 keV emission shows no significant modulation over the spin phase, the normalization of the 6.9 keV line has lowest values around the spin minima (phases 0.4-0.5).

In both observations the temperature parameters of MEKAL components are predominantly constant at all phases. There is only a slight modulation in normalizations in both 2000 and 2003, in line with the flux over spin phase.

## 2.5 Discussion

In this chapter, the XMM-Newton EPIC pn data EX Hya was analyzed thoroughly. The source has a complex spectrum, and in order to fit the data, a multi-component model was necessary. The average spectrum of the source was fit with a model that included 2 MEKAL models with different temperatures around 1.3-1.7 keV and 0.6-0.8 keV; a cooling flow emission with variable abundances (VMCFLOW) with temperature distribution of 3-33 keV and 8-61 keV for 2000 and 2003 observation respectively; and Gaussian emission profiles centered at various energies such as 6.4 keV, 6.7 keV, 6.9 keV, 0.58 keV, 0.78 keV and 7.8 keV. The emission line at 7.8 keV is not usually encountered in the spectra of CVs. The detailed investigations from the spectral fits focused on the 5.0-10.0 keV region, the line is found to be centered at  $7.8_{-0.3}^{+0.3}$ , with a line width of 0.2-0.4 keV and a normalization of  $0.0001 \text{ photons cm}^{-2} \text{ s}^{-1}$ . According to CHIANTI atomic database, the 7.8 keV line corresponds to Fe XXV  $K\beta$  transition, and the other emission lines centered at 0.78 and 0.58 keV correspond to O VIII and O VII transitions respectively. These lines may have emerged from the calibration issues, since they only appear in the average spectrum.

At all orbital and spin phases, the two plasma emissions modelled with MEKAL are present and they both have almost constant temperature values around 0.6-0.8 and 1.3-1.7 keV. This indicates that there is a region in the line of sight that emits X-rays and not affected by either orbital and spin motion. We find that the normalisations of the MEKAL emission components decrease during the eclipse, which indicates that these



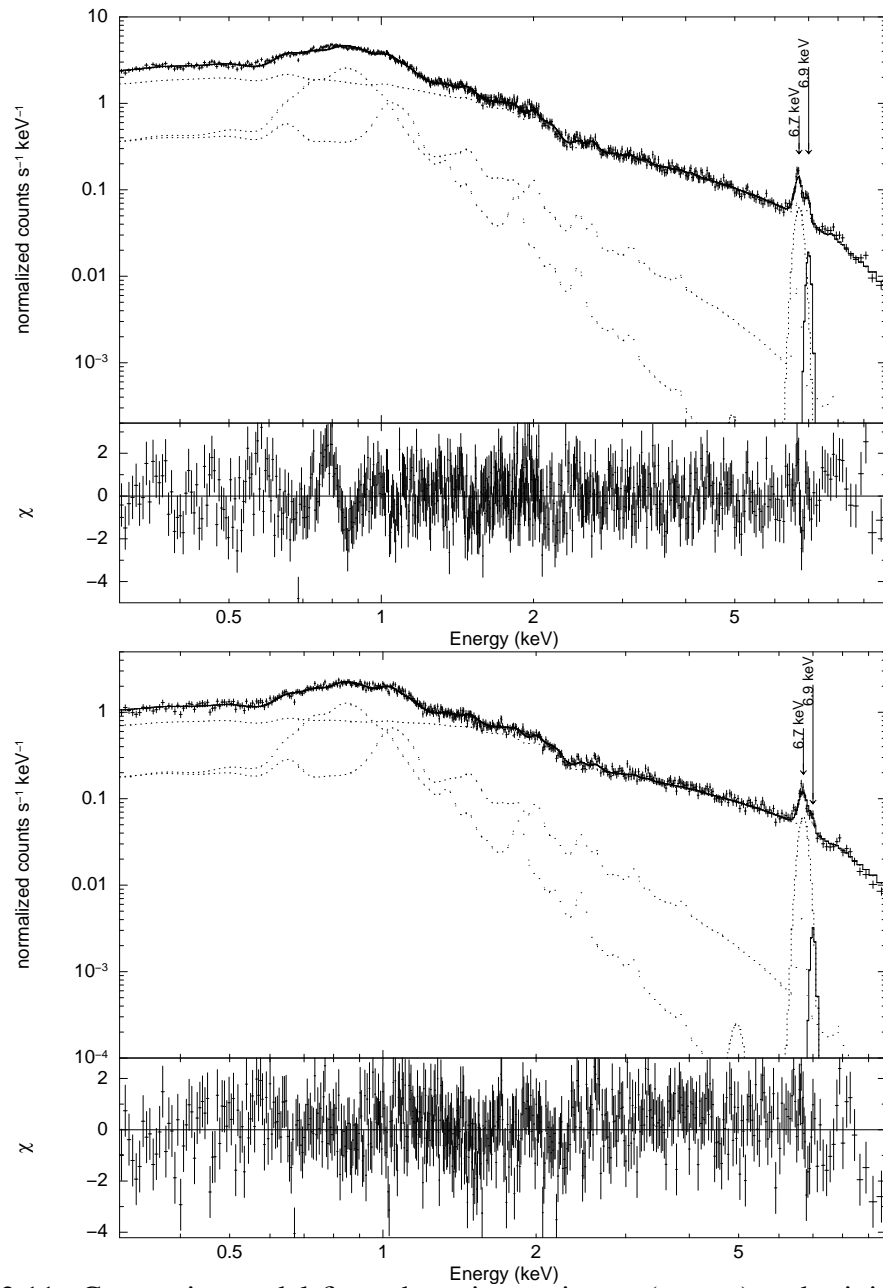


Figure 2.11: Composite model fit to the spin maximum (on top) and minimum (at the bottom) of EX Hya from 2003 data. The 6.7 keV and 6.9 keV emission lines are displayed explicitly.

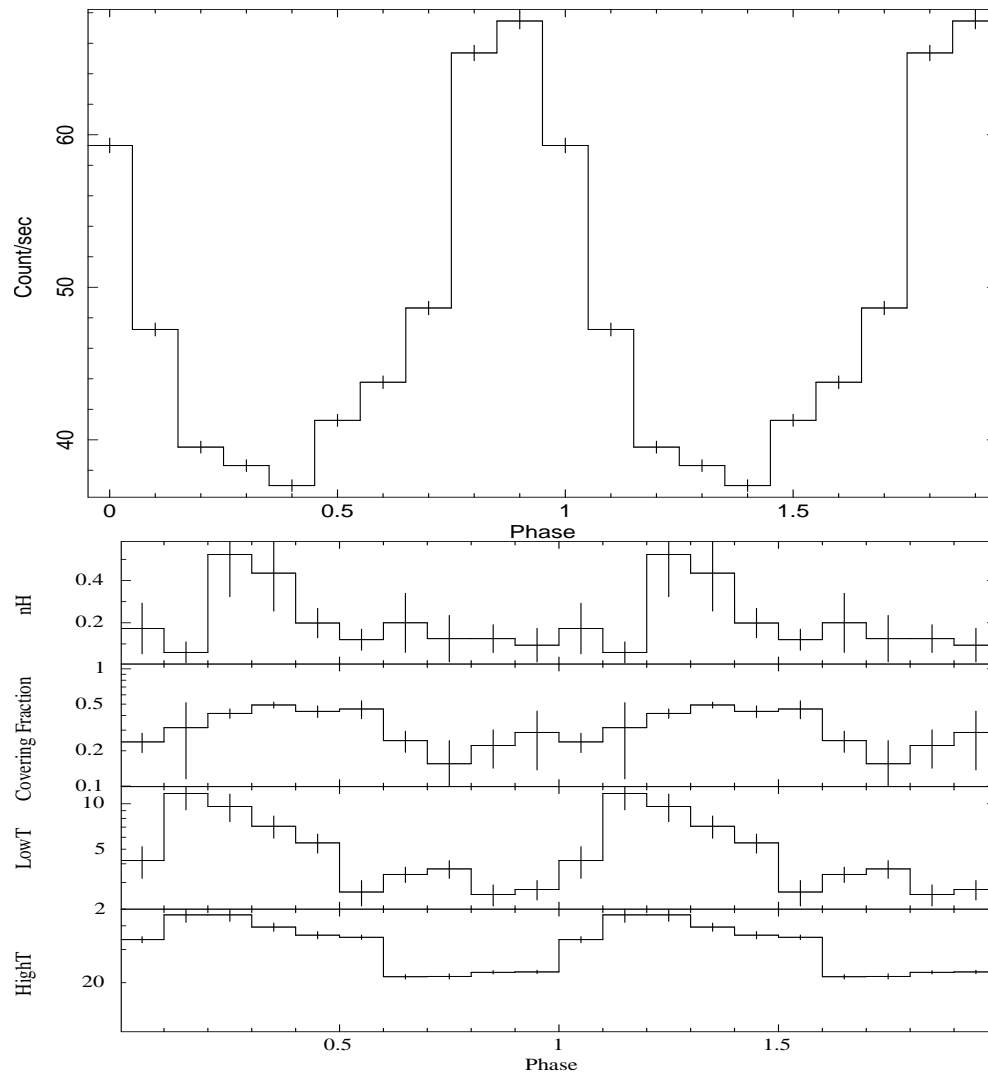


Figure 2.12: The X-ray light curve (2000 observation) folded over the spin period using the ephemeris  $T = 2437699.8914(5) + 0.046546504(9)E$  at the top, and spectral parameters derived from the best fits to the orbital phase-resolved spectra plotted over the spin phase. The temperatures are given in keV.

Table 2.6: Spectral parameters derived from the best fits to each spectra extracted from each 0.1 spin phase interval for the year 2003 observation. The corresponding parameter errors are at  $2\sigma$  confidence level.

Model	Component	0.1	0.2	0.3	0.4	0.5
pcfabs	$N_{\text{H}} (\times 10^{-22})$	$0.17^{+0.16}_{-0.09}$	$0.06^{+0.12}_{-0.04}$	$0.52^{+0.20}_{-0.25}$	$0.44^{+0.20}_{-0.17}$	$0.20^{+0.08}_{-0.07}$
	CoverFrac	$0.24^{+0.06}_{-0.03}$	$0.31^{+0.68}_{-0.17}$	$0.42^{+0.04}_{-0.04}$	$0.49^{+0.04}_{-0.02}$	$0.43^{+0.07}_{-0.03}$
MEKAL1	kT (keV)	$0.62^{+0.2}_{-0.2}$	$0.62^{+0.02}_{-0.02}$	$0.61^{+0.03}_{-0.02}$	$0.62^{+0.01}_{-0.01}$	$0.63^{+0.01}_{-0.03}$
	Norm ( $\times 10^{-4}$ )	$4.6^{+0.4}_{-0.3}$	$3.5^{+0.3}_{-0.2}$	$4.1^{+0.7}_{-0.4}$	$4.4^{+0.7}_{-0.7}$	$3.2^{+0.3}_{-0.4}$
MEKAL2	kT (keV)	$1.41^{+0.21}_{-0.07}$	$1.42^{+0.20}_{-0.07}$	$1.41^{+0.22}_{-0.08}$	$1.58^{+0.13}_{-0.16}$	$1.47^{+0.17}_{-0.13}$
	Norm ( $\times 10^{-4}$ )	$5.4^{+1.2}_{-0.6}$	$4.6^{+1.1}_{-0.5}$	$5.7^{+1.1}_{-1.2}$	$6.9^{+1.8}_{-2.4}$	$4.7^{+0.9}_{-0.8}$
VMCFLOW	LowT (keV)	$4.2^{+1.3}_{-0.6}$	$11.7^{+3.5}_{-1.9}$	$9.6^{+2.2}_{-1.5}$	$7.1^{+1.2}_{-1.2}$	$5.5^{+1.0}_{-0.6}$
	HighT	$33.8^{+1.3}_{-1.2}$	$45.7^{+5.2}_{-3.3}$	$45.7^{+3.8}_{-3.2}$	$39.4^{+1.2}_{-2.6}$	$35.7^{+2.0}_{-1.3}$
Gaussian1 (6.7 keV)	$\sigma$ (keV)	$0.11^{+0.03}_{-0.01}$	$0.12^{+0.05}_{-0.01}$	$0.10^{+0.04}_{-0.02}$	$0.12^{+0.04}_{-0.02}$	$0.12^{+0.03}_{-0.03}$
	Norm ( $\times 10^{-5}$ )	$2.8^{+0.4}_{-0.4}$	$3.2^{+0.5}_{-0.3}$	$3.2^{+0.4}_{-0.2}$	$3.0^{+0.5}_{-0.4}$	$3.1^{+0.4}_{-0.2}$
Gaussian2 (6.9 keV)	$\sigma$ (keV)	0	0	0	0	0
	Norm ( $\times 10^{-6}$ )	$5.5^{+2.1}_{-2.3}$	$3.4^{+2.1}_{-2.8}$	$4.0^{+2.0}_{-2.4}$	$0.9^{+2.2}_{-0.7}$	$0.9^{+2.0}_{-0.7}$
	$\chi^2_{\nu}$	1.27 (539)	1.26 (493)	1.28 (494)	1.28 (501)	1.23 (494)
Model	Component	0.6	0.7	0.8	0.9	1.0
pcfabs	$N_{\text{H}} (\times 10^{-22})$	$0.12^{+0.06}_{-0.04}$	$0.20^{+0.22}_{-0.11}$	$0.12^{+0.18}_{-0.08}$	$0.12^{+0.07}_{-0.07}$	$0.10^{+0.10}_{-0.06}$
	CoverFrac	$0.46^{+0.10}_{-0.6}$	$0.24^{+0.07}_{-0.03}$	$0.16^{+0.11}_{-0.04}$	$0.22^{+0.13}_{-0.04}$	$0.29^{+0.28}_{-0.07}$
MEKAL1	kT (keV)	$0.61^{+0.02}_{-0.02}$	$0.61^{+0.02}_{-0.02}$	$0.62^{+0.02}_{-0.02}$	$0.64^{+0.01}_{-0.01}$	$0.64^{+0.01}_{-0.01}$
	Norm ( $\times 10^{-4}$ )	$3.7^{+0.3}_{-0.2}$	$4.5^{+0.4}_{-0.3}$	$4.9^{+0.3}_{-0.3}$	$6.0^{+0.3}_{-0.3}$	$6.0^{+0.4}_{-0.2}$
MEKAL2	kT (keV)	$1.36^{+0.07}_{-0.08}$	$1.40^{+0.10}_{-0.06}$	$1.42^{+0.15}_{-0.06}$	$1.57^{+0.12}_{-0.16}$	$1.71^{+0.10}_{-0.12}$
	Norm ( $\times 10^{-4}$ )	$4.5^{+0.6}_{-0.6}$	$6.1^{+0.4}_{-0.6}$	$7.0^{+0.6}_{-0.6}$	$8.1^{+1.5}_{-1.5}$	$9.3^{+1.7}_{-1.6}$
VMCFLOW	LowT (keV)	$2.6^{+0.6}_{-0.5}$	$3.4^{+0.5}_{-0.4}$	$3.7^{+0.6}_{-0.4}$	$2.5^{+0.4}_{-0.4}$	$2.7^{+0.4}_{-0.4}$
	HighT (keV)	$34.8^{+1.1}_{-0.9}$	$21.5^{+0.7}_{-0.6}$	$21.6^{+0.7}_{-0.6}$	$22.7^{+0.5}_{-0.5}$	$22.8^{+0.5}_{-0.5}$
Gaussian1 (6.7 keV)	$\sigma$ (keV)	$0.10^{+0.04}_{-0.02}$	$0.10^{+0.03}_{-0.02}$	$0.11^{+0.01}_{-0.02}$	$0.10^{+0.02}_{-0.02}$	$0.11^{+0.03}_{-0.01}$
	Norm ( $\times 10^{-5}$ )	$3.1^{+0.5}_{-0.3}$	$2.7^{+0.4}_{-0.3}$	$3.2^{+0.4}_{-0.4}$	$3.2^{+0.4}_{-0.4}$	$3.0^{+0.4}_{-0.4}$
Gaussian2 (6.9 keV)	$\sigma$ (keV)	0	0	0	0	0
	Norm ( $\times 10^{-6}$ )	$4.2^{+1.9}_{-2.5}$	$4.6^{+2.0}_{-2.2}$	$5.6^{+2.2}_{-2.4}$	$5.3^{+2.1}_{-2.3}$	$5.0^{+2.4}_{-2.6}$
	$\chi^2_{\nu}$	1.31 (521)	1.39 (527)	1.22 (581)	1.10 (600)	1.24 (583)

components originate most likely from the post-shock region in the accretion column which is too complex to be represented with just a cooling-flow plasma emission model alone.

In both 2000 and 2003 observations, the light curves of the source folded over the orbital period has two prominent features. The first one is the partial X-ray eclipse which we expected to see at phase 0.0. In order to determine the exact eclipse phase, we fitted a simple sinus function to light curves folded at the orbital period for both 2000 and 2003 data. In the 2000 data, the eclipse occurs at  $0.93 \pm 0.05$  and eclipse in 2003 is at  $1.02 \pm 0.05$ . The semi amplitude variations are  $6.4 \pm 1.0$  counts  $s^{-1}$  and  $1.6 \pm 0.3$  counts  $s^{-1}$  with 14% and 20% modulations for 2000 and 2003 respectively. The errors accumulated from phase locking amounts up to 0.000083 and 0.000088 for 2000 and 2003 data respectively. From these values, it is clear that the X-ray eclipse occurs at different phase than optical observations. In the previous works (e.g. Hoogerwerf, Brickhouse & Mauche 2005), however, it is indicated that the eclipse at higher energies lag the eclipse at the lower energies. For 10-15 Å the eclipse happens at phase 0.992 while for 15-20 Å it happens at phase 1.0. Moreover Belle et al. (2002) found that the EUV eclipse occurs at phase 0.97 and suggested that the optical eclipse found at phase 0 may be originating from the eclipse of the hot spot. The shift in phase we find in the eclipse from 2000 to 2003 may be due to changes in the geometry of the eclipsing region between the two epochs. The X-ray eclipse is a partial one, so that the count rate does not disappear completely during the eclipse. This is in accordance with two pole accretion where one of the accreting regions is eclipsed but the other pole is still in the line of sight (Belle et al. 2005). This is also consistent with our findings, since the phase resolved spectroscopy shows that some of the emission components and emission lines are unaffected by the eclipse. However, we cannot reach the two pole accretion conclusion, since the light curves folded at the spin phases show a single peak profile as expected from single pole accretion.

The other distinct feature of the light curve folded over the orbital period is the shallow dip observed at both 2000 and 2003. The dip is around phases 0.45-0.65 in year 2000, with a depth of about 1/3 of the eclipse. In 2003, the dip gets shallower with 1/5 of the depth of the eclipse and the location moves to the orbital phases 0.35-0.55.

This modulation has also been observed at other wavelengths, in optical, UV and X-rays; and it is attributed to the hot spot and/or bulge on the disc (e.g. Hoogerwerf et al. 2005, Belle et al. 2005, Mhlahlo et al. 2007). At higher wavelengths, the dip becomes more prominent and it appears at phases closer to the eclipse. This is due to the variations of the ionization state of the bulge. Belle et al. (2005) found the dip around phase 0.65 with the *RXTE* light curve, Hoogerwerf et al. (2005) found the dip at phase 0.78 from *Chandra* light curve. Both of these light curves are from May 2000, so the dip feature found July 2000 XMM-Newton light curve is in agreement with the above examples.

During the eclipse, absorbing column and the lower limit of the cooling flow temperature distribution significantly increase in both 2000 and 2003 data. This implies that the absorption has a major role in the orbital modulations in X-rays over the orbital motion. Increasing absorption reduces the emission originating from the bottom end of the cooling flow, and hence the lower temperature values also increase. This effect of an absorbing region on the disc affecting the X-ray orbital modulation has been encountered in CVs before (Pekön & Balman 2008). Hence the spectral behaviour of CVs over the orbital period is an area that is worth more investigation.

The spin folded light curves of the source in both 2000 and 2003 data show similar sinusoidal behaviour. A simple sine fit performed on the spin folded light curve of 2003 reveals that the spin minimum occurs at phase  $0.26 \pm 0.03$  with semi-amplitude variation of  $14.5 \pm 1.2$  counts  $s^{-1}$  and 30% modulation. For the 2000 observation, the minimum occurs at phase  $0.36 \pm 0.06$ , with semi-amplitude variation of  $14.5 \pm 1.2$  counts  $s^{-1}$  and 30% modulation. The errors accumulated from phase locking amounts to 0.00027 and 0.00029 for 2000 and 2003 observations respectively, and are much smaller than our phase bins of 0.1. The location of the spin minimum changes from 2000 to 2003, which is most likely due to variations in the accretion column/curtain structure between these epochs.

The values of absorbing column and covering fraction parameters increase dramatically during the spin minima in 2000 data. This indicates the role of absorption from the curtains in the spin variation. The lower temperature limit of the cooling flow component also increases during the spin minima. This in turn indicates that the

spectrum gets harder due to absorbing reducing the amount of softer X-rays. In 2003, the absorbing column and covering fraction does not show a distinct variation over the spin period. However, the lower temperature limit shows a net increase during the spin minima, which is in agreement with the scenario that the X-ray modulation over the spin phase arises from the absorption from the curtains. Our findings do not rule out the effect of occultation by the white dwarf as put forward by Allan et al. (1998), but favor the fact that the absorption predominantly has more effect on spin modulation.

The 6.4 keV fluorescent emission line is a common feature observed in IPs and originates from reprocessing of the hard X-rays from the surface of the white dwarf (Hellier & Mukai 2004, Landi et al. 2009). Hellier & Mukai (2004) encountered the 6.4 keV emission line in the *Chandra HEG* spectrum of EX Hya, and found that the line to be weaker than 6.7 keV and 6.9 keV Fe lines. The average XMM-Newton spectrum of the source from 2003 observation is in agreement with this, since we find that the normalization parameter of the 6.4 keV line to be smaller than those of 6.7 keV and 6.9 keV lines. However, 6.4 keV emission line show an unusual behaviour over the orbital cycle. According to the phase-resolved spectral analysis, the line is not detected for the orbital and spin phase-resolved spectra of the 2000 data and the spin phase-resolved spectra of the 2003 data. The line is also absent from the orbital phase resolved spectra of 2003 between phases 0.4 to 0.8 which correspond to orbital maxima. However, we can detect the 6.4 keV line during the orbital minima. This implies that the reflecting component responsible for the emergence of this emission feature is not the white dwarf, but rather the bulge on the disc which is also responsible for the X-ray modulation during the eclipse. This is the first time this kind of behaviour was observed in an IP. We strongly argue that the bulge at the accretion impact zone appears at similar orbital phases to the eclipse causing this reflection feature to occur. This feature is similar to those observed in dipping Low-mass X-ray binaries (Diaz-Trigo et al. 2006), but they have significantly higher line widths (e.g.  $\sigma \sim 0.85$  keV) than observed in this source ( $\sigma \sim 0.1$  keV).

The number of IPs observed with a soft blackbody emission component which are called "soft IPs" has been increasing over the last decade (Evans & Hellier 2007, Anzolin et al. 2008, de Martino et al. 2008, Anzolin et al. 2009). Evans & Hellier (2007)

listed EX Hya as a soft IP, however their blackbody fits yielded poor results. We also tried to include a blackbody component in the composite fitting model, however the fits give reduced  $\chi^2$  values larger than 2 and hence we cannot support the claim that EX Hya is a soft IP.

The temperature distribution of the cooling flow-plasma emission component are between 3 keV and 33 keV for 2000 data and 8 keV and 61 keV for 2003 data. This result is in agreement with the high plasma temperatures found in other IPs (Anzolin et al. 2008, de Martino et al. 2008, Anzolin et al. 2009). It should be noted that the EX Hya is one of the hardest IPs that is observed (see Brunschweiler et al. 2009). The previous works on EX Hya indicate that different observations yield different temperature distributions. *SWIFT* observation yields 19.4 keV (Brunschweiler et al. 2009), *ASCA* data yields 0.54-15.4 keV (Allan et al. 1998), and *Chandra* data yields  $< 20$  keV (Mukai et al. 2003) by fitting plasma models to the X-ray spectra. Using measurements of broad emission components, Luna et al. (2010) found pre-shock temperature values extending up to  $\sim 80$  keV from *Chandra HETG* data.

The plots of the count rate ratios of spin and orbital maximum to minimum provide information on the characteristics of absorption in the system. The spin ratios are similar in both 2000 and 2003 data, where it start around 2 at lower energies, and gradually decreases to 1 at harder energies. This may imply that the absorption from the accretion curtain has similar nature in 2000 and 2003. Spectral fitting however, indicates that the absorbing column density has been reduced by a factor of 4 from 2000 to 2003. So this indicates that the absorption due to accretion curtain has decreased in 2003. There is a significant difference between the hardness ratios of 2000 and 2003 data. Although the ratios decrease at harder energies, the decay is flatter in 2000 and 2003 data shows a much steeper decay.

Therefore, when the absorption over the orbital cycle is taken into consideration, there is clearly a difference in the state of the source between 2000 and 2003. This difference most likely arises from the changes in the absorbing material on the accretion disc/binary plane in terms of geometry and/or ionization structure.

Additionally, we also looked for any quasiperiodic oscillations (QPOs) in the source. QPOs are associated with non radial oscillations from discs at high accretion rate

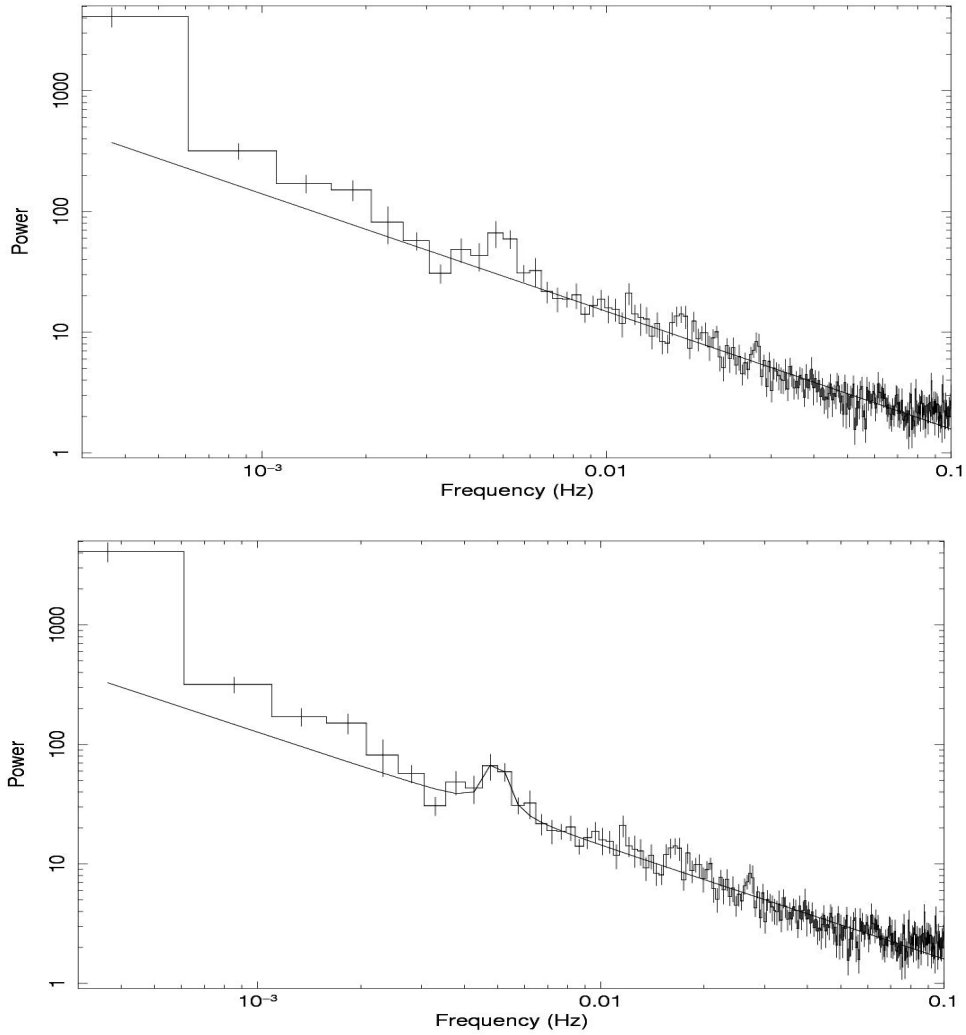


Figure 2.13: The power spectrum of EX Hya from the 2000 data. The top panel shows a power law fit only. The bottom panel shows a Lorentzian superimposed on the powerlaw continuum.

(Warner & Woudt 2002). For EX Hya, Semena et al. (2014) searched for a QPO in the optical data, however, they fail to detect any. For both 2000 and 2003 data, we extracted light curves binned with 0.1 s, and plotted power spectra in search for QPOs. We could only find a period in the 2000 data, that might be a QPO. We fitted the power spectrum with a power law and a Lorentzian, and we could detect a period at 200.9 s, at  $2.5 \sigma$  level. Figure 2.13 shows the power spectrum and the period found.



## CHAPTER 3

### FO AQR

FO Aqr is a well known intermediate polar (IP), which has an orbital period of 4.85 hr (Osborne & Mukai 1989) and a white dwarf spin period of 20.9 min (Patterson et al. 1998). The source has been observed over a variety of X-ray missions; *EXOSAT*, *Ginga*, *ASCA*, *RXTE*, *XMM-Newton*, *INTEGRAL*, *SWIFT* and *Suzaku* (Cook, Watson & McHardy 1984, Norton et al. 1992; Mukai, Ishida & Osborne 1994; Evans et al. 2004, Parker, Norton & Mukai 2005, Landi et al. 2009, Yuasa et al. 2010, respectively). There has been a debate going on over the years as to how the accretion takes place in the system: First, it has been suggested that the system accretes without a disc and the accretion flow alternates between the magnetic poles of the white dwarf (Norton et al. (1992)). However, later, it has been argued that an accretion disc in the system in fact exists and the accretion takes place simultaneously through an accretion disc and an accretion stream flowing above the disc Hellier (1993). Mukai, Ishida & Osborne (1994) confirmed this mode of hybrid accretion, but stated that the dominant accretion occurs via a partial accretion disc. Later, it was suggested that, over the years, the system underwent alternating accretion modes, changing from a hybrid mode of disc-fed and stream fed accretion to disc fed mode i.e. hybrid mode in 1988, disc-fed mode in 1990 (Norton, Beardmore & Taylor 1996) hybrid mode in 1993 and 1998 (Beardmore et al. 1998), disc-fed mode in 2001 (Evans et al. 2004). Changes in the mass accretion rate of the system are the most probable cause of these changes in modes of accretion (de Martino et al. 1999). Orbital modulations have been observed in the system, which tend to be deeper at lower energies, arising due to absorption from the accretion stream and vertical structures on the disc (Hellier et al. 1993; Evans et al. 2004; Parker, Norton & Mukai 2005). The system has a

complicated spin pulse shape: It has a quasi-sinusoidal component and a notch after a "dip" which caused by the absorption from accretion curtains (Evans et al. 2004). Over the orbital phase, the pulse profile remains the same (Hellier 1993), however, between observations at different epochs it may vary between nearly sinusoidal shape to saw-tooth shapes (Beardmore et al. 1998).

The average X-ray spectrum of the source have been represented with a plasma emission with multiple components, complex absorption and Gaussian lines (eg. Mukai, Ishida & Osborne 1994; Evans et al. 2004; Yuasa et al. 2010). An soft blackbody component was not detected by using *XMM-Newton* data Evans & Hellier (2007) or by using *Suzaku* data Yuasa et al. (2010), however by using *INTEGRAL/IBIS* and *SWIFT/XRT* data, a blackbody component was detected at a temperature of 61 eV. This blackbody component was thought to be arising due to the irradiation of the white dwarf surface by the hard emission from accretion curtain, and it was detected by analysis of broad-band spectrum (in 0.4-50 keV band)(Landi et al. 2009).

### 3.1 Observation and Data

The *XMM-Newton* (Jansen et al. 2001) observation of FO Aqr was done on 12 May 2001 with 35 ks exposure time (OBS ID: 0009650201). It was observed with all of the instruments on board: a pn (Strüder et al. 2001) and two MOS CCD detectors (Turner et al. 2001) at the focus of three European Photon Imaging Cameras (EPIC) and are sensitive in the energy range of 0.2-15 keV; two high resolution spectrometers called Reflecting Grating Spectrometers (RGS; den Herder et al. 2001), and an optical/UV camera which is called the Optical Monitor (OM) (Mason et al. 2001).

In this analysis, EPIC pn data of the source is used since it has a higher sensitivity than MOS detectors. The archival EPIC pn data utilized, was taken with small window mode, and in the 0.3-10.0 keV energy range, it has a net count rate of  $2.33 \pm 0.01$   $\text{c s}^{-1}$ . Using version 11.0.0. of *XMM-Newton* Science Analysis Software (SAS), the standard data pipeline for preparation and processing were performed. We utilized SAS tools ESPECGET and EVSELECT respectively in order to extract a background subtracted spectra and lightcurve of the source. Single and double pixel events were

used in extraction. For the source and background photon extraction, a circular region which has a radius of 32.4 arcsec was used. We utilized the PHASECALC tool in SAS in order to create phase columns in the event files, so that spectrum and light curve extraction according to the orbital phase can be performed. The observation start time was used as the starting point of the phase column (i.e. phase 0). Using the phase column, phase-resolved spectra and lightcurves could be extracted. After extraction, data analysis was carried out with X-ray data analysis packages XRONOS 5.2 and XSPEC 12.6.0. Our analysis here is based on the original study by Evans et al. (2004) and we published our study presented in this chapter Pekön & Balman (2012).

### 3.2 Spin Modulation Variations over the Orbit

By utilizing LCMATH tool in FTOOLS v6.10 we extracted a background subtracted source lightcurve of the source. Barycentric correction was also applied to this lightcurve. Then, by using the periods given by (Patterson et al. 1998), we created spin (1254 s) and orbital (17458 s) folded lightcurves. For the orbital period we used the epochs  $T_0=2452041.806$  (HJD) and for the spin period we used the epoch  $T_0=2452041.858$  (HJD) as used by Evans et al. (2004). The orbital and spin folded lightcurves can be seen in Figure 3.1.

For the purpose of investigating the variations in spin pulse shape over the orbital phase, light curves from each 0.1 phase interval over the orbital period were extracted then folded these over the spin period. Each orbital-phase bin consists of 1745.8 s, greater than spin period, so that at least one pulse is contained in a bin. Generally, all the spin pulse shapes are similarly sinusoidal and each has minimum flux at around phase 0.8. However, it can be seen in Figure 3.2 that amplitudes of the sinusoidal spin pulses vary for each orbital phase. We also made a comparison of the orbital phase resolved spin pulse amplitude changes with the orbital folded light curve. As seen in Figure 3.3, the semi-amplitude variations are directly correlated with orbital phase flux. In order to construct Figure 3.3, spin pulse in each orbital bin was fitted with a simple sine curve, and percentage variations of semi-amplitudes of the sine fit was plotted against the orbital phase. The semi-amplitude variations change from  $(13.3\pm 3.7)\%$  at the orbital minimum to  $(38.0\pm 1.8)\%$  at the orbital maximum.

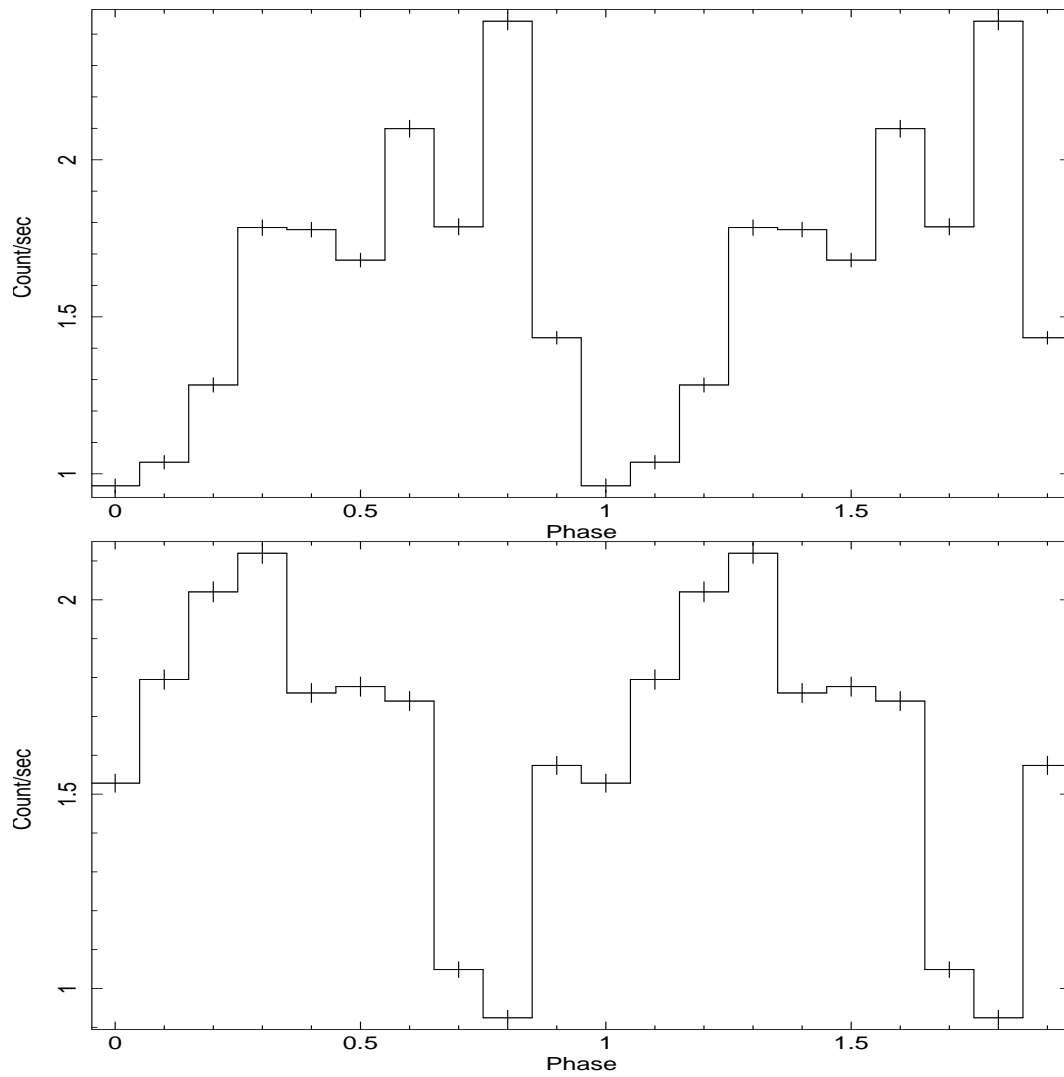


Figure 3.1: The top panel displays the X-ray light curve of FO Aqr folded over the orbital period of 17458 s, bottom panel displays the same lightcurve folded over the spin period of 1254 s.

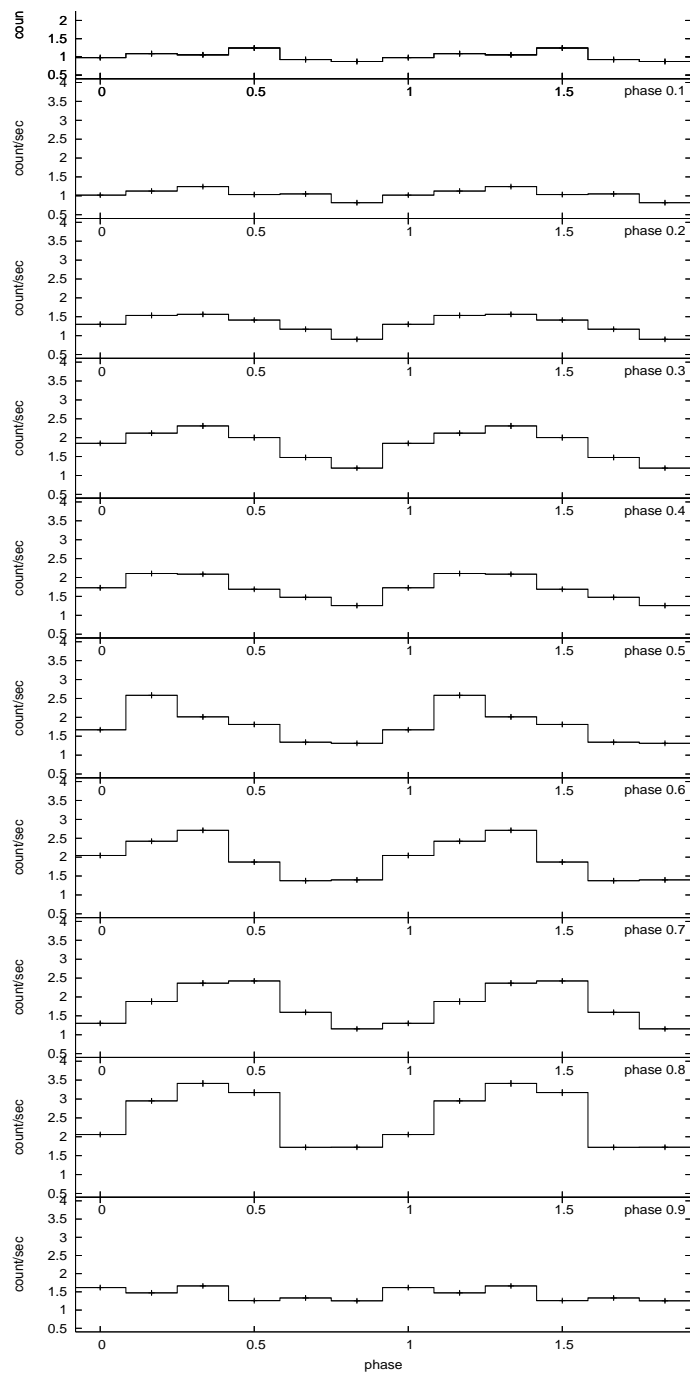


Figure 3.2: The spin pulse profile of FO Aqr for each 0.1 orbital phase interval. The corresponding phases are noted on each panel.

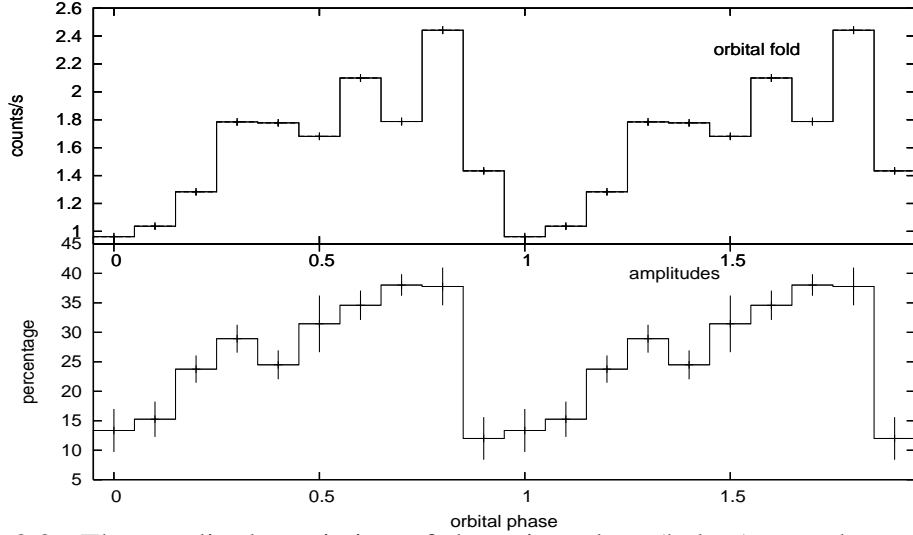


Figure 3.3: The amplitude variation of the spin pulses (below), together with the orbital flux variation (above).

### 3.3 Spectral Variations over the Orbital Phase

We began the spectral analysis by fitting the composite spectral model introduced in Evans et al. (2004) to the phase average spectrum. The composite model has various components such as a cold absorption column (WABS), two partial covering absorption columns (PCFABS); plasma emission models at three different temperatures (MEKAL) and an emission line (Gaussian) at 6.4 keV (Fe  $K_{\alpha}$ ). The

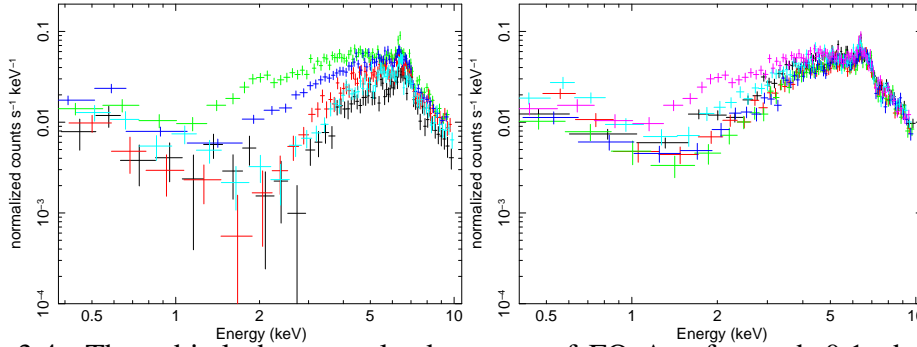


Figure 3.4: The orbital-phase resolved spectra of FO Aqr for each 0.1 phase bin interval. The left-hand panel shows phases from 0.8 to 1.2, and the right-hand panel shows the phases from 0.3 to 0.8. Notice the spectral differences on the left-hand side during orbital minima and how the spectra are different for the rest of the phases. Figure taken from Pekön & Balman (2012)

For the purpose of investigating how this composite model spectrum changes over the orbital phase, orbital phase-resolved spectroscopy was performed, and spectra for

each each 0.1 orbital phase interval (10 different spectra on the total) were extracted, fitted with the aforementioned composite model (See Pekön & Balman 2012). From this phase resolved analysis, a clear correlation of the spectral components with the orbital phase flux was observed. One of the three components of the plasma emission showed spectral hardening during the orbital minima; and one of the absorption components showed significant increase in the absorption column during the orbital minima. These findings indicate the presence of absorption from the structures on the disc.

There are also significant variations in the shape of the spectrum over the orbital phase. During the orbital phases with minimum X-ray flux (i.e. phases that are around 0-0.1) the normalized count rates around the 1-2 keV energy region drop substantially (see Figure 3.4), while on the other hand, normalized count rates below 1 keV energy region and at high energy region towards 10 keV the normalized count rates are consistent with the rest of the phases. Hence there is a clear soft excess which may be an indication of a possible warm absorber at the dipping phases in the line of sight. For the purpose of investigating this feature, two spectra were extracted from the orbital minimum (phases between 0.55-0.85) and orbital maximum (phases between 0.9-1.2). The same model that is used previously was fitted to both spectra, but this time one of the partial covering absorbers was replaced with a warm absorber model i.e. WARMABS model implemented into XSPEC. WARMABS models the absorption from a photoionized plasma in the line of sight with column densities of ions (including small cross sections) coupled through a photoionization model using stored level populations calculated by XSTAR (Kallman & Bautista 2001) assuming a given continuum spectrum.

This new composite model with warm absorber component yielded reduced  $\chi^2_\nu$  values smaller than 2. Fitting the orbital minimum spectrum yielded results with  $\chi^2_\nu$  of 1.39 (for 126 degrees of freedom) with values of  $N_H = 13.8^{+5.1}_{-4.4} \times 10^{22} \text{ cm}^{-2}$  and  $\log(\xi) = 2.36^{+0.11}_{-0.12} \text{ erg cm s}^{-1}$ . Here  $N_H$  is the equivalent Hydrogen column density of ionized absorption and  $\xi = L/n_e r^2$  is the ionization parameter where L is the luminosity of the ionizing source,  $n_e$  the electron density of the plasma and r the distance between the absorber and the ionizing source. The spectrum at the orbital minimum and the fitted model is presented in Figure 3.5, and the spectral parameters derived from the

fits are presented in Table 3.1.

Table 3.1: Spectral parameters derived from fitting the composite model to the spectra at the orbital maxima and minima. The gaussian emission line energy is fixed at 6.4 keV.  $N_{\text{H}}$  of the WARMABS model is the equivalent Hydrogen column density of ionized warm absorption. The corresponding errors are given in 99% confidence level.

Model	Component	Maxima	Minima
warmabs	$N_{\text{H}} (\times 10^{22} \text{ cm}^{-2})$	$0.56^{+0.26}_{-0.15}$	$2.09^{+0.98}_{-1.09}$
	$\log(\xi)$	$< 0.30$	$0.23^{+0.37}_{-0.26}$
	vturb ( $\text{km s}^{-1}$ )	$295^{+295}_{-295}$	$193^{+108}_{-193}$
wabs	$N_{\text{H}} (\times 10^{22} \text{ cm}^{-2})$	$0.25^{+0.12}_{-0.08}$	$0.25^{+0.26}_{-0.24}$
pcfabs	$N_{\text{H}} (\times 10^{22} \text{ cm}^{-2})$	$10.9^{+1.2}_{-1.0}$	$20.7^{+1.9}_{-1.8}$
	CoverFrac	$0.88^{+0.02}_{-0.02}$	$0.98^{+0.01}_{-0.01}$
MEKAL1	kT	$0.081^{+0.038}_{-0.081}$	$0.19^{+0.11}_{-0.08}$
	Norm	$0.058^{+0.121}_{-0.051}$	$0.18^{+4.54}_{-0.13}$
MEKAL2	kT	$61.1 <$	$49.5 <$
	Norm	$0.014^{+0.001}_{-0.001}$	$0.012^{+0.01}_{-0.01}$
Gaussian	$\sigma$	$0.23^{+0.06}_{-0.05}$	$0.16^{+0.12}_{-0.06}$
	Norm ( $\times 10^{-5}$ )	$8.4^{+1.7}_{-1.6}$	$5.0^{+2.0}_{-1.8}$
$\chi^2_{\nu}$ (d.o.f.)		1.24 (216)	1.39 (126)

### 3.4 Discussion

In non-magnetic CVs and intermediate polars, the orbital modulation is an essential source of information about the accretion disc structure. However, the task of orbital-phase resolved analysis is quite demanding since it requires additional conditions such as sufficient count rates, adequate observation times and suitable orbital and spin periods. Previous works that utilized orbital phase resolved analysis (e.g., Hellier et al. 1996, Salinas & Sclegel 2004, Itoh et al. 2006, Staude et al, 2008, Pekön & Balman 2011, Pekön & Balman 2012) are good indicators that the X-ray spectral characteristics of CVs such as absorbing column densities, temperature distribution of the X-ray emitting plasma, emission line features can be thoroughly investigated in detail over the orbital cycle. This in turn greatly enhances the understanding of the accretion mechanism in these systems in detail. Orbital phase resolved spectroscopy utilized in this work helped us to calculate contribution to the absorption from the disc and from the accretion curtains separately. The low  $P_{\text{spin}}$  to  $P_{\text{orbital}}$  ratio of the system



also proved to be an advantage, because the contribution from the spin modulations could be averaged out in each orbital phase bin.

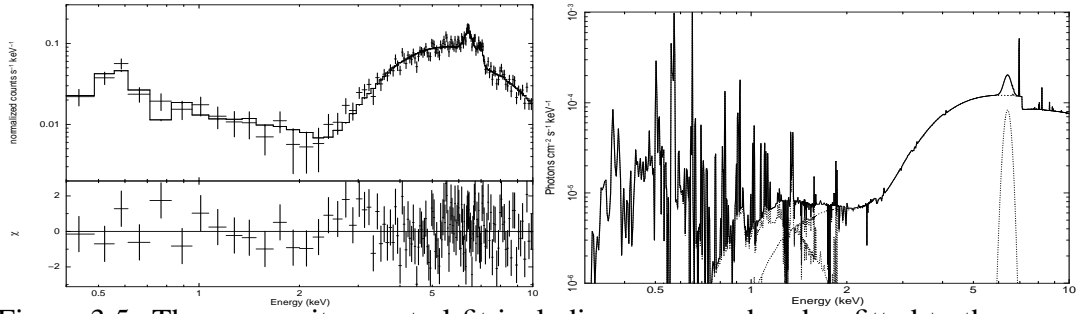


Figure 3.5: The composite spectral fit including a warm absorber fitted to the spectrum at orbital minima of the source (phases between 0.9 and 1.2) is shown on the left. On the right, a plot of the composite model alone without the data is presented.

It was pointed out by Evans et al. (2004) that "the orbital modulation of FO Aqr may be a result of the absorption from vertical structures on the disk extending out to  $140^\circ$  on the plane of the accretion disk and  $25^\circ$  above the accretion plane" (however not explicitly calculated). Moreover; Parker, Norton & Mukai (2005) showed that "the modulation depth increases at lower energies which supports the absorption effects from the disk". There are three distinct features observed in the light curve folded over the orbital period : during phases 0.3-0.6, there is a "plateau feature" where the flux is almost constant/slightly increasing; during phases 0.6-0.8 there is a peak in the flux; and around phases 0.0-0.1 there is a rapid decline and a dipping feature where the flux minimizes. As seen from the orbital phase resolved spectral analysis,  $N_{\text{H}}$  parameter of the second partial covering absorber (PCFABS2) varies inversely with these features. It shows a peak at the orbital dipping phases and the values decrease at the orbital phases where the flux peaks. The absorption column density ( $N_{\text{H}}$  parameter) has a value of  $17.45 \times 10^{22} \text{ cm}^{-2}$  during the orbital phase minima which is 5 times the value of  $3.75 \times 10^{22} \text{ cm}^{-2}$  during the orbital maxima. There is no significant modulation in the covering fraction over the orbital cycle with values close to 1 (See Pekön & Balman 2012). Hence, at all phases, the absorber is in the line of sight, with uniform structure. The material causing absorption is well smeared out on the disk because the absorbing column never disappears over the orbital cycle. However, the absorber is denser and colder during the phases of X-ray dip and causes more absorption than the orbital maxima (See Figure 3.6).

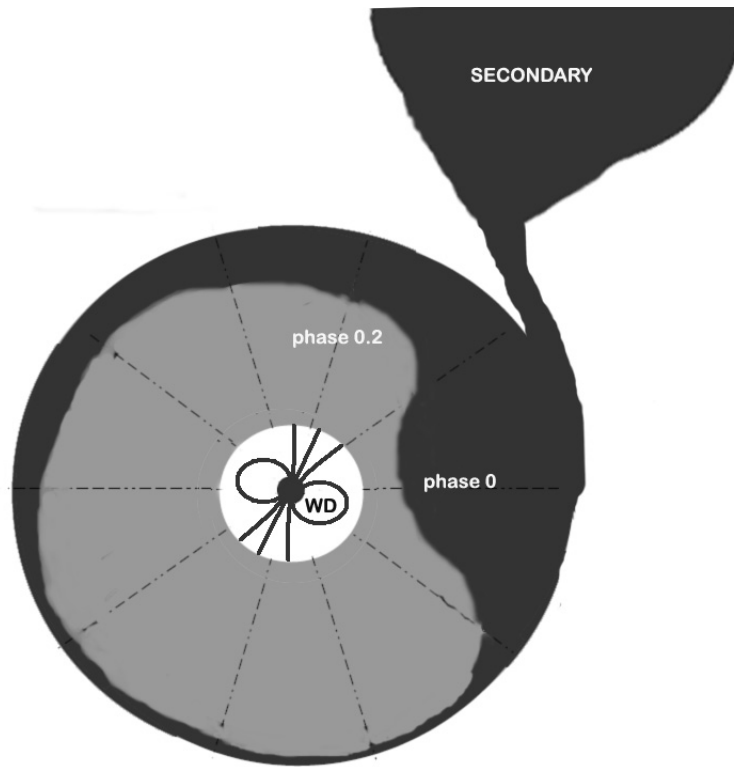


Figure 3.6: The schematic diagram showing the system. The absorber (represented as the dark region on the disc) is concentrated around the accretion impact zone (phase 0), and smeared out gradually around the accretion disk.

It has been suggested that the inferior conjunction of the secondary is the cause of the eclipse in the system (Osborne & Mukai 1989). It is also claimed that there is a reprocessing region which corresponds to the zone where accretion stream interacts with the accretion disc, and this region precedes the optical eclipse by 0.2 orbital phases. When the X-ray light curve of the source folded over the orbital period is phase-locked with the ephemeris provided by Osborne & Mukai (1989) ( $T_0 = \text{HJD } 2446081.3037 + 0.20205956E$  corresponding to the optical eclipse), the X-ray minimum coincides on phase 0.8. In this work, the folded light curve was phase-locked to the ephemeris provided Evans et al. (2004) where phase 0 corresponds to the UV minimum, and this in turn corresponds to phase 0.8 in the optical folded light curve.

The spectral fits with the composite model reveal that there is three separate absorption components in the system. The detailed phase resolved spectroscopy enables us to identify these three distinct components originating from interstellar absorption,

absorption from the accretion disc and the absorption from accretion curtains separately. The analysis of the spin pulse profile of the system over the orbital cycle is also in accordance with these findings. Although the spin pulse remains to have the same sinusoidal shape throughout the orbital cycle, the amplitude of the pulse changes in line with the flux. Hence the spin and orbital modulations originate from different sources. The spin variations are caused by the absorption from the accretion curtains and the orbital variations arise from the absorption from a region near the accretion stream impact zone on the disc.

Hellier et al. (1993) and Parker, Norton & Mukai (2005) argued that "the orbital modulation in IPs may be similar to those of Low Mass X-ray Binaries (LMXBs) where non-symmetric structures on the accretion disk raised by the impact stream (possibly around the hot spot) causing energy dependent absorption hence reducing the X-ray flux". In particular a class of LMXBs called Low-mass X-ray binary dippers show considerable fluctuations and modulation around the orbital minimum. Such characteristics have been explained by modeling the dip and non-dip spectra using highly ionized warm absorber models (Boirin et al. 2005, Diaz-Trigo et al. 2006, Balman 2009 and the references therein). We tried to explore the warm absorber scenario for FO Aqr extracting spectra from phases around the orbital minima and maxima and fit them with the assumed composite spectral model including a warm absorber. We simply replaced the absorption component due to the disk (PCFABS2) and one of the MEKAL components with WARMABS model. Both minima and the maxima could successfully be modeled with an ionized absorber. The ionized absorption  $N_{\text{warmabs}}$  value increases by 4 times during the orbital minima which is expected since the absorber is denser and colder at the orbital "dip". The values for the ionization parameter  $\log(\xi)$  is consistent within error margins between the minima and the maxima. This may be affected from the fact that we used a range of 0.3 phases for the minimum and maximum calculations. The  $N_{\text{warmabs}}$  values we find are lower than those found in LMXBs by about 10 times at all times (min or max) (see Diaz-Trigo et al. 2006). Since  $\xi$  is given by  $L/(n_e r^2)$ ,  $\xi$  values can be compared using  $\xi = L/N_H R_d$  where  $n_e \sim N_H/R_d$  ( $R_d$ , disk radius and  $N_H$  equivalent Hydrogen column density of ionized absorption). The 0.6-10 keV luminosities of LMXB dippers listed by Diaz-Trigo et al. (2006) are of the order of  $10^{36}$  erg s<sup>-1</sup>. The X-ray flux of FO Aqr in 0.6-10 keV range

is  $1.4 \times 10^{-10} \text{ ergs cm}^{-2} \text{ s}^{-1}$ , yielding a luminosity of the order of  $10^{32} \text{ erg s}^{-1}$  at 400 pc source distance. Therefore, one can approximate  $\log(\xi_{CV}) \sim -3 \log(\xi_{\text{LMXB}})$  (given the warmabs absorption column is a factor of 10 more in LMXB dippers). We also assumed similar  $P_{orb}$  and  $R_d$ , disk radius. This yields a range of  $\log(\xi_{CV}) \sim -0.8-1$ . Therefore the orbital dip in the X-ray light curve of FO Aqr is analogous to the dips observed in the dipping LMXBs with the expected cause of the dips being variation of temperature and density of the warm ionized material on the disk. A schematic representation of the system is shown in Figure 3.6.

## CHAPTER 4

### PQ GEM AND V2069 CYG

In this chapter, orbital phase resolved analysis of two IPs, PQ Gem and V2069 Cyg will be presented. As stated previously, an increasing number of IPs exhibit a soft blackbody component (30-100 eV) in their X-ray spectra. These two sources also possess this soft blackbody component arising from the reprocessing of the hard X-rays from the post-shock area in the white dwarf surface.

PQ Gem was discovered in 1992 by ROSAT all sky survey and identified as an intermediate polar by Mason et al. (1992). It is the first IP that is found to have a soft blackbody component with a temperature in the 23-58 eV range (Duck et al. 1994). The source shows strongest X-ray modulation over the white dwarf spin period of 13.89 min. It has a complex energy dependent spin pulse shape with dip followed by a plateau and then a peak. The spin modulation is explained by a combination of both the absorption from the accretion curtains and the occultation of the X-ray emitting region by the white dwarf limb (James et al. 2002, Evans et al. 2006, de Martino et al. 2004, Kiziloglu et al. 1998). The source also shows polarized optical emission varying on the spin phase and a spin down rate of  $\dot{P} = 1.1 \times 10^{-10} \text{ s}^{-1}$  indicating that it has a strong magnetic field and extended accretion from the co-rotation radius (Mason 1997). PQ Gem has an orbital period of 5.1926 hr, and it shows an "S-wave" modulation in the doppler shifts from the  $H_{\beta}$  emission lines over the orbital period. However, it shows very weak X-ray modulation over the orbital period due to low ( $<30^{\circ}$ ) inclination of the system. (Hellier 1997; Parker, Norton, Mukai 2005)

V2069 Cyg is another IP which was discovered in X-rays by Motch et al. (1996). With an orbital period of 7.48 hr (Thorstensen & Taylor 2001) and spin period of

743 s (de Martino et al. 2009), the source is quite asynchronous with  $P_{spin} / P_{orb} = 0.027$  which is much less than the common ratio of 0.1 seen in most IPs (Scaringi et al. 2010). The source shows a double peak spin modulation, as an indication of weak magnetic field strength together with the short spin period. The source shows complex absorption, a hard plasma emission, a soft blackbody component and 6.4 keV reflection component. (Bernardini et al. 2012).

#### 4.1 The Data and Observations

Both PQ Gem and V2069 Cyg were observed with *XMM-Newton* with all instruments on board in May 2001 and April 2009 respectively. PQ Gem was observed in small window mode with about 36 ks exposure time (OBS ID:0009650201) while V2069 Cyg was observed at the full frame mode with about 28 ks exposure time (0601270101).

EPIC pn data for both of the sources is used in this study with average net count rate of  $7.3 \pm 0.01 \text{ c s}^{-1}$  for PQ Gem and  $1.4 \pm 0.01 \text{ c s}^{-1}$  for V2069 Cyg. Due to lower sensitivity, MOS1 and MOS2 were not used. The standard pipeline for data preparation and processing was carried out by using version 11.0.0. of *XMM-Newton* Science Analysis Software (SAS). SAS tools ESPECGET and EVSELECT were utilized in order to extract background subtracted spectra and lightcurves of the sources. Single and double pixel events were used in extraction. For each source, a circular region centered at the source and from a background region with 28 arcsec radius for PQ Gem and 50 arcsec radius for V2069 Cyg in order to extract photons from the source and background. Before extraction, high background flaring events were filtered out by using GTIs for both sources. The PHASECALC tool in SAS was utilized for creating phase columns in the event files, in order to extract spectra and light curves according to the orbital phases. The observation start time was used as phase 0 for each spectrum, however the phases were shifted in order to lock the sources with the orbital ephemeris given by previous studies. After extraction of lightcurves and spectra, data analysis was carried out with X-ray data analysis packages XRONOS 5.2 and XSPEC 12.6.0.

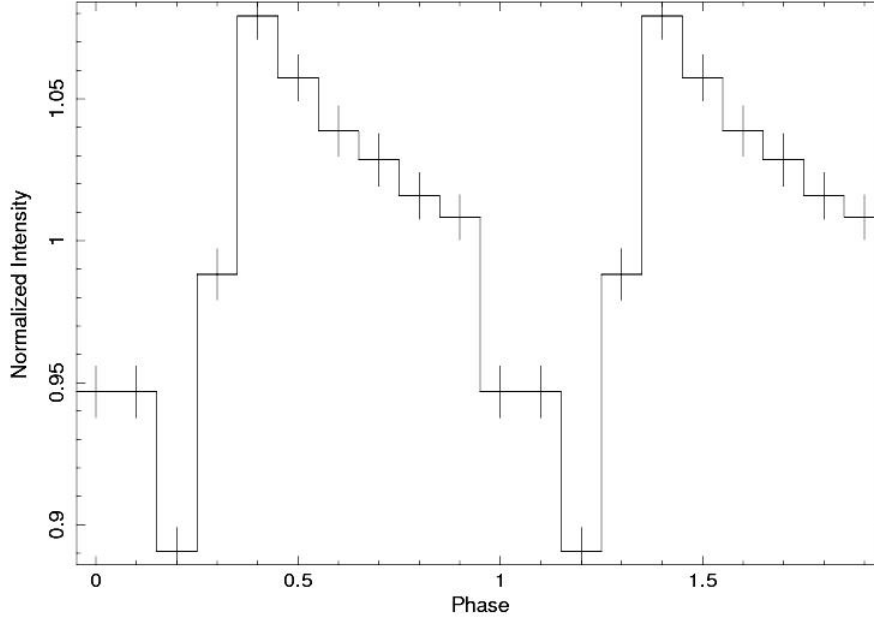


Figure 4.1: The light curve of PQ Gem folded over the orbital period (see text for ephemeris).

## 4.2 Analysis and Results

### 4.2.1 PQ Gem

In order to investigate the behaviour of the source over the orbital motion, the first thing to be done was to extract a light curve and fold it over the orbital period. The ephemeris given by Hellier (1997) was utilized for this purpose. The ephemeris given was  $\text{HJD}=2449333.984(4)+0.216359(3)\text{E}$  which was derived from the  $\text{H}_\beta$  profiles and phase 0 corresponds to the red to blue crossing of the lines. However, Hellier (1997) argues that the red to blue crossing does not correspond to the inferior conjunction of the secondary, but rather it is at the phase 0.75. Therefore we shifted the phase so that the phase zero of our folded light curve corresponds to the secondary conjunction and hence the ephemeris used was  $\text{HJD}=2449334.146(4)+0.216359(3)\text{E}$ . Due to the error on the orbital period, an accumulated error on the phase occurs in the folded XMM EPIC pn light curve which amounts to 0.2 in phase. The folded light curve is given in Figure 4.1.

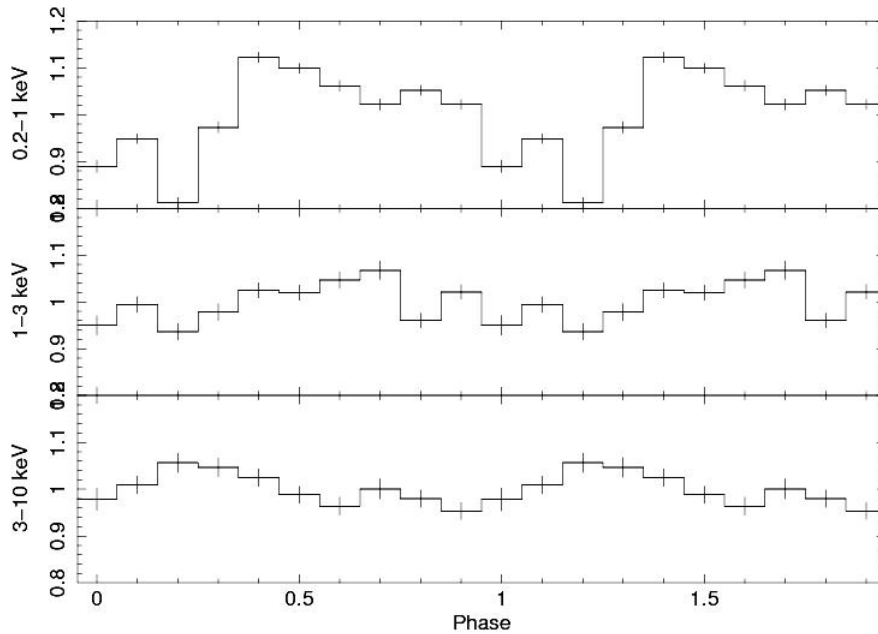


Figure 4.2: The lightcurves of PQ Gem extracted from three different energy ranges and folded over the orbital period (see text for ephemeris).

The X-ray flux varies with the orbital period as seen in the orbital fold, and there is about 20% modulation between the maximum and the minimum phases. The minimum phase is at 0.2, but there is error on the determined period which accumulates in time after several periods have elapsed. When trying to phase-lock the system from different epochs this accumulated error should be taken in consideration. Since error from phase locking is 0.2 in phase, it is possible that the Xray minimum is coincidence with the inferior conjunction of the secondary.

In order to further investigate the behaviour of the orbital modulation in X-rays and to account for the energy dependence of the modulation, we extracted lightcurves from three different energy ranges. We picked the ranges as 0.2-1.0 keV (soft), 1.0-3.0 keV (intermediate) and 3.0-10.0 keV (hard). Then we folded the energy dependent lightcurves over the orbital period. As seen in Figure4.2, the prominent X-ray modulation comes from the soft (0.2-1.0 keV) energies and the contribution from the harder energies are negligible.

Another feature to investigate was the hardness ratio in the system. We have looked



at the ratio of the fluxes of 3.0-10.0 keV lightcurve to the 0.2-1.0 keV lightcurve over the orbital period. The source obviously shows hardening during the orbital minimum phases, as the ratio increases by up to 30% of the value at other phases (See Figure4.3). We also closely examined higher energies among themselves, by extracting two lightcurves for 2.0-5.0 keV and 5.0-10.0 keV energy ranges. As seen in Figure4.3, there are no significant modulation at high energies, and the hardness ratio is similarly constant. Thus the modulation of the source in the X-rays and hardening clearly originates from the modulation by the softer energies.

As for the next step, in order to account for the origins of the X-ray modulation of the source over the orbital period, we extracted spectra from the orbital minima and orbital maxima, namely from the phase ranges 0.95-0.25 and 0.35-0.75 respectively. We have adopted the model proposed by Evans et al. (2006) found for the phase average spectrum of the source. Our composite model fitted the minimum and maximum spectra has 3 different absorptions, one total covering and two partial covering. For the continuum, there are 2 MEKAL emissions at different temperatures; a soft black-body emission; and a gaussian emission line at 6.4 keV. For the sake of constraining the complex fit, parameters such as first absorbing column, hard MEKAL temperature and the center of the Gaussian line were kept fixed. The absorbing column is kept at the value obtained from NASA HEASARC "NH TOOL" which uses Leiden/Argentine/Bonn (LAB) Survey of Galactic HI (Kalberla et al., 2005) to account for the interstellar absorption. The hard MEKAL temperature was fixed at the 40 keV which is the value found by Evans et al. (2006). Both minimum and maximum spectra gave reasonable fits with  $\chi^2_\nu$  values close to 1 (See Table4.1 and Figure4.4).

#### 4.2.2 V2069 Cyg

In a similar fashion, the first step into investigating the orbital behavior of the source, we folded the lightcurve of V2069 Cyg over the orbital period. The phases of the mean light curve was locked to the ephemerides given by Thorstensen & Taylor (2001),  $HJD = 2451066.783(2) + 0.311683(2)E$  where  $T_0$  corresponds to the red to blue crossing of the  $H_\alpha$  radial velocities. Due to the error on the orbital period, an accumulated error on the phase occurs in the folded XMM EPIC pn light curve which

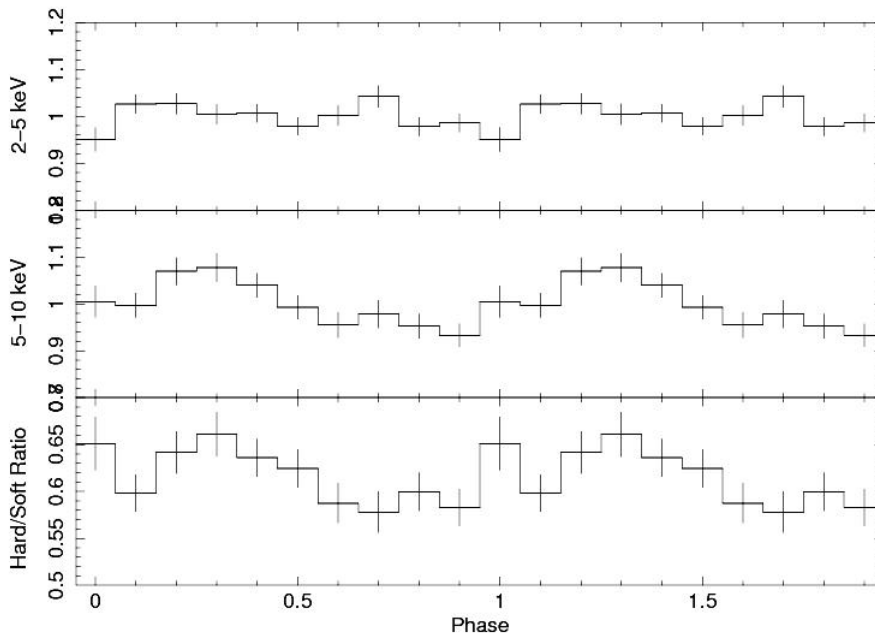
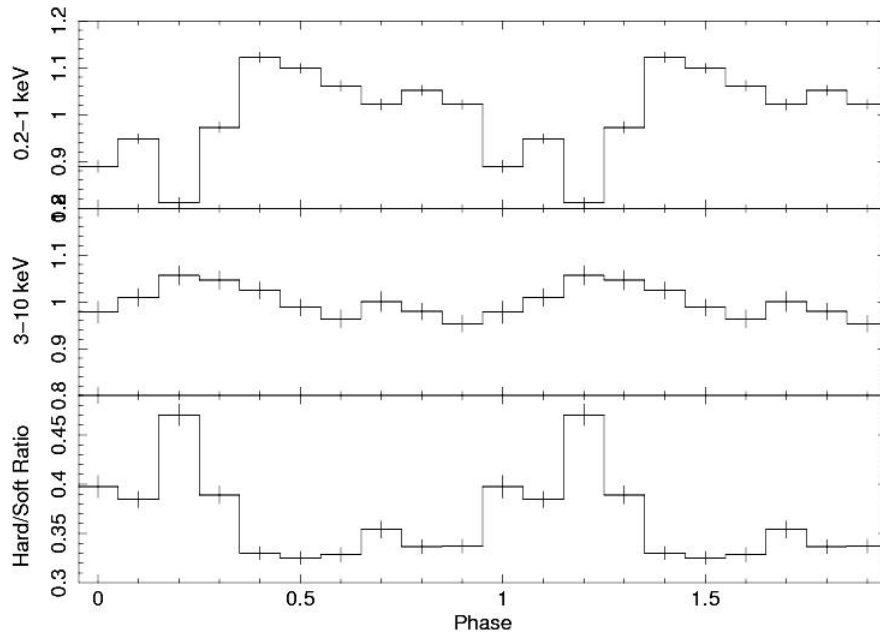


Figure 4.3: The top panel shows energy dependent PQ Gem lightcurves and hardness ratios for 0.2-1.0 keV and 3.0-10.0 keV folded on orbital period. The bottom panel shows energy dependent PQ Gem lightcurves and hardness ratios for 2.0-5.0 keV and 5.0-10.0 keV folded on orbital period.

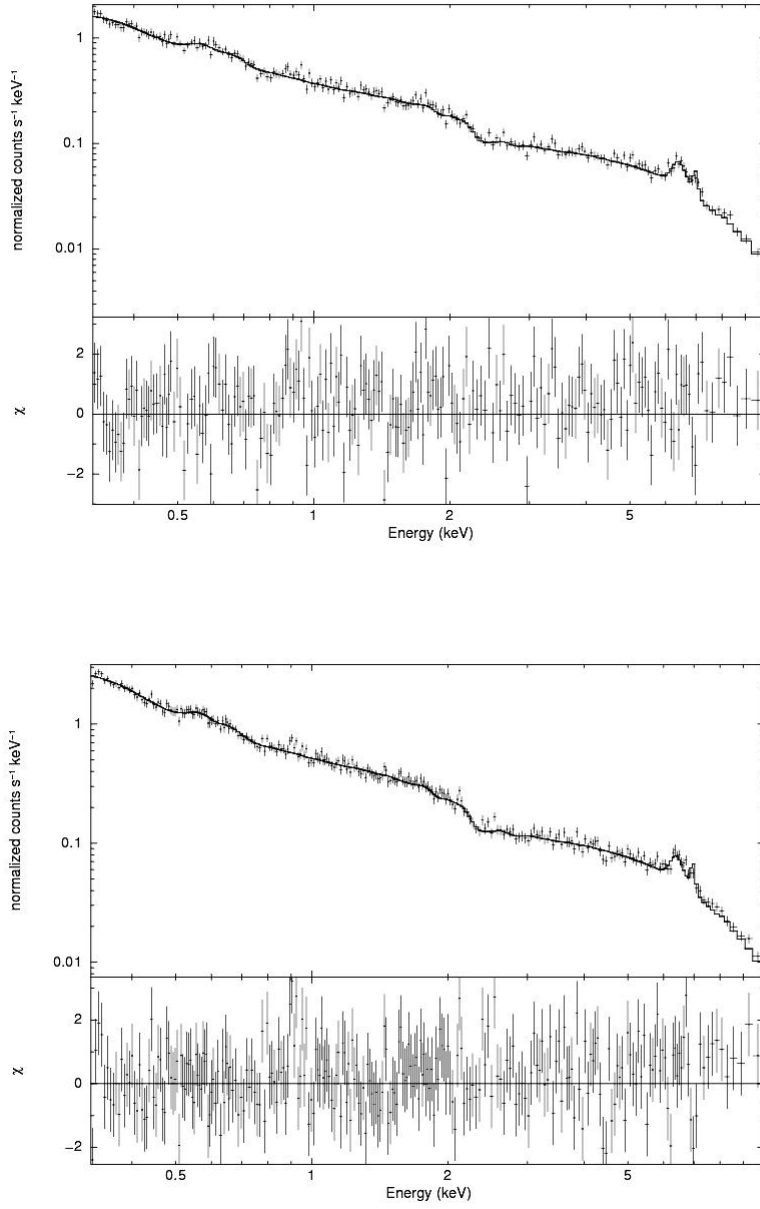


Figure 4.4: The minimum (at the top) and maximum (at the bottom) spectra of PQ Gem fit with the composite model.

Table 4.1: Spectral parameters derived from the fits to the orbital maxima and minima for PQ Gem. The model used is WABS\*PCFABS\*PCFABS\*(MEKAL+MEKAL+BBODY+GAUSS). All the errors are given in 90% confidence level.

Model	Component	Maxima	Minima
wabs	$N_{\text{H}} (\times 10^{22} \text{ cm}^{-2})$	0.35 (fixed)	0.35 (fixed)
pcfabs1	$N_{\text{H}} (\times 10^{22} \text{ cm}^{-2})$	< 0.001	$0.1^{+5.1}_{-0.06}$
	CoverFrac	<	$0.39^{+0.10}_{-0.16}$
pcfabs2	$N_{\text{H}} (\times 10^{22} \text{ cm}^{-2})$	$7.49^{+1.58}_{-1.29}$	$5.76^{+1.25}_{-1.00}$
	CoverFrac	$0.42^{+0.02}_{-0.02}$	$0.45^{+0.02}_{-0.03}$
MEKAL1	kT (keV)	$0.19^{+0.01}_{-0.01}$	$0.19^{+0.01}_{-0.01}$
	Norm	$0.00036^{+0.00004}_{-0.00004}$	$0.00036^{+0.00004}_{-0.00004}$
MEKAL2	kT (keV)	40 (fixed)	40 (fixed)
	Norm	$0.0048^{+0.0002}_{-0.0002}$	$0.0039^{+0.0003}_{-0.0003}$
Blackbody	kT (keV)	$0.044^{+0.002}_{-0.002}$	$0.045^{+0.002}_{-0.003}$
	Norm	$0.00036^{+0.00009}_{-0.00007}$	$0.00030^{+0.00012}_{-0.00008}$
Gaussian	$\sigma$ (keV)	$0.16^{+0.07}_{-0.05}$	$0.17^{+0.5}_{-0.4}$
	Norm ( $\times 10^{-5}$ )	$1.9^{+0.6}_{-0.5}$	$1.4^{+0.4}_{-0.4}$
$\chi^2_{\nu}$ (d.o.f.)		1.02 (836)	1.07 (753)

amounts to 0.08 in phase.

The mean light curve folded on the orbital period clearly shows a sinusoidal shape, with about a 20% dip around phase 0 and 0.1, and then quickly rising to a peak with about 30% modulation above the average at phases 0.6 and 0.7 as seen in Figure4.5.

Similar to PQ Gem, we also extracted lightcurves filtered on the energies in order to investigate the energy dependence of the orbital X-ray modulation. The lightcurves extracted from energy ranges 0.2-1.0 keV, 1.0-3.0 keV and 3.0-10.0 keV are displayed in Figure4.6. The lightcurves indicate a similar pattern of modulation, and unlike PQ Gem, they extend all the way upto the harder energies, although the amplitude of modulation decreases.

We also had a closer look on the hardening behaviour of the source. We plotted the ratio of the fluxes of 3.0-10.0 keV to 0.2-1.0 keV, and ratio of 2-5 keV to 5-10 keV fluxes over the orbital phases. The hardness ratio for V206 Cyg shows a similar expected pattern. The ratio between the 3-10 keV range and 0.2-1 keV range fluxes show anti-correlation with the folded lightcurves, significantly increasing during the orbital minimum phases, and decreasing during the orbital maximum phases. As

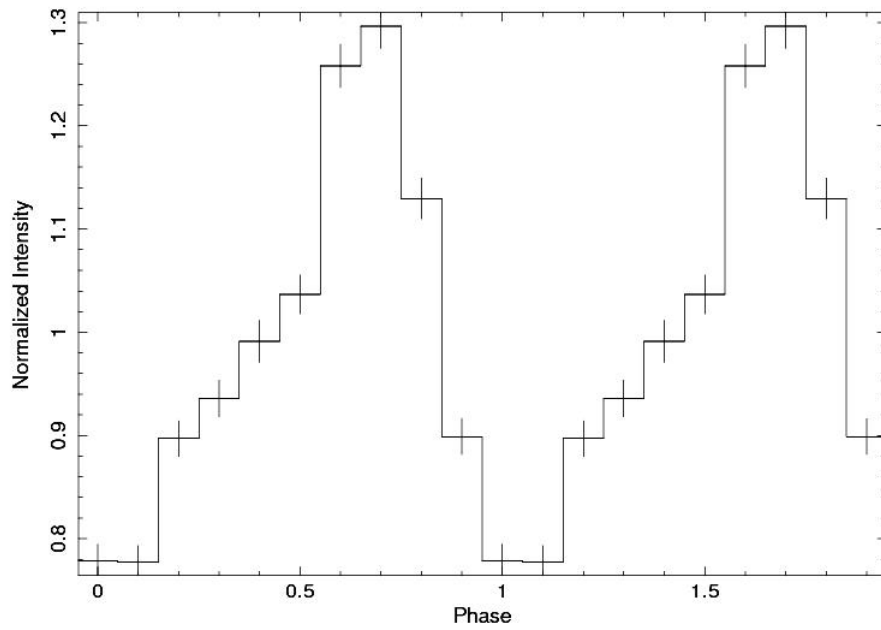


Figure 4.5: The light curve of V2069 Cyg folded over the orbital period (see text for ephemeris).

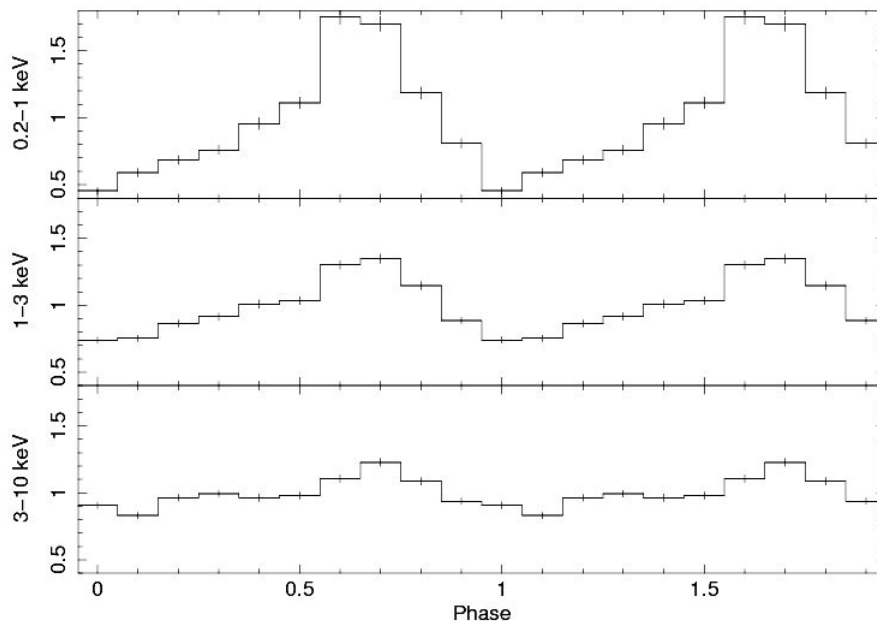


Figure 4.6: The lightcurves of V2069 Cyg extracted from three different energy ranges and folded over the orbital period (see text for ephemeris).

for the harder energies, although 2-5 keV and 5-10 keV lightcurves follow a similar pattern. The hardness variations shows no significant pattern over the orbital phase (See Figure4.7).

For the purpose of orbital phase resolved spectral analysis, we extracted X-ray spectra from the source corresponding to the dipping (0.9-1.2) and peak (0.5-0.8) phases. We adopted the composite model presented by Bernardini et al. (2012). The model consists of a simple absorber and a covering absorber, together with a blackbody, MEKAL and a Gaussian emission line component at 6.4 keV. The MEKAL temperature was fixed at 32 keV and the line centroid of the Gaussian emission was fixed at 6.4 keV. The resulting fits yielded  $\chi^2_\nu$  values of 0.96 for both minimum and maximum spectra. Variations to the model such as adding a second partial covering absorber or imposing separate absorption components for the blackbody and MEKAL emissions models resulted in unconstrained and non-physical parameter values. The Figure 4.8 displays model fit to the data and the spectral parameters derived from the fits are given in Table4.2 .

Table 4.2: Spectral parameters derived from the fits to the orbital maxima and minima for V2069 Cyg. The model used is WABS\*PCFABS\*(MEKAL+BBODY+GAUSS). All the errors are given in 90% confidence level.

Model	Component	Maxima	Minima
wabs	$N_H (\times 10^{22} \text{ cm}^{-2})$	$0.34^{+0.8}_{-0.07}$	$0.38^{+0.1}_{-0.08}$
pcfabs	$N_H (\times 10^{22} \text{ cm}^{-2})$	$10.9^{+5.1}_{-3.4}$	$6.38^{+2.51}_{-1.76}$
	CoverFrac	$0.54^{+0.04}_{-0.05}$	$0.63^{+0.04}_{-0.05}$
MEKAL	kT (keV)	32 (fixed)	32 (fixed)
	Norm	$0.0019^{+0.0002}_{-0.0001}$	$0.0017^{+0.0001}_{-0.0002}$
Blackbody	kT (keV)	$0.083^{+0.007}_{-0.006}$	$0.062^{+0.01}_{-0.01}$
	Norm ( $\times 10^{-5}$ )	$6.4^{+8.2}_{-3.8}$	$9.3^{+12.5}_{-5.4}$
Gaussian	$\sigma$ (keV)	$0.19^{+0.07}_{-0.06}$	$0.13^{+0.12}_{-0.08}$
	Norm ( $\times 10^{-5}$ )	$1.4^{+0.4}_{-0.3}$	$0.9^{+0.4}_{-0.3}$
$\chi^2_\nu$ (d.o.f.)		0.96 (833)	0.96 (595)

### 4.3 Discussion

Due to low inclination of the system, PQ Gem does not show substantial modulation over the orbital phase, the main pulsation rather comes from the spin period of the

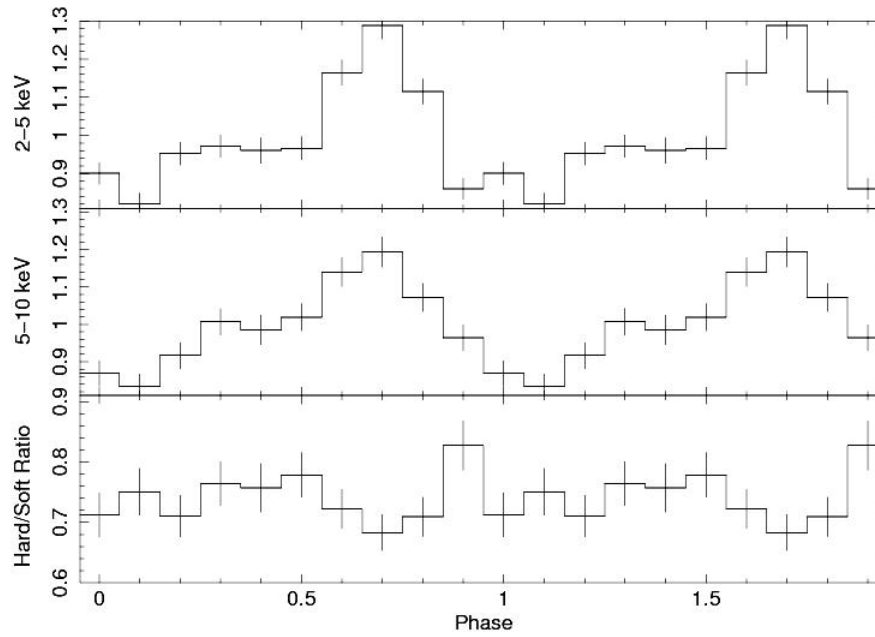
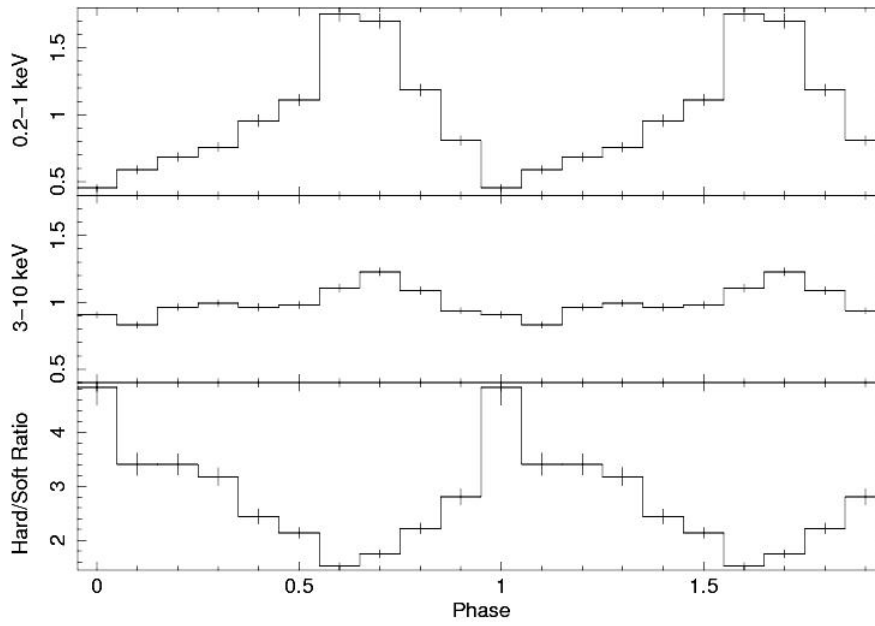


Figure 4.7: The top panel shows energy dependent V2069 Cyg lightcurves and hardness ratios for 0.2-1 keV and 3-10 keV folded on orbital period. The bottom panel shows energy dependent V2069 Cyg lightcurves and hardness ratios for 2-5 keV and 5-10 keV folded on orbital period.

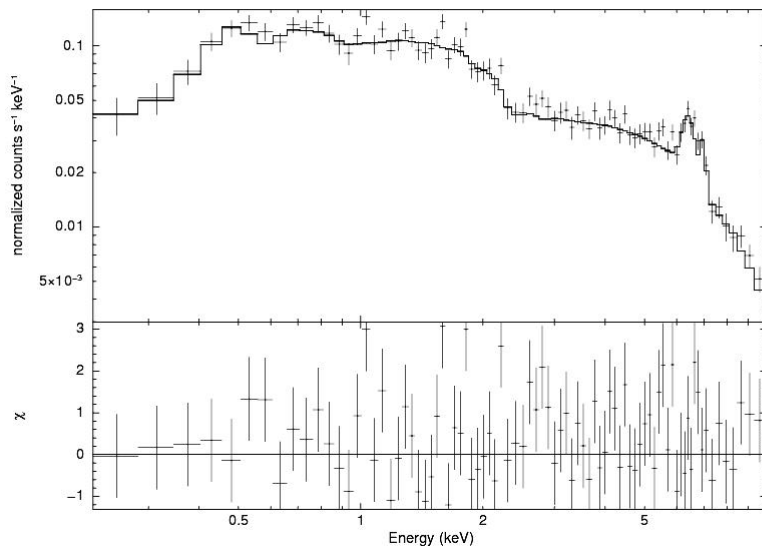
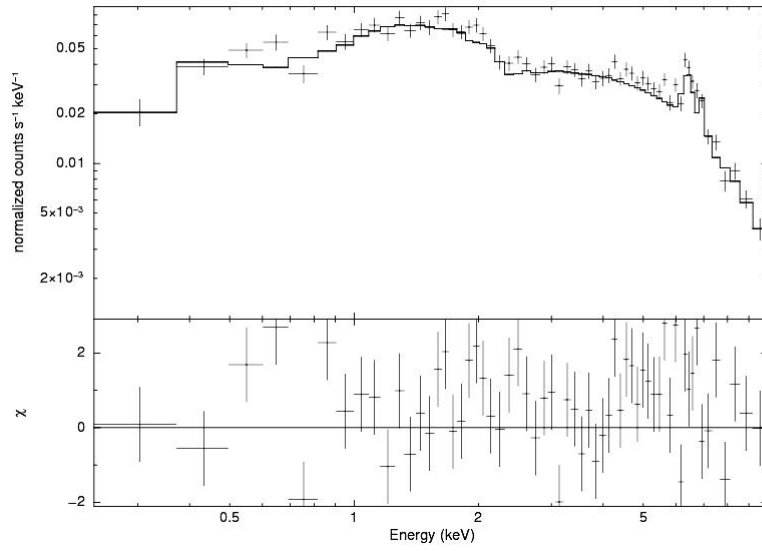


Figure 4.8: The minimum (at the top) and maximum (at the bottom) spectra of V2069 Cyg fit with the composite model.



white dwarf. In fact previous works rely on indirect spectroscopic measurements in order to determine the orbital period of the system (see Hellier 1997 and the references therein). RXTE and ASCA observations reveal a modulation of about 5% in amplitudes (Parker, Norton & Mukai 2005). Our normalized XMM Newton EPIC pn light curves folded on the orbital period reveal a modulation of about 10% from the average X-ray flux at the orbital minimum phase. This modulation increases at the lower energies. Moreover, the spectral hardening occurring at minimum phases are only prominent between the soft and hard energies, and no hardening is apparent at higher energies. Therefore, it is most likely that the modulation arises due to an absorbing bulge on the edge of the disk, which effects the lower energies. Occultation from the secondary and/or hot spot is not favorable.

The position of the orbital minimum corresponds to the phase 0.2 which lags the inferior conjunction of the secondary. However due to our large error of 0.2 phases from phase locking, this makes the minimum occurring between phases 0 and 0.4 which means that the absorbing bulge is probably related to the accretion stream impacting the disk, around the hot spot.

When we investigate the difference of spectral parameters between the spectra at the maximum and minimum, it supports the absorption from the bulge scenario. We could resolve the absorption from the system into three distinct components. The first one is the common interstellar absorption represented by the wabs component in the composite model. The second one is the high absorbing component showing not much difference between the orbital minima and maxima in terms of absorption and covering fraction. This can be attributed to the high absorption resulting from the accretion curtains. We expect to see a constant absorption since the effect of accretion curtains are averaged out over the orbital phase bins. The last component is the low absorption pcfabs component. While much smaller than the contribution from the absorption from the curtains, this component vanishes at the orbital maximum both in absorbing column and covering fraction. Hence this corresponds to the absorption from the bulge at the edge of the disk, which only enters in the line of sight during the orbital minima and absent during the maxima.

V2069 Cyg has a more prominent X-ray modulation over the orbital phase. The

modulation depth substantially decreases at the higher energies, indicating the effect of the absorption in the system. The hardening of the source also supports this idea, such that the hardening of the source arises from the decrease in the softer energy flux. At higher energies no distinct hardening occurs at the orbital minima, despite the orbital modulation persists. This may indicate that occultation can also play a role in the orbital modulation along with the absorption, modulating the flux even at higher energies.

The orbital minimum is around 0-0.1 orbital phases, which coincides with the inferior conjunction of the secondary within accumulated errors from phase locking. Another interesting feature to note is that the orbital minimum shifts by 0.1 phase to the right at higher energies. This can be explained with the combined absorption/occultation effect. A possible scenario is that the region responsible for the occultation (most probably the limb of the secondary) lies close within 0.1 phase of the region responsible for the absorption (bulge on the disk around hot spot). However, this may also be due to the 0.1 error in phase from phase-locking.

Spectral analysis has been unfruitful in successfully distinguishing between each absorption components for V2069 Cyg, since only two different components could be fit to the data. So, apart from the interstellar absorption represented by the wabs component in the model, the disk and the absorption curtain both contribute to the second absorption component. Different absorption combinations, or trying to fit separate absorbers for soft and hard emission was not successful in producing a meaningful fit. The fits reveal that the absorbing column is higher during the orbital maxima than minima and the covering fraction does not show a dramatic difference. Even considering that the absorbing column values are similar within error margins, these values are quite unexpected. The light curve analysis clearly indicates an increase in absorption during the minima but the spectral analysis cannot account for the increase in absorption. One possible scenario here is since disk and curtain absorption effects mix up, the increase in absorbing column is not represented in the fit. Since the observation time is short, only one orbital period is covered in the data, and the absorption components may not be constrained due to lack of data. The other possible explanation could be that the bulge spread over the disk, making a same contribution to the absorption throughout the orbital motion, but has a much larger area during the

orbital minima, explaining the rise in the covering fraction, but this is unlikely since the change in covering fraction is marginal.

The other distinct difference between the orbital minimum and maximum spectra is the soft blackbody component getting softer during the minima in V2069 Cyg. In PQ Gem, this component is the same between minimum and maximum. This may indicate that the blackbody emission is further reprocessed by the bulge during orbital minima.



## CHAPTER 5

### V2491 CYG AND V4743 SGR

In this chapter, we reanalyze a selection of the XMM-Newton RGS (Reflection Grating Spectrometer) data of two classical novae; V4743 Sgr and V2491 Cyg. The High resolution nova spectra in the X-ray wavelengths show the existence of absorption features. Our main aim is to model the absorption components detected in the high resolution spectra independently from the assumed continuum model. Moreover, we will obtain abundances of elements in the ejecta/nova wind. In comparison with previous modeling of individual absorption features with Gaussians, we are utilizing photo-ionized warm absorber models and collisionally ionized absorber models that we discuss in the light of observations.

Nova 4743 Sgr is discovered in September 2002 reaching  $V = 5$  magnitudes (Haseda et al. 2002). It is a very fast nova with time to decay by 3 magnitudes of 15 days and the FWHM of the  $H\alpha$  line shows large velocities of the order of  $2400 \text{ km s}^{-1}$  (Kato et al. 2002). The distance to the nova is estimated to be about  $1.2 \pm 0.3 \text{ kpc}$  (Nielbock & Schmidtobreick 2003).

Nova 2491 Cyg is discovered in April 2008 at about 7.7 mag on unfiltered CCD frames (Nakano et al. 2008). Assuming 7.54 mag for the maximum  $t_2$  is about 4.6 days making this nova a very fast nova similar to V838 Her and V2487 Oph. V2491 Cyg has been classified as a He/N nova based on photometric and spectroscopic results (Lynch et al. 2008, Helton et al. 2008). It shows extremely broad lines with complex profiles and large expansion velocities ( $\sim 4000\text{-}6000 \text{ km s}^{-1}$ ) (Lynch et al. 2008, Tomov et al. 2008). Ibarra et al. (2009) show that V2491 was a persistent X-ray source using archival *ROSAT*, *XMM-Newton*, and *Swift* data during its quiescent time before

the optical outburst. Both of the novae we analyze in this chapter show the hard X-ray and the soft X-ray component during the outburst stage (V4743 Sgr: Ness et al. 2003, Rauch et al. 2010; V2491 Cyg: Page et al. 2010).

## 5.1 The Data and Observations

V2491 Cyg was observed (pointed archival observation, OBSID=0552270501) for an exposure of 39 ks between 2008 May 20 UT 14:03:53 and 2008 May 21 UT 00:59:28. V4743 Sgr was observed (pointed archival observation, OBSID=0127720501) by *XMM-Newton* for an exposure of 35 ks between 2003 April 4 22:24:12 and 2003 April 5 08:13:34. Both sources were observed by all the EPIC cameras using different modes, but we utilize the RGS data to obtain the high resolution spectra for our analysis purpose. For the analysis, we reprocessed the data using the XMM-SAS routine RGSPROC. RGSPROC allows the user to restrict the processing to an enumerated subset of exposures within the observation and an enumerated set of reflection orders.

The final exposure times and net count rates showed that there were no sporadic high background events in our data and since both of the nova were very bright, we did not include any corrections for flares. Source and background counts for the RGS were extracted using the standard spatial and energy filters; for the source position, which defines the spatial extraction regions as well as the wavelength zero point. For adequacy, simplicity and its better quality, we used RGS(1) 1st order data for our analysis purpose. The RGS(1) net count rate of V2491 Cyg was found as  $3.17 \pm 0.02 \text{ c s}^{-1}$  and the net count rate of V4743 Sgr was  $50.9 \pm 0.04 \text{ c s}^{-1}$ .

## 5.2 Analysis and Results

### 5.2.1 Warm and Hot Absorber Models

We used two absorption models within the SPEX software (Kaastra et al. 1996) to model our data along with a simple blackbody emission component for the continuum. SPEX is a software package optimized for the analysis and interpretation of

high-resolution cosmic X-ray spectra. The software is especially suited for fitting spectra obtained by current X-ray observatories like *XMM-Newton*, *Chandra*, and *Suzaku*. It is maintained by SRON (HEA Division, Netherlands Institute for Space Research).

One of the models we used in our analysis is the XABS model of SPEX, which calculates the absorption by a thin slab composed of different ions, located between the ionizing source and the observer. The relative column densities of the ions are calculated through a photo-ionization model introducing two free parameters:  $N_{\text{H}}^{\text{xabs}}$  and  $\xi$ .  $N_{\text{H}}^{\text{xabs}}$  is the equivalent hydrogen column density of the ionized absorber in units of atoms  $\text{cm}^{-2}$ .  $\xi$  is the ionization parameter of the absorber defined as  $\xi = L/n_e r^2$ , where  $L$  is the luminosity of the ionizing source,  $n_e$  the electron density of the plasma and  $r$  the distance between the slab and the ionizing source.  $\xi$  is expressed in units of  $\text{erg cm s}^{-1}$ .

Other than the XABS model within SPEX, we also utilized the HOT model that assumes a collisional ionization equilibrium absorption model instead of the photo-ionized absorber model. This model calculates the transmission of a plasma in collisional equilibrium with cosmic abundances. For a given temperature and abundances, the model calculates the ionization balance and then determines all ionic column densities by scaling the prescribed hydrogen column density. Using these column densities, the transmission of the plasma is calculated by multiplying the transmission of the individual ions. It, also, has similar free parameters to those in XABS model like velocity shift  $v$  and turbulent velocity broadening  $\sigma_v$  together with  $N_{\text{H}}^{\text{Hot}}$ , equivalent hydrogen column density and  $kT$ , temperature, of the absorber in keV.

### 5.2.2 *XMM-Newton* RGS Spectrum of V2491 Cyg and V4743 Sgr

We analyzed the data using Science Analysis Software (SAS) version 11.0.0. Some spectral analysis checks were performed using XSPEC (Arnaud 1996) version 12.5.1n, and the main analysis were conducted with the SPEX software package (Kaastra et al. 1996) version 2.02.04. The photo-electric cross sections of Morrison & McCammon (1983) were used throughout to account for absorption by neutral gas with solar abundances (Anders & Grevesse 1989, ABSM model within SPEX). Spectral uncertainties

in our analysis correspond to 99.9% confidence level for one parameter of interest.

We used two different absorption models XABS and HOT in the SPEX software package together with a blackbody model for the continuum and ABSM model for the neutral hydrogen absorption in the line of sight. We used the RGS1 data (since it was adequate for our analysis) for both of the nova and fitted the spectra with two composite models of ABSM×XABS×BLACKBODY and ABSM×HOT×BLACKBODY. The fitted spectra of V2491 Cyg can be found in Figure 5.1 and Figure 5.2 for XABS and HOT model fits respectively. Figure 5.3 and Figure 5.4 display the XABS and HOT model fits to the V4743 Sgr data. The resulting spectral parameters from fits with the XABS model is listed on Table 5.1 for V2491 Cyg and on Table 5.3 for V4743 Sgr. The spectral parameters from the fits with the HOT absorber model are presented on Table 5.2 for V2491 Cyg and on Table 5.4 for V4743 Sgr.

We generally find high  $\chi^2_\nu$  values for all fits. We find that the fits yield  $\chi^2_\nu=25.5$  using the HOT model and  $\chi^2_\nu=27.3$  using the XABS model for the classical nova V2491 Cyg. As for V4743 Sgr, we find that the fits yield  $\chi^2_\nu=72$  using the HOT model and  $\chi^2_\nu=57$  using the XABS model. We have assumed mainly solar abundances in the fitting procedures except for CNO abundances. In order to show the quality of the used models and the detailed absorption lines in the models, we have constructed Figure 5.5 which display the best fitted models (models only) to the two novae of XABS and HOT models.

In addition to the simple model fitting, we tried a more complex model on the V2491 Cyg data. Adopting this ionized absorber approach, Pinto et al. (2012) proposed such a complex model. They extracted 3 spectra from 3 different time domains and fitted them with a composite model with 3 separate XABS components. This way, they greatly improved the fits with  $\chi^2$  values of 2.4, 2.7 and 7.1. Hence, we did a similar fit to the V2491 Cyg data. First we plotted the lightcurve of the source and chose 3 separate regions as used by Pinto et al. (2012). The lightcurve and the regions are displayed in Figure 5.6. We extracted rgs1 and rgs2 count rate spectra for each region and then combined the rgs1 and rgs2 spectra. Then for each spectrum, we fitted a combined model of blackbody and a hot plasma (CIE in SPEX) for the continuum, a HOT component with low temperature for the cold absorption, and 3 HOT components



Table 5.1: The spectral parameters from the fit with the RGS spectrum of V2491 Cyg using the XABS model in SPEX.

MODEL	PARAMETER	VALUE
blackbody	norm ( $10^{20}$ cm $^2$ )	3107.7 $^{+11.4}_{-195.2}$
	temperature (keV)	0.0541 $^{+0.0001}_{-0.0005}$
xabs	$N_{\text{H}}^{\text{xabs}}$ ( $10^{24}$ cm $^{-2}$ )	0.057 $^{+0.021}_{-0.005}$
	log xi (erg cm $^2$ s $^{-1}$ )	2.10 $^{+0.02}_{-0.01}$
	$\sigma_{\text{v}}$ rms velocity (km/s)	828.6 $^{+33.5}_{-69.2}$
	velocity shift (km/s)	-3201.6 $^{+11.0}_{-121.9}$
	C abundance	4.4 $^{+2.1}_{-0.5}$
	N abundance	5.7 $^{+5.9}_{-0.7}$
	O abundance	10.8 $^{+9.9}_{-0.9}$
absm	Column ( $10^{24}$ cm $^{-2}$ )	0.00398 $^{+0.00003}_{-0.00001}$
	$\chi^2_{\nu}$ (d.o.f)	27.3 (1276)

(instead of XABS) at different temperatures. For Region 1 and Region 2, we also had to include 2 Gaussian components at 15.395 and 16.374 Å in order to improve the fits. We find lower  $\chi^2$  values: 1.69 (3061 d.o.f.), 1.99 (3064 d.o.f.) and 3.44 (3059 d.o.f.) for Region 1, 2 and 3 respectively. Different combinations of XABS and HOT models yielded worse fits. The extracted spectra and the respective fits are presented in Figure 5.7 and the parameters from the fit are given in Table 5.5. The parameters for the elemental abundances were fixed on the values given by Pinto et al. (2012). Trials for fitting similar complex model to the V4743 Sgr data were unsuccessful.

### 5.3 Discussion

In a nova explosion, convection and radiation pressure leads to the ejection of the envelope material, forming an optically thick shell where the high energy photons produced by the nuclear burning have to travel through. The resultant spectrum is an atmospheric spectrum originating from the photosphere with a blackbody-like continuum and superimposed absorption lines as detected by X-ray grating data. Previously, such X-ray spectra were fitted with LTE (Local Thermodynamic Equilibrium) atmosphere models with a success, albeit for low resolution data (e.g, Balman, Krautter, Ögelman 1998, Kahabka et al. 1999, Balman & Krautter 2001). For higher resolution data, static and expanding NLTE atmosphere models were tried instead, in

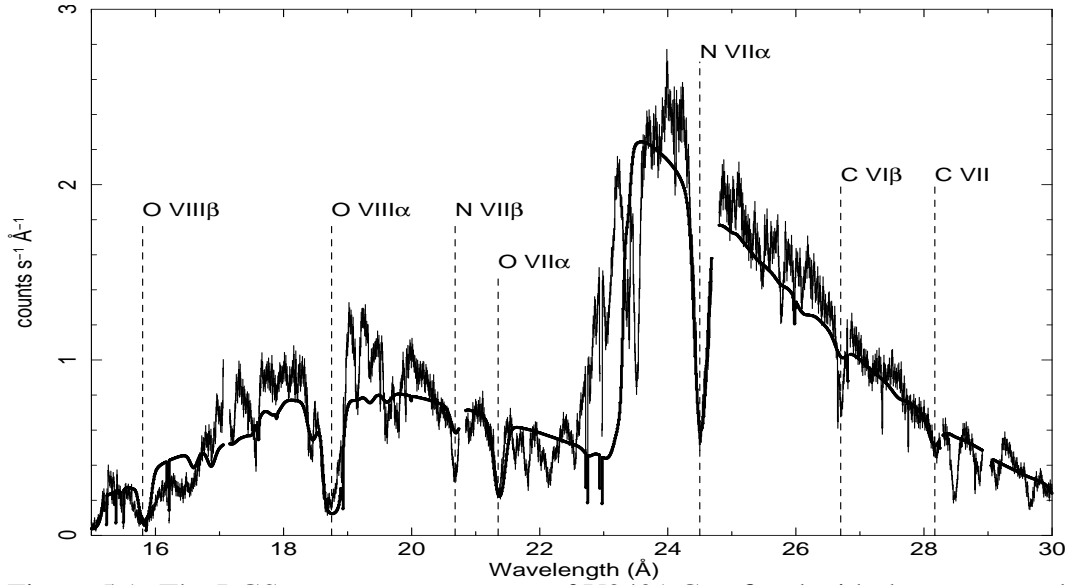


Figure 5.1: The RGS count rate spectrum of V2491 Cyg fitted with the XABS model in SPEX. Certain detected blue-shifted absorption lines are labeled with dashed lines.

Table 5.2: The spectral parameters from the fit with the RGS spectrum of V2491 Cyg using the HOT model in SPEX.

MODEL	PARAMETER	VALUE
blackbody	norm ( $10^{20} \text{ cm}^{-2}$ )	$1607.7^{+154.6}_{-143.4}$
	temperature (keV)	$0.0584^{+0.0005}_{-0.0004}$
hot	$N_{\text{H}}^{\text{Hot}}$ ( $10^{24} \text{ cm}^{-2}$ )	$0.0034^{+0.0002}_{-0.0002}$
	temperature (keV)	$0.165^{+0.003}_{-0.003}$
	$\sigma_v$ rms velocity (km/s)	$291.6^{+14.7}_{-14.5}$
	velocity shift (km/s)	$-3427.5^{+17.9}_{-26.4}$
	C abundance	$1.5^{+0.4}_{-0.3}$
	N abundance	$14.3^{+21.7}_{-0.1}$
	O abundance	$2.6^{+0.1}_{-1.3}$
absm	Column ( $10^{24} \text{ cm}^{-2}$ )	$0.003920^{+0.000004}_{-0.000004}$
	$\chi^2_{\nu}$ (d.o.f)	25.5 (1276)

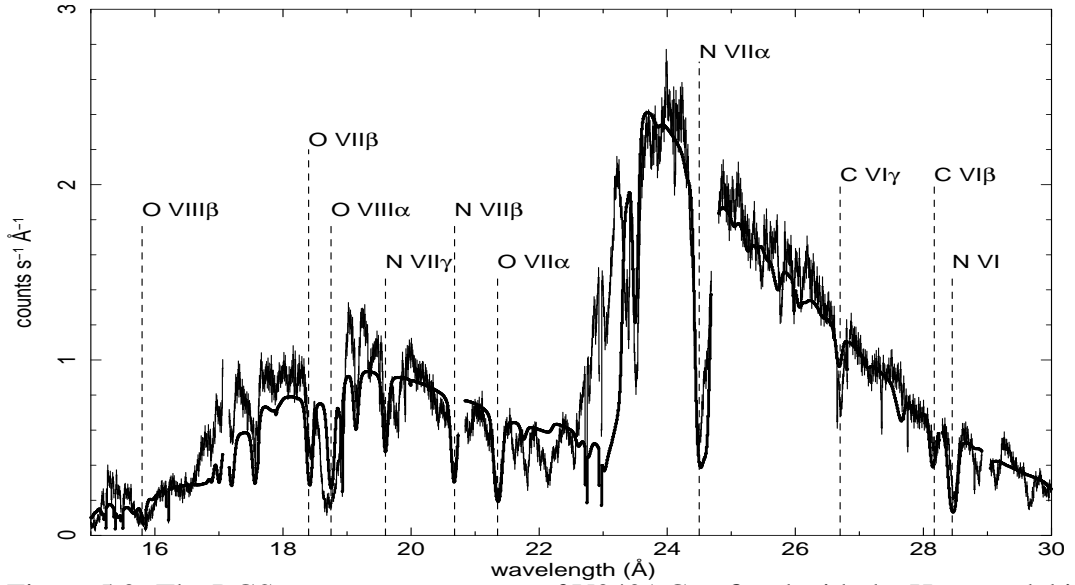


Figure 5.2: The RGS count rate spectrum of V2491 Cyg fitted with the HOT model in SPEX. Certain detected blue-shifted absorption lines are labeled with dashed lines.

Table 5.3: The spectral parameters from the fit with the RGS spectrum of V4743 Sgr using the XABS model in SPEX.

MODEL	PARAMETER	VALUE
blackbody	norm ( $10^{20}$ cm $^2$ )	174423 $^{+80443}_{-39890}$
	temperature (keV)	0.036 $^{+0.001}_{-0.001}$
xabs	$N_{\text{H}}^{\text{xabs}}$ ( $10^{24}$ cm $^{-2}$ )	0.40 $^{+0.30}_{-0.03}$
	log $\xi$ (erg cm $^2$ s $^{-1}$ )	2.30 $^{+0.02}_{-0.01}$
	$\sigma_v$ rms velocity (km/s)	783.8 $^{+7.2}_{-126.0}$
	velocity shift (km/s)	-1429.6 $^{+173.5}_{-112.9}$
	C abundance	0.18 $^{+0.18}_{-0.07}$
	N abundance	40.0 $^{+12.6}_{-0.3}$
	O abundance	25.5 $^{+1.3}_{-1.2}$
absm	Column ( $10^{24}$ cm $^{-2}$ )	0.00195 $^{+0.00012}_{-0.00006}$
	$\chi^2_{\nu}$ (d.o.f)	57.2 (1543)

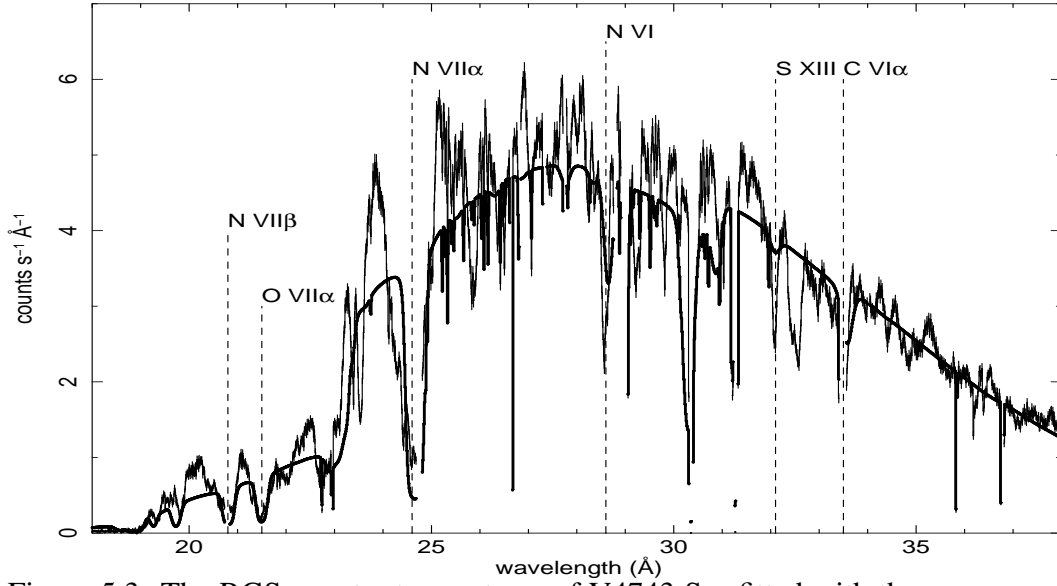


Figure 5.3: The RGS count rate spectrum of V4743 Sgr fitted with the XABS model in SPEX. Certain detected blue-shifted absorption lines are labeled with dashed lines.

Table 5.4: The spectral parameters from the fit with the RGS spectrum of V4743 Sgr using the HOT model in SPEX.

MODEL	PARAMETER	VALUE
blackbody	norm ( $10^{20}$ cm $^2$ )	58292 $^{+15497}_{-92}$
	temperature (keV)	0.0392 $^{+0.0006}_{-0.0001}$
hot	$N_{\text{H}}^{\text{Hot}}$ ( $10^{24}$ cm $^{-2}$ )	0.37 $^{+0.01}_{-0.01}$
	temperature (keV)	0.40 $^{+1.9}_{-0.01}$
	$\sigma_v$ rms velocity (km/s)	59.5 $^{+1.7}_{-1.0}$
	velocity shift (km/s)	-1088.3 $^{+0.9}_{-2.8}$
	C abundance	0.0036 $^{+0.0317}_{-0.0001}$
absm	N abundance	11.8 $^{+16.6}_{0.1}$
	O abundance	49.9 $^{+3.1}_{-1.6}$
	Column ( $10^{24}$ cm $^{-2}$ )	0.00174 $^{+0.00001}_{-0.00004}$
	$\chi^2_{\nu}$ (d.o.f)	72 (1543)

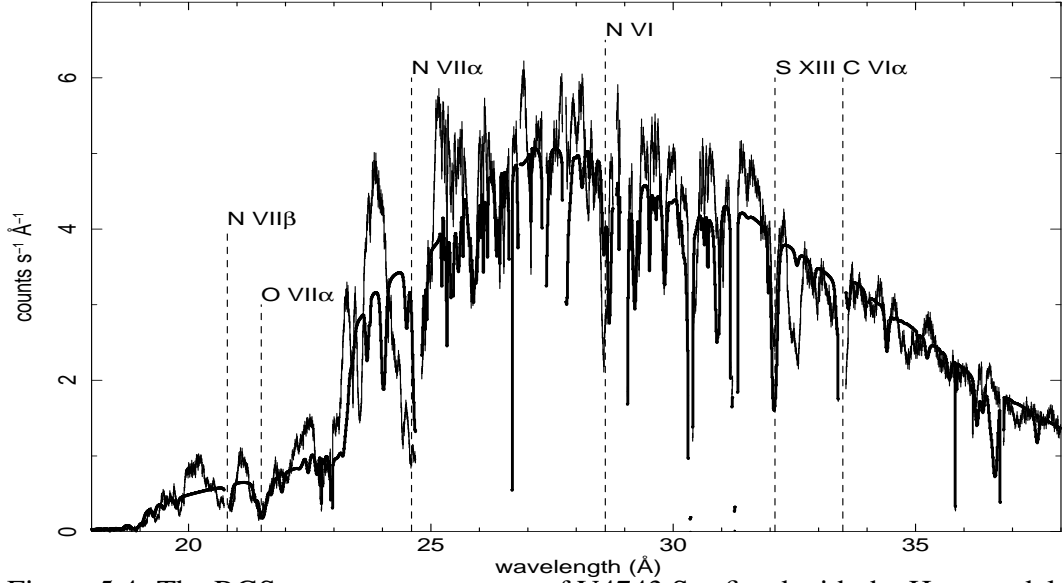


Figure 5.4: The RGS count rate spectrum of V4743 Sgr fitted with the HOT model in SPEX. Certain detected blue-shifted absorption lines are labeled with dashed lines.

Table 5.5: The spectral parameters from the fit with the RGS spectrum of V2491 Cyg using 3 HOT models. Region 1, 2 and 3 correspond to the time extraction regions where the total spectrum was divided into.

MODEL	PARAMETER	REGION 1	REGION 2	REGION 3
blackbody	norm ( $10^{20} \text{ cm}^2$ )	58.5	26.0	64.5
	temperature (keV)	0.098	0.71	0.12
hot1	$N_{\text{H}}^{\text{xabs}}$ ( $10^{24} \text{ cm}^{-2}$ )	0.058	0.024	0.075
	temperature (keV)	0.69	0.66	0.74
	$\sigma_v$ rms velocity (km/s)	1041	1041 (fixed)	1041 (fixed)
	velocity shift (km/s)	-3676	-3676 (fixed)	-3676 (fixed)
hot2	$N_{\text{H}}^{\text{xabs}}$ ( $10^{24} \text{ cm}^{-2}$ )	1.97	0.81	2.86
	temperature (keV)	0.86	1.09	0.88
	$\sigma_v$ rms velocity (km/s)	20	10 (fixed)	20 (fixed)
	velocity shift (km/s)	-3607	-3607 (fixed)	-3607 (fixed)
hot3	$N_{\text{H}}^{\text{xabs}}$ ( $10^{24} \text{ cm}^{-2}$ )	0.036	0.013	0.13
	temperature (keV)	0.15	0.16	0.25
	$\sigma_v$ rms velocity (km/s)	87.1	87.1 (fixed)	87.1 (fixed)
	velocity shift (km/s)	-3078	-3078 (fixed)	-3078 (fixed)
gauss1 (0.805 keV)	FWHM (keV)	0.018	N/A	0.019
	norm ( $\times 10^{44} \text{ ph/s}$ )	24.7	N/A	144
gauss2 (0.757 keV)	FWHM (keV)	0.035	N/A	0.035
	norm ( $\times 10^{44} \text{ ph/s}$ )	43.4	N/A	43.4
	$\chi^2_{\nu}$ (d.o.f)	1.69 (3061)	1.99 (3064)	3.44 (3059)

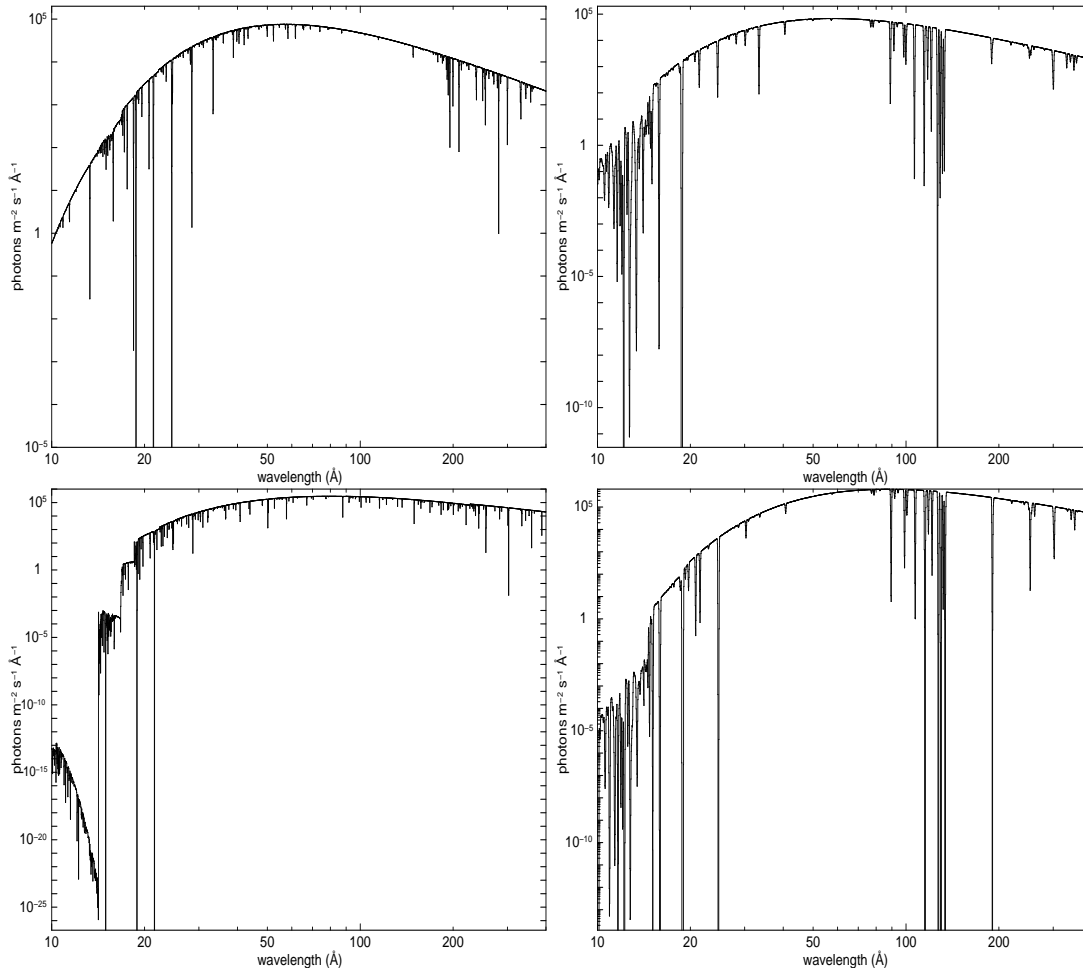


Figure 5.5: The figure shows the best fit models to the RGS data of V2491 Cyg and V4743 Sgr (from Tables 1-4) in photon flux. Upper lefthand panel is the best fit HOT model for V2491 Cyg and the upper righthand panel displays the best fit XABS model for the same nova. The lower lefthand panel is the best fit HOT model for V4743 Sgr and the lower righthand panel shows the best fit XABS model for the same nova. We note that we have assumed zero absorption of neutral hydrogen in the line of sight, when plotting the models. Thus, the only absorption is of the HOT or XABS models.

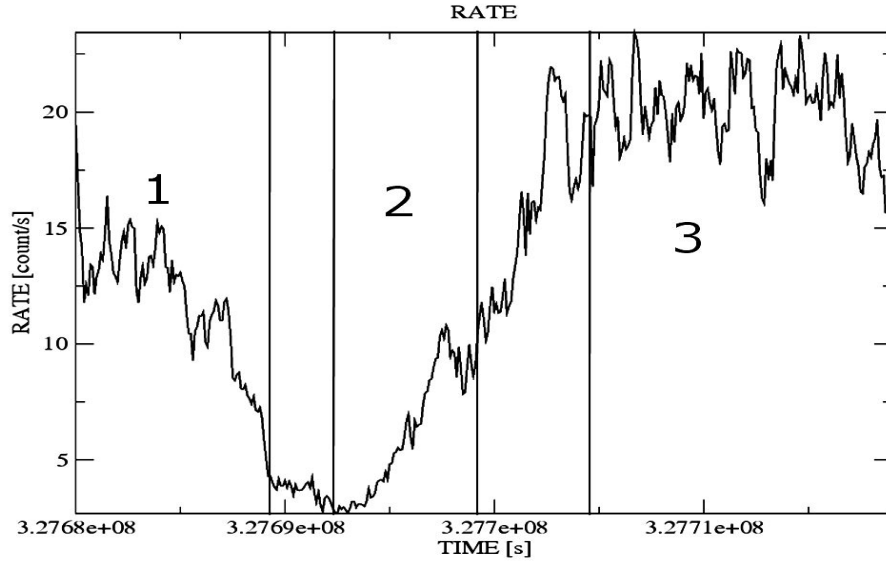


Figure 5.6: The lightcurve of V2069 Cyg and the selected regions for spectrum extraction.

order to account for the rich absorption features and line velocities observed in the spectra. However, these atmosphere models could not produce successful results, resulting in large  $\chi^2$  values and could not explain the detailed absorption features (e.g. Orio et al. 2002, Nelson et al. 2008, Rauch et al. 2010, Osborne et al. 2011, Ness et al. 2011, Petz et al. 2005, Rossum & Ness 2010).

Our approach is to mainly model the absorption components in the X-ray spectroscopic data. This is an independent approach in regards to the choice of the continuum emission with the atmosphere models being expanding or static. We are assuming a simple continuum model, a blackbody emission model, so that the complicated absorption models are thoroughly investigated. We utilize either a photo-ionized absorber or a collisionally ionized absorber along with a model of neutral hydrogen column density in the line of sight.

We derive a blackbody temperature of 52-59 eV ( $6-7 \times 10^5$  K), this value is larger than the value obtained from *Swift* (Page et al. 2010), but in very good agreement with the effective temperature of  $6 \times 10^5$  K obtained from the best fit approximations to the *XMM-Newton* data (day 49.7) using expanding NLTE atmosphere models (Rossum & Ness 2010). Thus, our blackbody continuum is a good/adequate representation for the continuum emission. Our fitted results with the HOT model for

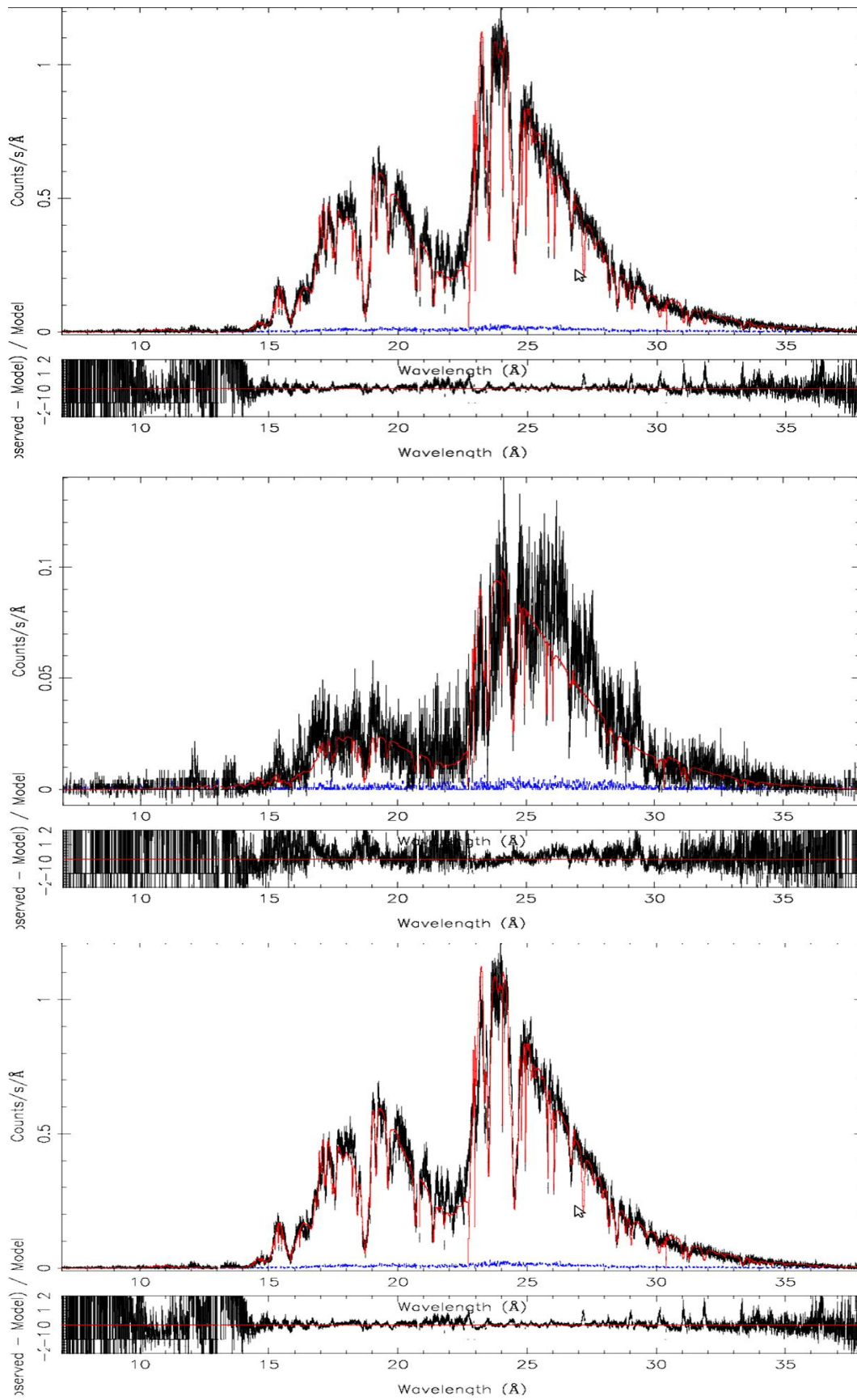


Figure 5.7: The composite model fit to the time filtered V2491 Cyg spectra. Region 1 at top, Region 2 in the middle, and Region 3 at the bottom.



a collisionally ionized absorber yield abundances of C=1.2-2.0 O=1.2-2.7 N=14-36 (values are the ratio to solar abundance) which are consistent with the *Swift* results. This in turn, will make the photo-ionized warm absorber model physically less likely since enhanced oxygen O=10-21 (value is the ratio to solar abundance) is obtained from our fits. Our CNO abundances derived from the fits to the RGS data are the first detailed abundance calculation from the X-ray data. We derive a neutral hydrogen column density of about  $4.0 \times 10^{21} \text{ cm}^{-2}$  from our fits which is the same with the listed value in Dickey and Lockman (1990) and also similar to the value measured from the *Swift* data. We find a self-consistent blue-shift in a range 3078-3445 km s<sup>-1</sup> from the *XMM-Newton* data via fitting all the absorption lines simultaneously which is a unique result and consistent with wind/ejecta expansion velocities.

The complex model with 3 HOT absorber models proved to yield better fits. However, the inclusion of Gaussian emission lines poses a problem. If we assume that the lines come from a source at rest, 15.395 Å and 16.374 Å correspond to Fe XVIII and Fe XIX transitions respectively, according to the CHIANTI Atomic Database. If we assume that these lines are blueshifted with 3600 km/s as found in the fits, the original lines are from 15.579 Å and 16.570 Å, corresponding to Fe XX and Fe XIX respectively. Instead of fitting Gaussian to these lines, we tried to compensate these emission lines by changing the abundances in the plasma emission component (CIE in SPEX). This action did not have any effect to the fit around these lines. Hence we cannot give a physical explanation for these two strong emission lines. Moreover, although the  $\chi^2_\nu$  values improve, there are still numerous absorption features that cannot be fit properly. Varying abundances, line blueshifts and turbulent velocities in order to fit these lines may be a solution. However since there are three different ionized absorber components with quite a large number of variables, efforts on constraining these parameters were unsuccessful. On the other hand, we seem to obtain relatively better fits with HOT models than those made with XABS. Hence our initial interpretation with the simple model is more favoured i.e. that the spectrum is more compatible with collisionally ionized absorber than photoionized absorber.

The *XMM-Newton* RGS data of V4743 Sgr have been modeled using NLTE static atmosphere models. Suitable fits with best approximations to the data have been achieved with models having fixed abundances (all ratio to solar abundance) of C=0.00243,

N=2.43 O=2.66 Ne=0.46 (Model A in Rauch et al. 2010) or C=0.03, N=64.0, O=33.72, Ne=0.33, Mg=0.35, Si=1.5, S=0.026 (Model B in Rauch et al. 2010). Our fits to the April 2003 RGS data yield enhanced nitrogen and oxygen abundance of N=12-53 and O=24-53 (all ratio to solar abundance). We derive a very low carbon abundance of C=0.004-0.18 revealing that carbon is under-abundant in the moving absorber component along with the enhanced nitrogen and oxygen indicating that nuclear burning and dredge-up/mixing has been in effect. We note that Model A assumed by Rauch et al. (2010) is highly unrealistic for this RGS data set and Model B is more consistent with our findings. However, the carbon abundance is only 0.18 times its solar abundance (XABS fits) and is not as under-abundant as Rauch et al. (2010) assumes.

We find a neutral hydrogen column density of  $1.4-1.9 \times 10^{21} \text{ cm}^{-2}$  from our fits which is in excellent accordance with the value in Dickey and Lockman (1990). Our black-body temperatures are in a range  $(4.3-5.0) \times 10^5 \text{ K}$  which is slightly less than the results of static models, but in good agreement with expanding atmosphere models which has been calculated as  $5.8 \times 10^5 \text{ K}$  (Petz et al. 2005). Our fits to the April 2003 RGS data indicate a blue-shift range of 1085-1603  $\text{km s}^{-1}$  from simultaneous modeling of all absorption features which is a unique result.

We find that the turbulent velocity broadening is in a range 277-860  $\text{km s}^{-1}$  for V2491 Cyg. This value is 60  $\text{km s}^{-1}$  from the HOT model and 656-790  $\text{km s}^{-1}$  from the XABS model for V4743 Sgr. We argue that 60  $\text{km s}^{-1}$  is unacceptably low value for any expanding envelope or wind interpretation which then would make the HOT absorption model nonphysical. This is, also, consistent with higher  $\chi^2_{\nu}$  value of the HOT model fits revealing that the absorber is likely not collisionally ionized.

Finally, we note that the X-ray absorption in classical novae during the outburst stage is complicated with several different components. Simple absorption from photospheric lines are inadequate.

## CHAPTER 6

### SUMMARY AND CONCLUSION

X-ray observations of Cataclysmic Variables offer substantial information especially on the accretion and X-ray emission in binary systems, as well as the physical properties of the white dwarves. In this work, we have presented the XMM-Newton X-ray analysis of various selected CVs. We tried to determine the underlying physics by examining the X-ray spectra and light curves of the sources. For the first four sources in "accretion phase" (EX Hya, FO Aqr, PQ Gem and V2069 Cyg) we tried to establish the relation of the underlying X-ray emission mechanism and absorbing components with the orbital and/or spin period of the system, hence determine the physical state and the geometry in these systems. For the latter two sources which have undergone outbursts (V4743 Sgr and V2491 Cyg), we tried to determine the features of the absorption structure of the ejecta and the underlying X-ray emission

The XMM-Newton EPIC pn (0.3-10. keV) spectrum of the IP EX Hya together with spin and orbital phase-resolved spectroscopy were thoroughly investigated for the first time in this work. We have used two different observations of EX Hya to look for spectral variations over time. In both observations the mass accretion rate and luminosities are compatible with those of the previous quiescent observations, hence the source is in a quiescent state both in 2000 and 2003. The X-ray emission is modelled as arising from three different components: two collisional equilibrium plasma emission models around 0.6-0.8 keV and 1.3-1.7 keV and a cooling-flow plasma emission model with a distribution of 3 to 33 keV for the 2000 state and 8 to 61 keV for the 2003 state. We find very little change in the spectral parameters of the two collisional equilibrium plasma emission models over the orbital and spin cycles. In general, the

two observations of the source reveal spectral variations. For the 2000 data, we find neutral hydrogen column densities in a range  $0.01-0.2 \times 10^{22} \text{ cm}^{-2}$  from spin phase-resolved spectroscopy (with covering fractions ranging from 0.2-0.5), and  $0.01-0.08 \times 10^{22} \text{ cm}^{-2}$  from orbital phase-resolved spectroscopy (where covering fraction is 1.0). For the 2003 data, the neutral hydrogen column densities are in a range  $0.03-0.1 \times 10^{22} \text{ cm}^{-2}$  (with covering fractions of 0.6-1.0) in the spin resolved spectroscopy, and  $0.02-0.15 \times 10^{22} \text{ cm}^{-2}$  in the orbital phase-resolved spectroscopy (with covering fraction of 1.0). The highest  $N_{\text{H}}$  values always occur either at the orbital or spin phase minima. There is a definite difference in the absorber geometry for the spin phase-resolved spectroscopy between the two epochs. In the year 2000 it shows a covering fraction of 0.2-0.5 whereas in the year 2003 it shows a covering fraction of 0.6-1.0 (both years show that covering fraction reduces towards spin maxima). This indicates a geometrical change in the absorber from 2000 to 2003. The angle subtended by the absorber is considerably less in 2000 and hence the accretion curtain is reduced in size. Since we attained a model of only neutral absorption, we can not comment much on the ionization state changes of the absorber. We note that we do not rule out any occultation effect or change in the occultation effects. The absorption in the orbital plane changes by a factor of 2 from 2000 to 2003 and the absorption effects are more spread over the orbital cycle in comparison with the 2000 data. Thus, the bulge at the accretion impact zone is larger (and optically thicker) in 2003. We also note that both the spin and orbital phase-resolved spectroscopy of the 2003 data show a larger variation (3-25 keV) for the  $LowT$  parameter of the cooling-flow plasma emission model as compared to the 2000 state where this parameter stays around 6-12 keV over most of the phase-resolved spectroscopy. Thus, the structure of the cooling flow and the absorption effects are different in the two different epochs of observations. This is not related to any mass accretion rate difference, but only to a difference in the accretion column temperature distribution structure and absorption.

We detect a 6.4 keV fluorescent Fe line at orbital phases 0.9-1.3 corresponding to the location of orbital minima in 2003 and it is absent in the orbital phases 0.4 to 0.8. This feature can be attributed to reflection from a region on the orbital plane most likely the bulge at the accretion impact zone and spread around the disk covering a location including the eclipse phases. So the absorber may be viewed in other wavelengths

at around these phases. We note that a 6.4 keV fluorescent Fe line is non-existent in the orbital phase-resolved spectroscopy of the 2000 data. This strongly indicates an accretion geometry change and a change in the bulge size (impact zone) from year 2000 to 2003; the bulge is larger and more spread in 2003.

We have presented X-ray orbital-phase resolved analysis of the intermediate polar FO Aqr. This work improves upon the previous works by calculating the spectral parameters over the orbital phase. The distinction between the absorbing components are clarified and the values are explicitly calculated. The absorption originating from the polar regions of the white dwarf can be resolved from the absorption by structures on the accretion disk. The shape of the spin pulse profile is unaffected by the orbital motion, however the semi-amplitude of the profile change over the orbital phase. The X-ray orbital variation over the orbit in the system arises from absorption by the bulge material on the disk spread well over the disk. The absorption column is greatly enhanced during the X-ray orbital dip. Moreover, we have modeled the absorption from the orbital dip with a warm absorber model for the first time for this source and also for CVs, confirming the ionized nature of the material on the disk causing the absorption. We derived a range of ionization parameter  $\log(\xi_{CV}) \sim -0.8-1$  for plausible warm absorbers on CV disks. We calculate that the orbital modulations in FO Aqr (and plausibly some other CVs) are similar to those seen in LMXB dippers as variations (density/temperature) of a warm absorber at the accretion impact region and spreading on the disk.

For PQ Gem and V2069 which are IPs with a soft blackbody component in their spectra, we performed orbital phase resolved analysis. We only covered the spectra during the orbital minima and maxima in detail because of the low count rates and exposure durations. Both systems show orbital modulation in X-rays. We could successfully differentiate the 3 different absorption components for PQ Gem. One component is the constant interstellar absorption, the second one is the high absorption which does not change between orbital minimum and maximum. The last component is related to the absorption from bulge on the disc near the hot spot, since it disappears from the line of sight at the orbital maxima. The modulation depth decreases at higher energies, and the hardness ratio varies in line with the orbital motion. These features support the absorption from the disc idea. For V2069 Cyg, we could not resolve the

distinct absorption components and therefore could not account for the absorption from disc component in the spectral analysis. However, the lightcurves and hardness ratios indicate such absorption is at work over the orbital phase. There is also possibility of occultation since the X-ray modulation persists at higher energies. The soft blackbody component remained the same for PQ Gem between orbital minima and maxima. However, for V2069 Cyg the temperature of the soft component is lower at the orbital minima with possible implication of reprocessing of the blackbody emission by the bulge on the disc.

Lastly, we presented a reanalysis of a selection of *XMM-Newton* RGS (Reflection Grating Spectrometer) data obtained for the two classical novae; V4743 Sgr and V2491 Cyg. We model the absorption components detected in the high resolution spectra independently from the assumed continuum model. We are utilizing a photo-ionized warm absorber model and a hot, collisionally ionized absorber model that we discuss in the light of observations. Our fits model all the absorption features simultaneously, thus calculating a global velocity shift for the absorption component in the data. We derive a blue-shift of 3078-3445 km s<sup>-1</sup> for V2491 Cyg and 1085-1603 km s<sup>-1</sup> for V4743 Sgr consistent with ejecta/wind speeds. We derive CNO abundances from our fits. V2491 Cyg has a nitrogen overabundance of N=14-36 (ratio to solar abundance) where C and O are about twice their solar abundance. V4743 Sgr shows a typical signature of H-burning with under-abundant C=0.004-0.2, and enhanced N=12-53 and O=24-53 (all ratio to solar abundances). We find the equivalent hydrogen column density of the ionized absorbers as  $(8.0-0.3) \times 10^{22}$  cm<sup>-2</sup> for V2491 Cyg and  $(3.6-4.3) \times 10^{23}$  cm<sup>-2</sup> for V4743 Sgr. Although these attempts at modelling the novae are still in initial stage, the results are promising to seek a more complex model with more components and combinations in order to explain the outburst spectra.

On the overall, this is a study that brings some contribution in understanding CVs in the X-ray regime. Extensive X-ray orbital and spin phase resolved spectral analysis of IPs; in detail analysis of the absorption components in CVs; detection of a possible warm absorbing element in a CV; taking the first steps in modelling the classical nova outbursts in X-rays with physical models are such contributions. However, the author is aware of the future improvements that can be done, especially with the analysis of the classical nova data.

## REFERENCES

- [1] Allan A., Hellier C., Beardmore A., 1998, MNRAS, 295, 167
- [2] Anders E., Grevesse N., 1989, GeCoA, 53, 197
- [3] Anzolin G., de Martino D., Bonnet-Bidaud J.-M., Mouchet M., Gänsicke B. T., Matt G., Mukai K., 2008, A&A, 489, 1243
- [4] Anzolin G., de Martino D., Falanga M., Mukai K., Bonnet-Bidaud J.-M., Mouchet M., Terada Y., Ishida M., 2009, A&A, 501, 1047
- [5] Anzolin G., Tamburini F., de Martino D., Bianchini A., 2010, A&A, 519, 69
- [6] Arnaud K. A., 1996, in Jacoby G., Barnes J., eds, ASP Conf. Ser. Vol. 101, Astronomical Data Analysis Software and Systems V., Astron. Soc. Pac., San Francisco, p. 17
- [7] Balman Ş., Krautter J., Ögelman, H., 1998, ApJ, 499, 395
- [8] Balman Ş., Krautter J., 2001, MNRAS, 326, 1441
- [9] Balman Ş., 2009, AJ, 138, 50
- [10] Balman Ş., 2012, MmSAI, 83, 585
- [11] Balman Ş., 2014, arXiv1403.4437B
- [12] Barlow E.J., Knigge C., Bird A.J., Dean A.J., Clark D.J., Hill A.B., Molina M., Sguera V., 2006, MNRAS, 372, 224
- [13] Beardmore, A. P., Mukai, K., Norton, A. J., Osborne, J. P., & Hellier, C., 1998, MNRAS, 297, 337
- [14] Belle K. E., Howell S. B., Sirk M. M., Huber M. E., 2002, ApJ, 577, 359
- [15] Belle K. E., Howell S. B., Mukai K., Szkody P., Nishikida K., Ciardi D. R., Fried R. E., Oliver J. P, 2005, AJ, 129, 1985
- [16] Bernardini F., de Martino D., Falanga M., Mukai K., Matt G., Bonnet-Bidaud J.-M., Masetti N., Mouchet M., 2012, A&A, 542, 22
- [17] Beuermann K., Burwitz V., 1995, ASPC, 85, 99
- [18] Beuermann K., Harrison Th. E., McArthur B. E., Benedict G. F., Gänsicke B. T., 2003, A&A, 412, 821

- [19] Bode M. F., Evans A., 2008, *Classical Novae*, 2nd Edition, Cambridge Astrophysics Series, No. 43, Cambridge: Cambridge University Press, 2008
- [20] Boirin, L., Méndez, M., Díaz Trigo, M., Parmar, A. N., & Kaastra J. S., 2005, *A&A*, 436, 195
- [21] Brunschweiler J., Greiner J., Ajello M., and Osborne J., 2009, *A&A*, 496, 121
- [22] Buckley D. A. H., Haberl F., Motch C., Pollard K., Schwarzenberg-Czerny A., Sekiguchi K., 1997, *MNRAS*, 287, 117
- [23] Cook, M. C., Watson, M. G., & McHardy, I. M., 1984, *MNRAS*, 210, 7
- [24] Cropper M., 1990, *SSRv*, 54, 195
- [25] Cropper M., Ramsay G., Wu K., 1998, *MNRAS*, 293, 222
- [26] Cropper M., Wu K., Ramsay G., 2000, *New Astron. Rev.*, 44, 57
- [27] Cropper M., Ramsay G., Hellier C., Mukai K., Mauche C., Pandel D., 2002, *RSPTA*, 360, 1951
- [28] Diaz-Trigo M., Parmar A. N., Boirin L., Méndez M., Kaastra J. S., 2006, *A&A*, 445, 179
- [29] Dickey J. M., Lockman F. J., 1990, *ARA&A*, 28, 215
- [30] Duck S.R., Rosen S.R., Ponman T.J., Norton A.J., Watson M.G., Mason K.O., 1994, *MNRAS*, 271, 372
- [31] Evans P. A., Hellier C., 2004, *MNRAS*, 353, 447
- [32] Evans, P. A., Hellier, C., Ramsay, G., & Cropper M., 2004, *MNRAS*, 349, 715
- [33] Evans P. A., Hellier C., Ramsay G., 2006, *MNRAS*, 369, 1229
- [34] Evans P. A., Hellier C., 2007, *ApJ*, 663, 1277
- [35] Ezuka H., Ishida M., 1999, *ApJ*, 120, 277
- [36] Frank J., King A. R., Lasota J. -P., 1984, *A&A*, 178, 137
- [37] Fujimoto R., Ishida M., 1997, *ApJ*, 474, 774
- [38] Hamilton R. T. et al., *ApJ*, 667, 1139
- [39] Haseda K., West D., Yamaoka H. & Masi G., 2002, *IAU Circ.*, 7975
- [40] Hellier C., Mason K. O., Rosen S. R., Cordova, F. A., 1987, *MNRAS*, 228, 463
- [41] Hellier C., Cropper M., Mason K. O., 1991, *MNRAS*, 248, 233
- [42] Hellier C., Sproats L. N., 1992, *IBVS*, 3724, 1



- [43] Hellier, C., 1993, MNRAS, 265, 35
- [44] Hellier C., Garlick M. A., Mason K. O., 1993, MNRAS, 260, 299
- [45] Hellier C., 1997, MNRAS, 288, 817
- [46] Hellier, C., Mukai, K., Ishida, M., & Fujimoto, R., 1996, MNRAS, 280, 877
- [47] Hellier C., Mukai K., Beardmore A. P., 1997, MNRAS, 292, 397
- [48] Hellier C., Beardmore A. P., 2002, MNRAS, 331, 407
- [49] Hellier C., Mukai K., 2004, MNRAS, 352, 1037
- [50] Hellier, C., 2001, "Cataclysmic Variable Stars, How and why they vary", Springer-Praxis Books in astronomy and space sciences, Cornwall
- [51] Helton L.A., Woodward C.E., Valandingham K., Schwarz G.J., 2008, IAU Circ., 1379, 1
- [52] den Herder J. W. et al., 2001, A&A, 365, 7
- [53] Hernanz M., 2005, ASPC, 330, 265
- [54] Hoogerwerf R., Brickhouse N. S., Mauche C. W., ApJ, 2005, 628, 946
- [55] Ibarra A. et al., 2009, A&A, 497, L5
- [56] Itoh, K., Okada, S., Ishida, M., Kunieda, H., 2006, ApJ, 639, 397
- [57] Ishida M., 2010, SSRv, 157, 155
- [58] James C. H., Ramsay G, Mark C, Branduardi-Raymont, G., 2002, MNRAS, 336, 550
- [59] Jansen F. et al., 2001, A&A, 365, 1
- [60] Kaastra J.S., Mewe R., Nieuwenhuijzen H., 1996, in UV and X-ray Spectroscopy of Astrophysical and Laboratory Plasmas, Frontiers science series, 15, 411
- [61] Kahabka P., Hartmann H. W., Parmar A. N., Negueruela I., 1999, A&A, 347, 43
- [62] Kalberla P. M. W., Burton W. B., Hartmann D., Arnal E. M., Bajaja E., Morras R., Poppel W. G. L., 2005, A&A, 440, 775
- [63] Kallman, T., & Bautista, M., 2001, ApJS, 133, 221
- [64] Kato T. et al., 2002, IAU Circ., 7976
- [65] King A. R., Lasota J. -P., 1979, MNRAS, 188, 653
- [66] King A. R., Lasota J. -P., 1990, MNRAS, 247, 214

- [67] Kiziloglu U., Baykal A., Alev M., Gogus E., 1998, *ApSpSci*, 259, 191
- [68] Knigge C., 2011, *ASPC*, 447, 3
- [69] Kraft R. P., 1962, *ApJ*, 135, 408
- [70] Kuulkers E., Norton A., Schwobe A., Warner B., 2006, in "Compact stellar X-ray sources", eds. Lewin W. & van der Klis M., vol 39., p. 421 - 460
- [71] Lamb D. Q., Masters A. R., 1979, *ApJ*, 234, 117
- [72] Landi R., Bassani L., Dean A.J., Bird A.J., Focchi M., Bazzano A., Nousek J.A., Osborne J.P., 2009, *MNRAS*, 392, 630
- [73] Luna G. J. M., Raymond J. C., Brickhouse N. S., Mauche C. W., Proga D., Steeghs D., Hoogerwerf R., 2010, *ApJ*, 711, 1333
- [74] Lynch D.K. et al., 2008, *AJ*, 136, 1815
- [75] Lynden-Bell D., Pringle J. E., 1974, *MNRAS*, 168, 603
- [76] de Martino, D., Silvotti, R., Buckley, D. A. H., Gänsicke, B. T., Mouchet, M., Mukai, K., & Rosen, S. R., 1999, *A&A*, 350, 517
- [77] de Martino D., Matt G., Belloni T., Haberl F., Mukai K., 2004, *A&A*, 415, 1009
- [78] de Martino D., Matt G., Mukai K., Bonnet-Bidaud J.-M., Burwitz V., Gänsicke B. T., Haberl F., Mouchet M., 2006, *A&A*, 454, 287
- [79] de Martino D., Matt G., Mukai K., Bonnet-Bidaud J.-M., Falanga M., Gänsicke B. T., Haberl F., Marsh T. R., Mouchet M., Littlefair S. P., Dhillon V., 2008, *A&A*, 481, 149
- [80] de Martino D., Bonnet-Bidaud J. M., Falanga M., Mouchet M., Motch C., 2009, *ATel*, 2089, 1
- [81] Mason K.O., Watson M.G., Ponman T.J., Charles P.A., Duck S.R., Hassall B.J.M., Howell S.B., Ishida M., Jones D.H.P., Mittaz J.P.D., 1992, *MNRAS*, 258, 749
- [82] Mason K.O., 1997, *MNRAS*, 285, 493
- [83] Mason K. O., Drew J. E., Knigge C., 1997, *MNRAS*, 290, 23
- [84] Mason K. O. et al., 2001, *A&A*, 365, 36
- [85] Mauche C. W., Raymond J. C., 2000, *ApJ*, 541, 924
- [86] Mauche C. W., Robinson E. L., 2001, *ApJ*, 562, 508
- [87] McNamara A. L., Kuncic Z., Wu K., Galloway D. K., Cullen J. G., 2008, *MNRAS*, 383, 962

- [88] Mhlahlo N., Buckley D. A. H., Dhillon V. S., Potter S. B., Warner B., Woudt P. A., 2007a, MNRAS, 380, 353
- [89] Mhlahlo N., Buckley D. A. H., Dhillon V. S., Potter S. B., Warner B., Woudt P. A., 2007b, MNRAS, 378, 211
- [90] Morrison R., McCammon D., 1983, ApJ, 270, 119
- [91] Motch C., Guillout P., Haberl F., Krautter J., Pakull M.W., Pietsch W., Reinsch K., Voges W., Zickgraf F.-J. 1998, A&AS, 132, 341
- [92] Mukai, K., Ishida, M., & Osborne, J. P., 1994, PASJ, 46, 87
- [93] Mukai K, Wood J. H., Naylor T., Schlegel, E. M., Swank, J., 1997, ApJ, 475, 812
- [94] Mukai K., Kallman T., Schlegel E., Bruch A., Handle G., Kemp J., 2001, ASPC, 251, 90
- [95] Mukai K., Kinkhabwala A., Peterson J. R., Kahn S. M., Paerels F., 2003, ApJ, 586, 77
- [96] Mukai K., 2003, AdSpR, 32, 2067
- [97] Nakano et al., 2008, IAU Circ., 8934
- [98] Naylor T., la Dous C., 1997, MNRAS, 290, 160
- [99] Nelemans G., 2005, ASPC, 330, 27
- [100] Nelson T., Orio M., Cassinelli J.P., Still M., Leibowitz E., Mucciarelli P., 2008, ApJ, 673, 1067
- [101] Ness J.-U. et al., 2003, ApJ, 594, L127
- [102] Ness J.-U. et al., 2011, ApJ, 733, 70
- [103] Nielbock M., Schmdtobreck L., 2003 A&A, 400, 5
- [104] Norton A. J., Watson M. G., 1989, MNRAS, 237, 715
- [105] Norton, A. J., Watson, M. G., King, A. R., Lehto, H. J., & McHardy, I. M., 1992, MNRAS, 254, 705
- [106] Norton, A. J., Beardmore, A. P., & Taylor, P., 1996, 280, 937
- [107] Norton A. J., Beardmore A. P., Allan A., Hellier C., 1999, A&A, 347, 203
- [108] Norton A. J., Wynn G. A., Somerscales R. V., 2004, ApJ, 614, 349
- [109] Orio M., Parmar A., Greiner J., Ögelman H., Starrfield S., & Trussoni E., 2002, MNRAS, 333, L11

- [110] Osaki Y., 1996, *PASP*, 108, 39
- [111] Osborne, J. P., & Mukai, K., 1989, *MNRAS*, 238, 1233
- [112] Osborne J.P. et al., 2011, *ApJ*, 727, 124
- [113] Page K.L. et al., 2010, *MNRAS*, 401, 121
- [114] Pandel D., Cordova F. A., Mason K. O., Priedhorsky W. C., 2005, *ApJ*, 626, 396
- [115] Parker, T. L., Norton, A. J., & Mukai, K., 2005, *A&A*, 439, 213
- [116] Patterson J., 1994, *PASP* 106, 209
- [117] Patterson J., Raymond J.C., 1985, *ApJ*, 292, 535
- [118] Patterson, J., Kemp, J., Richman, H. R., Skillman, D. R., Vanmunster, T., Jensen, L., Buckley, D. A. H., O'Donoghue, D., & Kramer, R., 1998, *PASP*, 110, 415
- [119] Pekön Y., Balman Ş., 2008, *MNRAS*, 388, 921
- [120] Pekön Y., Balman Ş., 2011, *MNRAS*, 411, 1177
- [121] Pekön Y., Balman Ş., 2012, *AJ*, 144, 53
- [122] Petz A., Hauschildt P.H., Ness J.-U. & Starrfield S., 2005, *A&A*, 431, 321
- [123] Pinto C., Ness J.-U., Verbunt F., Kaastra J. S., Costantini E., Detmers R. G., 2012, 2012, *A&A*, 543, 134
- [124] Pratt G. W., Mukai K., Hassall B. J. M., Naylor T., Wood J. H., 2004, *MNRAS*, 348, 49
- [125] Pringle J.E., 1981, *ARA&A*, 19, 137
- [126] Ramsay G., Mason K. O., Cropper M., Watson M. G., Clayton K. L., 1994, *MNRAS*, 270, 692
- [127] Ramsay G., Poole T., Mason K., Cordova F., Priedhorsky W., Breeveld A., Much R., Osborne J., Pandel D., Potter S., West J., Wheatley P., 2001, *A&A*, 365, 288
- [128] Ramsay G., Cropper M., 2004, *MNRAS*, 347, 497
- [129] Ramsay G., Cropper M., Wu K., Mason K. O., Cordova F. A., 2004, *MNRAS*, 350, 1373
- [130] Ramsay G., Bridge C. M., Cropper M., Mason K. O., Cordova F. A., Priedhorsky W., 2004, *MNRAS*, 354, 773

- [131] Rana V. R., Singh K. P., Schlegel E.M., Barret P. E., 2004, AJ, 127, 439
- [132] Rana V. R., Singh K. P., Schlegel E.M., Barret P. E., 2006, ApJ, 642, 1042
- [133] Rana V. R., Singh K. P., Schlegel E.M., Barret P. E., 2006, AdSpR, 38, 284
- [134] Rauch T., Orio M., Gonzales-Riestra R., Nelson T., Still M., Werner K. & Wilms J., 2010, ApJ, 717, 363
- [135] Raymond J. C., Brickhouse N. S., 1996, ApJ, 237, 321
- [136] Rosen, S. R., Mason, K. O., & Cordova, F. A. 1988, MNRAS, 231, 549
- [137] van Rossum D.R., Ness J.-U., 2010, AN, 331, 75
- [138] Salinas, A., & Schlegel E. M., 2004, AJ, 128, 1331
- [139] Scaringi S., Bird A. J., Norton A. J., Knigge C., Hill A. B., Clark D. J., Dean A. J., McBride V. A., Barlow E. J., Bassani L., Bazzano A., Fiacchi M., Landi R., 2010, MNRAS, 401, 2207
- [140] Schwarz R., Reinsch K., Beuermann K., Burwitz V., 2005, A&A, 442, 271
- [141] Schwope A. D., Schwarz R., Sirk M., Howell S. B., 2001, A&A, 375, 419
- [142] Semena A. N., Revnivtsev M. G., Buckley D. A. H., Kotze M. M., Khabibullin, I. I., Breytenbach H., Gulbis A. A. S., Coppejans R., Potter S. B., 2014, MNRAS, 442, 1123
- [143] Shakura N. I., Sunyaev R.A., 1973, A&A, 24, 337
- [144] Singh K. P., Rana V. R., Mukerjee K., Barrett P., Schlegel E. M., 2004, ASPC, 315, 135
- [145] Singh K. P., 2013, ASInC, 8, 115
- [146] Staude, A., Schwope, A. D., Schwarz, R., Vogel, J., Krumpke, M., Nebot Gomez-Moran, A., 2008, A&A, 486, 899
- [147] Strüder L. et al., 2001, A&A, 365, 18
- [148] Szkody P., Nishikida K., Raymond J. C., Seth A., Hoard D. W., Long K. S., Sion E. M., 2002, ApJ, 574, 942
- [149] van Teeseling A, 1997, A&A, 319, 25
- [150] Terada Y., Ishida M., Makishima K., 2004, PASJ, 56, 533
- [151] Thorstensen J.R., Taylor C.J., 2001, MNRAS, 326, 1235
- [152] Tomov T., Mikolajewski M., Ragan E., Swierczynski E., Wychadzki P., 2008, Astron. Tel., 1475

- [153] Verbunt F., 1982, *SSRv*, 32, 379
- [154] Vogt N., Krzeminski W., Sterken C., 1980, *A&A*, 85, 106
- [155] Warner B. 2003, *Cataclysmic Variable Stars*. Cambridge Univ. Press, Cambridge
- [156] Warner B., Woudt P. A., 2002, *ASPC*, 259, 584
- [157] Wheatley P. J., West R. G., 2003, *MNRAS*, 345, 1009
- [158] Wheatley P. J., Mauche C. W., Mattei J. A., 2003, *MNRAS*, 345, 49
- [159] van der Woerd H., Heise J., Bateson F., 1986, *A&A*, 156, 252
- [160] Wu K., 2000, *SSRv*, 93, 611
- [161] Yuasa, T., Nakazawa, K., Makishima, K., Saitou, K., Ishida, M., Ebisawa, K., Mori, H., & Yamada S., 2010, *A&A*, 520, 25

# CURRICULUM VITAE

## PERSONAL INFORMATION

**Surname, Name:** Pekön, Yakup

**Nationality:** Turkish (TC)

**Date and Place of Birth:** 15 November 1982, Ankara

**Marital Status:** Single

**Phone:** 03122107637

## EDUCATION

<b>Degree</b>	<b>Institution</b>	<b>Year of Graduation</b>
Ph.D.	PHYSICS, METU	2014
M.S.	PHYSICS, METU	2007
B.S.	PHYSICS, METU	2004
High School	TEV İTÖL	2000

## PROFESSIONAL EXPERIENCE

<b>Year</b>	<b>Place</b>	<b>Enrollment</b>
2013 -	Atılım University	Research Assistant
2006-2013	METU	Student Assistant for TUBITAK project

## **PUBLICATIONS**

"Orbital phase-resolved spectroscopy of the intermediate polar FO Aqr using XMM-Newton Observatory Data" - Pekon Y., Balman S., 2012, AJ, 144, 53

"Orbital and spin phase-resolved spectroscopy of the intermediate polar EX Hya using XMM-Newton data" - Pekon Y., Balman S., 2011, MNRAS, 411, 1177

"RR Pic (1925): An X-ray View" - Pekon Y., Balman S., 2008, MNRAS, 388, 921

### **International Conference Publications**

"High resolution XMM-Newton data of Nova Outbursts using Warm and Hot Absorber Models" - Balman S., Pekon Y., 2013, in Binary Paths to Type Ia Supernovae Explosions, Proceedings of the International Astronomical Union, IAU Symposium, Volume 281, p. 124-125

"Orbital-phase Resolved Spectroscopy of FO Aqr (IP) Using XMM-Newton data" Pekon Y., Balman S., 2011, in "The X-ray Universe 2011", 266

"Orbital Phase-Resolved Spectroscopy of Selected Intermediate Polars: EX Hya, 1RXSJ173021.5 and FO Aqr" - Balman S., Pekon Y., in "Physics of Accreting Compact Binaries", 2010, in press

"Orbital Phase Resolved Spectroscopy of EX Hya Using XMM-NEWTON" - Pekon Y., Balman S., in "X-RAY ASTRONOMY 2009; PRESENT STATUS, MULTIWAVELENGTH APPROACH AND FUTURE PERSPECTIVES", 2010, AIPC, 1248, 137